



# LUND UNIVERSITY

## Prospects of Observing the Decay $B_c \rightarrow J/\psi + \pi$ and the Alignment Performance in the ATLAS Experiment

Ji, Weina

2010

[Link to publication](#)

*Citation for published version (APA):*

Ji, W. (2010). *Prospects of Observing the Decay  $B_c \rightarrow J/\psi + \pi$  and the Alignment Performance in the ATLAS Experiment.*

*Total number of authors:*

1

### General rights

Unless other specific re-use rights are stated the following general rights apply:

Copyright and moral rights for the publications made accessible in the public portal are retained by the authors and/or other copyright owners and it is a condition of accessing publications that users recognise and abide by the legal requirements associated with these rights.

- Users may download and print one copy of any publication from the public portal for the purpose of private study or research.
- You may not further distribute the material or use it for any profit-making activity or commercial gain
- You may freely distribute the URL identifying the publication in the public portal

Read more about Creative commons licenses: <https://creativecommons.org/licenses/>

### Take down policy

If you believe that this document breaches copyright please contact us providing details, and we will remove access to the work immediately and investigate your claim.

LUND UNIVERSITY

PO Box 117  
221 00 Lund  
+46 46-222 00 00

ISBN 978-91-7473-017-3  
LUNFD6/(NFFL-7229)2010

**Prospects of Observing the Decay  $B_c \rightarrow J/\psi \pi$   
and  
the Alignment Performance in the ATLAS experiment**

Thesis submitted for the degree of  
Doctor of Philosophy  
by

**Weina Ji**



**LUND**  
UNIVERSITY

DEPARTMENT OF PHYSICS  
LUND, 2010

Thesis Advisor: Dr. Else Lytken  
Faculty Opponent: Prof. Ian Shipsey

To be presented, with the permission of the Faculty of Science of Lund University, for public criticism in lecture hall B of the Department of Physics on Friday, the 24th of September 2010, at 14.00.



<b>Organisation</b> LUND UNIVERSITY Department of Physics Lund University Box 118 SE-221 00 Lund SWEDEN		<b>Document name</b> DOCTORAL DISSERTATION
		<b>Date of issue</b> August, 2010
		<b>CODEN</b> LUNFD6/(NFFL-7229)2010
<b>Author(s)</b> Weina Ji		<b>Sponsoring organisation</b>
<b>Title and subtitle</b> Prospects of Observing the Decay $B_c \rightarrow J/\psi \pi$ and the Alignment Performance in the ATLAS Experiment		
<b>Abstract</b>  This thesis contains two main aspects of my research work towards physics in proton-proton collisions in the ATLAS experiment at the LHC. First, a Monte Carlo based analysis of the event yield and the mass shape for the ground state of the $B_c$ meson in the hadronic decay channel $B_c \rightarrow J/\psi \pi$ was studied. The selection criteria have been optimised, the total number of signal events, and the significance of the observation have been estimated for the detector configuration and backgrounds expected at the centre-of-mass energy of 10 TeV with $1 \text{ fb}^{-1}$ of integrated luminosity. As the momenta of these decay products are relatively low, compared with the main objectives of the ATLAS physics program, the performance of the inner detector is crucial for the low $p_T$ tracking. As a result, the second part of the thesis is focused on the impact of the inner detector alignment on physics. Monte Carlo studies were performed by looking at the reconstructions of the well-known resonances, $K_s^0$ , $J/\psi$ , $\Upsilon$ and $Z^0$ in misalignments, particularly the systematic misalignments. Then the performance of two different alignments that have been applied subsequently in ATLAS since the start up of the LHC were investigated using $K_s^0 \rightarrow \pi^+ \pi^-$ events in the current 7 TeV collisions. Finally, I summarise the performance of the inner detector on the early $J/\psi \rightarrow \mu^+ \mu^-$ reconstruction in collisions, which is essential for the coming B physics measurements.		
<b>Key words:</b> LHC, ATLAS, $B_c$ ground state, Inner Detector alignment, Weak modes, Resonances		
<b>Classification system and/or index terms (if any)</b>		
<b>Supplementary bibliographical information:</b>		<b>Language</b> English
<b>ISSN and key title:</b>		<b>ISBN</b> 978-91-7473-017-3
<b>Recipient's notes</b>	<b>Number of pages</b> 144	<b>Price</b>
	<b>Security classification</b>	

**Distribution by (name and address)**

Weina Ji  
Department of Physics  
Div. of Experimental High-Energy Physics  
Box 118, SE-221 00 Lund, SWEDEN

I, the undersigned, being the copyright owner of the above-mentioned dissertation, hereby grant to all reference sources permission to publish and disseminate the abstract of the above-mentioned dissertation.

Signature Weina Ji

Date 16/08, 2010



# Contents

<b>Outline</b>	<b>i</b>
<b>1 Introduction to particle physics</b>	<b>1</b>
1.1 The Standard Model . . . . .	1
1.2 The electroweak theory . . . . .	3
1.3 The Higgs mechanism . . . . .	3
1.4 Quantum chromodynamics . . . . .	5
1.5 Summary . . . . .	6
<b>2 Heavy quark physics</b>	<b>9</b>
2.1 Heavy quark production . . . . .	9
2.2 Heavy quark decays . . . . .	12
2.3 Quarkonium . . . . .	13
2.3.1 Quarkonium spectrum . . . . .	14
2.3.2 Quarkonium production . . . . .	19
2.4 Physics of $B_c$ mesons . . . . .	22
2.4.1 Mass spectrum . . . . .	22
2.4.2 $B_c$ decays . . . . .	27
2.4.3 $B_c$ production . . . . .	29
<b>3 LHC and the ATLAS experiment</b>	<b>33</b>
3.1 The LHC machine . . . . .	34
3.2 The ATLAS experiment . . . . .	37
<b>4 Expected performance of the ATLAS experiment</b>	<b>43</b>
4.1 Tracking . . . . .	43
4.2 Muon reconstruction and triggers . . . . .	55
4.2.1 Muon reconstruction . . . . .	56
4.2.2 Muon triggers . . . . .	65
<b>5 Prospects of observing <math>B_c \rightarrow J/\psi \pi</math> events in ATLAS</b>	<b>67</b>
5.1 Introduction . . . . .	67
5.2 Monte Carlo samples . . . . .	67
5.3 Event offline analysis . . . . .	70
5.4 Comparison with the channel $B^+ \rightarrow J/\psi K^+$ . . . . .	79

---

5.5	Results . . . . .	80
5.6	Statistical and systematic uncertainties . . . . .	83
5.7	Summary and outlook . . . . .	86
<b>6</b>	<b>Impact of the ID alignment on tracking and physics</b>	<b>87</b>
6.1	Alignment of the ATLAS inner detector . . . . .	87
6.1.1	Track-based alignment of the inner detector . . . . .	88
6.1.2	Systematic misalignment . . . . .	90
6.2	Impact of the ID alignment on resonances . . . . .	93
6.2.1	Resonances in the ATLAS offline data quality monitoring . . . . .	94
6.2.2	Impact of weak mode misalignments on resonances . . . . .	101
6.3	Alignment performance in 7 TeV $pp$ collisions at the LHC . . . . .	109
6.3.1	Alignment performance on tracks in 7 TeV $pp$ collisions . . . . .	109
6.3.2	Alignment performance in $K_s^0 \rightarrow \pi^+\pi^-$ events at 7 TeV . . . . .	112
6.3.3	Early $J/\psi$ performance of the inner detector . . . . .	116
<b>7</b>	<b>Summary and outlook</b>	<b>121</b>
	<b>Acknowledgement</b>	<b>125</b>
	<b>Bibliography</b>	<b>132</b>
	<b>List of abbreviations</b>	<b>133</b>

*To my parents*





# Outline

The Large Hadron Collider (LHC) at CERN is currently the world's largest collider and accelerator, designed to collide two circular beams of protons or lead-ions at high energy and luminosity. The first collision in the LHC took place on November 23rd 2009 with protons colliding at the centre-of-mass energy of 900 GeV. Since March 2010, the LHC has been operating with proton-proton collisions at an unprecedented energy of 7 TeV and is planned to reach 14 TeV in a few years' time. Among the LHC experiments, ATLAS (A Toroidal LHC ApparatuS) is one of the general-purpose experiments, with about 3000 scientists from all over the world to investigate the particles produced in the collisions, so as to exploit the physics potential of the LHC.

Of the many approaches to understanding our universe, particle physics is focused on studying the basic constituents of matter and the fundamental forces in nature. The Standard Model in particle physics has accurately described the elementary particles and their interactions, postulating the Higgs field that assigns a mass to any particle that interacts with its force-carrying particle, the "Higgs". The "Higgs" particle has not yet been observed in experiments, and therefore searching for the Higgs is one of the main goals at the LHC. A brief overview of the Standard Model is given in Chapter 1.

In addition, a large variety of physics researches are expected to be carried out at the LHC, from precision measurements of the properties of known particles, to searches for signatures revealing physics beyond the Standard Model. One part of my research work is measuring the properties of the  $B_c$  meson which is a bound state of  $b$  and  $c$  quarks. The theory for the strong interaction of quarks is called Quantum Chromodynamics (QCD), where the heavy quark interactions ( $c$ ,  $b$  and  $t$  quarks) are in the perturbative regime. Chapter 2 is focused on the theoretical description of heavy quarks,  $c$  and  $b$  quarks, and their bound states. The mechanisms of heavy quark hadronic production and their decays will be introduced in Sec. 2.1 and Sec. 2.2, and 2.3 summarises the theoretical models proposed to interpret the mass spectra and productions of charmonium ( $c\bar{c}$ ) and bottomonium ( $b\bar{b}$ ) systems. Sec. 2.4 presents an overview of the theoretical predictions of the intermediate system, the  $B_c$  meson.

The LHC accelerator, and the structure of the ATLAS detector are described in Chapter 3. Although the main objectives of the ATLAS experiment are searches of the Higgs particle over a large expected mass range, as well as of signatures for physics beyond the Standard Model, measurements of B hadron properties and the CP violation are expected to test the Standard Model predictions and provide constraints to new physics models. In

order to improve the current world precision B measurements, tracking and muon reconstruction are crucial. The performance of the relevant sub-systems in ATLAS, the Inner Detector (ID) and the Muon Spectrometer (MS), were investigated using Monte Carlo simulation samples reconstructed with full detector response, and some of these results are reviewed in Chapter 4.

Chapter 5 presents my study of the prospects of observing  $B_c \rightarrow J/\psi \pi$  events in ATLAS. The  $B_c$  meson is unique because of its open flavour with two heavy quarks,  $b$  and  $c$ . Models which describe the  $c\bar{c}$  and  $b\bar{b}$  systems should also be able to predict this  $b\bar{c}$  (and  $\bar{b}c$ ) system, and therefore measurements on the properties of the  $B_c$  meson, which are not precise at present, could serve as complementary tests of the theoretical models proposed for quarkonium. In addition, the mass spectrum is expected to provide constraints to the shape of the strong potential inside hadrons. Together with my collaborators, I have investigated the ATLAS sensitivity for this channel using Monte Carlo samples fully simulated for the 10 TeV scenario with  $1 \text{ fb}^{-1}$  integrated luminosity. This study also applies to the current 7 TeV running.

Just like our  $B_c$  search, most of the B hadron measurements in ATLAS involves di-muon signatures, taking advantages of the efficient muon triggers. Reconstruction of these low  $p_T$  muons are driven by the inner detector. Therefore, I have also been working on the performance of the inner detector, in particular the impact of the ID alignment on low  $p_T$  physics. My contribution is to study the expected misalignments with Monte Carlo samples of resonance decays, with the emphasis on global systematic misalignments. In Chapter 6, Sec. 6.1 first introduces the track-based alignment algorithms applied for the ID track reconstruction. Sec. 6.2 illustrates some results of Monte Carlo studies to which my contribution is the study with  $J/\psi \rightarrow \mu^+\mu^-$  and  $\Upsilon \rightarrow \mu^+\mu^-$  decays. Besides, I have contributed to the software development work to implement our studies in the ATLAS offline data quality framework which is currently assessing the ID alignment and performance during data taking. Since the start up of the LHC, two different sets of the ID alignment constants have been applied subsequently in ATLAS, the improvement of the latest alignment is demonstrated in Sec. 6.3.1 using events recorded by the ATLAS minimum bias trigger. Because the production of  $K_s^0$  mesons is copious at the current LHC energy, I have investigated the  $K_s^0$  performance with these two alignments, included in Sec. 6.3.2. In the end, Sec. 6.3.3 presents the first study of the ID performance on  $J/\psi$  which is most important for the coming B physics measurements.

My contributions to the ATLAS experiment can also be found in the following documents:

1. *B Hadron Properties at the LHC*, contribution to the proceedings of *12th International Conference on B-Physics at Hadron Machines*, PoS(BEAUTY 2009)046, ATL-PHYS-PROC-2009-143
2. *A Study of the ATLAS Detector Sensitivity for the Event Yield in the  $B_c$  Meson Mass Region*, ATLAS note (internal) ATL-PHYS-INT-2010-066
3. *Inner Detector Alignment and Performance Monitoring*, ATLAS note (internal), ATL-INDET-INT-2009-006
4.  *$J/\psi$  Performance of the ATLAS Inner Detector*, ATLAS note, ATLAS-CONF-2010-078

# Chapter 1

## Introduction to particle physics

Particle physics is focused on studying the fundamental structure of our universe, the elementary particles and their interactions. The particles can be divided into two categories, matter particles and carrier particles. Matter particles are fermions with spin  $\frac{1}{2}$ , and carrier particles are bosons with integer spin which mediate the fundamental forces between particles. There are known to be four fundamental forces in nature: the electromagnetic force, the strong force, the weak force, and the gravitational force. Details of the discussions could be found in many documents, e.g. Ref. [1].

Matter particles come in two basic types called quarks and leptons (as well as their antiparticles). Both quark and lepton families comprise six member particles (called “flavours”) paired in three generations. Table 1.1 lists some of the characteristics of the quarks and leptons. In the lepton family, the  $e$ ,  $\mu$  and  $\tau$  all have an electric charge  $-e$  ( $e$  is equivalent to  $1.602 \times 10^{-19}$  C) and are massive, whilst the neutrinos are charge neutral with very little mass. In the quark family, the up-type quarks (up, charm and top quarks) have charge  $+\frac{2}{3}e$  and the down-type quarks (down, strange and bottom quarks) have charge  $-\frac{1}{3}e$ . In addition, quarks carry colour charge and are bound to form hadrons by the strong force. In nature, only colour neutral states (colour singlets) exist. Hadrons that are formed by a quark and an antiquark are called mesons, such as pions, and three-quark states are called baryons, such as protons and neutrons.

The interactions between the quarks and leptons are mediated by the exchange of carrier particles: the electromagnetic force is carried by the photon; the weak interaction is carried by bosons called  $W^\pm$  and  $Z^0$ ; gluons are responsible for the strong force. Among the fundamental interactions, the gravitation is the weakest, playing no significant role at the energy scales probed in particle physics. However, it is believed that the proposed graviton is the corresponding force-carrying particle of gravity.

### 1.1 The Standard Model

The Standard Model provides a remarkably accurate description of strong, weak, and electromagnetic interactions of elementary particles based on quantum field theory. In quantum field theory, particles are described by separate fields, and the dynamics of the

Generation	Quarks			Leptons		
	Flavour	Charge [e]	Mass	Flavour	Charge [e]	Mass
I	u	+2/3	1.5-3.3 MeV	$\nu_e$	0	< 3 eV
	d	-1/3	3.5-6.0 MeV	e	-1	0.511 MeV
II	c	+2/3	$\sim 1.27$ GeV	$\nu_\mu$	0	< 0.19 MeV
	s	-1/3	$\sim 104$ MeV	$\mu$	-1	105.66 MeV
III	t	+2/3	$\sim 171$ GeV	$\nu_\tau$	0	< 18.2 MeV
	b	-1/3	$\sim 4.2$ GeV	$\tau$	-1	$\sim 1776.8$ MeV

Table 1.1: Properties of mass particles: quarks and leptons. For each particle listed here, there is also an antiparticle with opposite quantum numbers [2].

particles are encapsulated in a Lagrangian. The Standard Model is a non-Abelian gauge theory and the Lagrangian is invariant under transformations characterised by the symmetry group  $SU(3)_C \times SU(2)_L \times U(1)_Y$ , where  $C$  is the colour charge of quarks,  $L$  refers to the left-handed chirality parts of the fermions that transform as weak isospin doublets, and  $Y$  is the electroweak hypercharge. The right-handed parts of the particles are singlets under the  $SU(2)_L$  symmetry. In addition to global symmetries, the Standard Model Lagrangian is required to have local symmetries allowing different transformations at different space-time points. In order to permit the local symmetries, gauge fields are introduced to couple to the fermion fields, and these can be identified with the fundamental forces of the Standard Model. As a result, the bosons that mediate the interactions are referred to as gauge bosons. The gauge fields introduced are:

- $B$  for the Abelian  $U(1)_Y$  symmetry,
- $W^i$  ( $i = 1, 2, 3$ ) for the non-Abelian  $SU(2)_L$  symmetry,
- $G^a$  ( $a = 1, \dots, 8$ ) for the non-Abelian  $SU(3)_C$  symmetry.

The  $SU(2)_L \times U(1)_Y$  symmetry unifies the weak and electromagnetic interactions and produces four gauge bosons from the gauge fields

$$\begin{aligned} W^+ &= (-W^1 + iW^2)/\sqrt{2} \\ W^- &= (-W^1 - iW^2)/\sqrt{2} \end{aligned} \quad (1.1)$$

and

$$Z^0 = \cos \theta_W W^3 - \sin \theta_W B \quad (1.2)$$

$$A = \sin \theta_W W^3 + \cos \theta_W B \quad (1.3)$$

where  $\theta_W$  is the weak mixing angle. The three bosons  $W^\pm$  and  $Z^0$  are the carriers for the weak force and  $A$  is the photon for the electromagnetic force. The  $SU(3)_C$  symmetry is only relevant for quarks and the gauge fields  $G^a$  represents the eight gluons that mediate the strong force.

The Standard Model Lagrangian is generally written as

$$\mathcal{L} = \sum_{f: \text{fermions}} \bar{f} i \gamma^\mu D_\mu f \quad (1.4)$$

where  $\gamma^\mu$  are the Dirac matrices. The covariant derivative  $D_\mu$  includes the three local gauge symmetries

$$D_\mu = \partial_\mu - ig_1 \frac{Y}{2} B_\mu - ig_2 \frac{\tau^i}{2} W_\mu^i - ig_3 \frac{\lambda^a}{2} G_\mu^a \quad (i = 1, 2, 3; a = 1, \dots, 8) \quad (1.5)$$

where  $Y$ ,  $\tau^i$  and  $\lambda^a$  are the generators of  $U(1)$ ,  $SU(2)$  and  $SU(3)$  transformations, and  $g_i$  is the coupling constant which determines the strength of the interaction with a value that has to be measured experimentally. In the following sections we will look closer at some of the aspects of the Standard Model.

## 1.2 The electroweak theory

As mentioned above, the  $SU(2)_L \times U(1)_Y$  component of the Standard Model gauge symmetry stands for a unification of the electromagnetic and weak interactions, known as electroweak theory [3]. The electromagnetic interaction is described by Quantum Electrodynamics (QED). It is an Abelian gauge invariant theory based on the  $U(1)_Q$  symmetry group with the gauge field  $A$ . The weak interaction is a flavour-changing, parity-violating force acting on quarks, leptons and gauge bosons. The charged-current interactions are mediated by the charged bosons  $W^\pm$  and the neutral-current interactions are carried by the neutral boson  $Z^0$ . The gauge bosons  $W^\pm$  and  $Z^0$  were subsequently observed in experiments and the masses were precisely measured ( $M_z = 91.1876 \pm 0.0021$  GeV,  $M_W = 80.398 \pm 0.025$  GeV [2]). Since the gauge invariance does not permit mass terms of gauge bosons, an  $SU(2)$  doublet of scalar fields, the Higgs field, is introduced to break the electroweak symmetry and meanwhile generates masses for the gauge bosons and fermions.

## 1.3 The Higgs mechanism

Under the assumption given by the Standard Model, the Higgs field is a doublet in the  $SU(2)$  space, carrying non-zero  $U(1)$  hypercharge, but is a singlet in colour space. The  $SU(2)_L \times U(1)_Y$  symmetry is spontaneously broken by the vacuum expectation value of the Higgs doublet. By interacting with the Higgs field, the gauge bosons and fermions acquire masses. The simplest way to achieve this breaking is to start with a single Higgs doublet

$$H = \begin{pmatrix} H^+ \\ H^0 \end{pmatrix} \quad (1.6)$$

where  $H^+$  and  $H^0$  are complex fields so that the Higgs field has in total four constituents. The potential of the Higgs field,

$$V(H) = \mu^2 H^\dagger H + \lambda (H^\dagger H)^2 \quad (1.7)$$

has a unique feature that its parameters  $\mu^2 < 0$  and  $\lambda > 0$ . Therefore, the potential is minimised at a non-zero value  $\sqrt{-\mu^2/2\lambda} = v/\sqrt{2}$ , known as the vacuum expectation value. We can always choose a direction in  $SU(2)$  space and expand the field around the minimum, such as

$$h_0 = \frac{1}{\sqrt{2}} \begin{pmatrix} 0 \\ v \end{pmatrix} \quad (1.8)$$

and

$$H(x) = h_0 + h(x) = \frac{1}{\sqrt{2}} \begin{pmatrix} 0 \\ v + h(x) \end{pmatrix} \quad (1.9)$$

Any arbitrary  $H(x)$  could be transformed and rotated to the form (1.9).

The gauge covariant derivative acting on any field,  $\psi$ , is already given previously in Eq. (1.5). If choosing  $\psi = H(x)$  as defined in Eq. (1.9), the electroweak symmetry  $SU(2)_L \times U(1)_Q$  is spontaneously broken to the  $U(1)_Q$  symmetry and the terms in the Lagrangian that produce gauge-boson masses are

$$\mathcal{L}_{\text{mass}} = \frac{g_2^2 v^2}{8} (W^1 W^1 + W^2 W^2) + \frac{v^2}{8} (g_2 W^3 - g_1 B)^2$$

The charged W-boson fields (Eq. (1.1)) have mass

$$M_W = \frac{g_2 v}{2} \quad (1.10)$$

Including the weak mixing angle  $\theta_W$

$$\sin \theta_W = \frac{g_1}{\sqrt{g_1^2 + g_2^2}}, \quad \cos \theta_W = \frac{g_2}{\sqrt{g_1^2 + g_2^2}} \quad (1.11)$$

the photon (Eq. (1.2)) is massless and the  $Z^0$  boson (Eq. (1.3)) has a mass given by

$$M_Z = \frac{\sqrt{g_1^2 + g_2^2}}{2} v = \frac{M_W}{\cos \theta_W} \quad (1.12)$$

After the electroweak symmetry breaking, three of the four Higgs components become the longitudinal parts of  $W^\pm$  and  $Z^0$ , and the fourth emerges as the physical Higgs boson with the mass  $m_H^2 = -2\mu^2$ . So far, the Higgs boson has not been observed so its mass remains an undetermined parameter in the Standard Model.

The  $SU(2)_L \times U(1)_Y$  gauge invariance prevents bare mass terms for the quarks and leptons. However, the Yukawa couplings of the Higgs doublet to two fermions are allowed, in forms of couplings to quark doublets, and either up- or down-type quark singlets, or lepton doublet and charged lepton singlets. These couplings turn into mass terms of fermions after the spontaneous symmetry breaking,

$$\mathcal{L}_{\text{mass}} = (m_u)_{ij} \bar{u}'_{Li} u'_{Rj} + (m_d)_{ij} \bar{d}'_{Li} d'_{Rj} + (m_e)_{ij} \bar{e}'_{Li} e'_{Rj} + \text{Hermitian conjugate} \quad (1.13)$$

Here the mass matrices are  $m_X = g_X v$ , where  $g_X$  are the Yukawa couplings constants, and  $q'$  denotes the weak eigenstate of a quark. Since there is no right-handed neutrino

field, neutrinos do not get mass from the Yukawa couplings. The mass matrices can be diagonalised by unitary transforms  $V(X, R)^\dagger m_X V(X, L)$ , leading to a change of basis from the weak eigenstates (e.g.  $u'_L$ ) to mass eigenstates (e.g.  $u_L$ ),

$$\begin{aligned} u'_L &= V(u, L)u_L, & u'_R &= V(u, R)u_R \\ d'_L &= V(d, L)d_L, & d'_R &= V(d, R)d_R \\ e'_L &= V(e, L)e_L, & e'_R &= V(e, R)e_R \end{aligned} \quad (1.14)$$

where  $V$  are unitary matrices. Consequently the charged current couplings are not diagonal in the mass basis, becoming

$$\mathcal{L}_{CC} = \frac{g_2}{\sqrt{2}} \bar{u}'_L \gamma^\mu d'_L W_\mu^+ = \frac{g_2}{\sqrt{2}} V_{CKM} \bar{u}_L \gamma^\mu d_L W_\mu^+ \quad (1.15)$$

where  $V_{CKM}$  is the Cabibbo-Kobayashi-Maskawa (CKM) matrix carrying the information about flavour mixing,

$$V_{CKM} = V(u, L)^\dagger V(d, L) = \begin{pmatrix} V_{ud} & V_{us} & V_{ub} \\ V_{cd} & V_{cs} & V_{cb} \\ V_{td} & V_{ts} & V_{tb} \end{pmatrix} \quad (1.16)$$

Because of the unitarity of the transformations, there is no flavour mixing in the neutral current.

The CKM unitary matrix relies on 9 real parameters of which three can be represented by mixing angles and the others are phases. Furthermore, five of the phases can be absorbed into arbitrary phase rotations of the quark fields. So in all there are three independent mixing angles and one phase in the CKM matrix to be determined.

## 1.4 Quantum chromodynamics

Quantum Chromodynamics (QCD) is a non-Abelian gauge theory based on the  $SU(3)_C$  gauge group which represents the strong interaction between coloured quarks and gluons. The QCD Lagrange density function is

$$\mathcal{L}_{QCD} = -\frac{1}{4} F_{\mu\nu}^a F^{a\mu\nu} + \bar{q}(i\gamma^\mu D_\mu - m_q)q + \mathcal{L}_{\text{gauge-fixing}} + \mathcal{L}_{\text{ghost}} \quad (1.17)$$

Here  $\mathcal{L}_{\text{gauge-fixing}}$  means the choice of gauge that is defined for the gluon field, supplemented by the ghost Lagrangian  $\mathcal{L}_{\text{ghost}}$  to cancel the unphysical degrees of freedom.  $D_\mu = \partial_\mu - igG_\mu^a \lambda^a$  is the  $SU(3)$  colour covariant derivative and  $g$  is the coupling constant which determines the strength of the strong interaction.  $F_{\mu\nu}^a$  is the field strength tensor derived from the gluon field  $G_\mu^a$ ,

$$F_{\mu\nu}^a = \partial_\mu G_\nu^a - \partial_\nu G_\mu^a - gf^{ABC} G_\mu^B G_\nu^C \quad (1.18)$$

where  $f^{ABC}$  ( $A, B, C = 1, \dots, 8$ ) are the structure constants of the  $SU(3)$  group. The last term of  $F_{\mu\nu}^a$  gives rise to gluon self-interactions and ultimately to the property of asymptotic freedom which distinguishes QCD from QED.



In QCD, the running of the coupling constant  $\alpha_s$  ( $\alpha_s = g^2/4\pi$ ) is determined by the renormalisation group function

$$Q^2 \frac{\partial \alpha_s}{\partial Q^2} = \beta(\alpha_s) \quad (1.19)$$

where  $Q$  is the energy scale [4]. The  $\beta$  function is to lowest order  $-\beta_0 \alpha_s^2$  where

$$\beta_0 = \left( \frac{33 - 2N_q}{12\pi} \right) \quad (1.20)$$

At a given scale  $\mu$ , if both  $\alpha_s(\mu^2)$  and  $\alpha_s(Q^2)$  are in the perturbative region,

$$\alpha_s(Q^2) = \frac{1}{1/\alpha_s(\mu^2) + \beta_0 \ln(Q^2/\mu^2)} \quad (1.21)$$

Contrary to the QED case, the gluon self coupling makes the  $\beta$  function in QCD negative, since the number of quark flavours  $N_q$  is less than 17. As a result, the running coupling  $\alpha_s$  decreases at a larger  $Q^2$ . This phenomenon is known as *asymptotic freedom*. On the other hand, the coupling increases at a low energy, known as *confinement*. It is convenient to introduce a parameter  $\Lambda_{\text{QCD}}$  with the dimension of mass into the definition of  $\alpha_s(Q^2)$ ,

$$\alpha_s(Q^2) = \frac{12\pi}{(33 - 2N_q) \ln(Q^2/\Lambda_{\text{QCD}}^2)} \quad (1.22)$$

$\Lambda_{\text{QCD}}$  represents the scale at which the coupling constant diverges so that perturbation theory breaks down. Measurements from experiments have given the estimate of  $\Lambda_{\text{QCD}}$  to be around 200 MeV.

The masses of  $u$ ,  $d$  and  $s$  quarks are below the scale  $\Lambda_{\text{QCD}}$  so that the perturbative QCD calculations are not precise. In the massless limit, the light quark QCD has the  $SU(3)_L \times SU(3)_R$  chiral symmetry, so chiral perturbation theory is used to predict some properties of hadrons containing light quarks. The  $t$ ,  $b$  and  $c$  quark masses are far beyond  $\Lambda_{\text{QCD}}$ , thus the perturbative QCD effects dominate. Since the top quark usually decays rapidly before it hadronises, in practice the heavy quarks that can form hadrons are charm and bottom quarks, which are the main focus of this thesis.

## 1.5 Summary

The Standard Model is a gauge theory which successfully describes the fermions and their interactions mediated by the gauge bosons. In the framework of quantum field theory, the Standard Model is described by the following Lagrangian:

$$\mathcal{L} = \mathcal{L}_{\text{gauge}} + \mathcal{L}_{\text{Yukawa}} + \mathcal{L}_{\text{Higgs}} \cdot \quad (1.23)$$

The model has at least 18 free parameters which need to be determined by experiments:

- three gauge coupling constants  $g_1$ ,  $g_2$  and  $g_3$ ;

- three lepton masses  $m_e, m_\mu, m_\tau$ ;
- six quark masses  $m_u, m_d, m_s, m_c, m_b,$  and  $m_t$ ;
- four parameters in the CKM matrix: three mixing angles and one CP violating phase;
- two parameters of the Higgs potential:  $\lambda$  and  $\mu$ .

The Standard Model is able to describe phenomena in its domain, the scale of interactions of  $\mathcal{O}(100)$  GeV or below. However, it is not complete and there still exist a large variety of open questions which may need physics beyond the Standard Model.

- Although the gauge theory part of the Standard Model has been well tested, the mechanism of the electroweak symmetry breaking is still unclear since the Higgs boson has not been observed. In the Standard Model, all the particle masses are tied to the mass scale of the Higgs sector. If the Higgs mass is heavy, the self couplings to the  $W$  and  $Z$  boson grow. Therefore either the Higgs mass is less than about 800 GeV or the  $WW$  and  $ZZ$  interactions at the centre-of-mass energies of order 1 TeV will reveal new structure [5]. The LHC experiments running at the TeV scale are expected to provide information on the nature of the electroweak symmetry breaking.
- The electroweak and QCD forces, and the quarks and leptons, have not been unified into a simpler structure. Theories such as Grand Unified Theories (GUT) have attempted such unification.
- Physics beyond the current Standard Model is the eternal focus in particle physics. In theory, supersymmetry (SUSY) is one of the favoured candidates for physics beyond the Standard Model. As an extension of the Standard Model, it relates fermions and bosons, and postulates the existence of superpartners of all the particles: bosonic superpartners of fermions (squarks and sleptons), and fermionic superpartners of bosons (gluinos and gauginos). The SUSY model also predicts multiple Higgs bosons:  $h, H, A$  and  $H^\pm$ . Although the parameters of the SUSY model are uncertain, if to stabilise the Higgs potential, the SUSY masses should be in the region below or of order of 1 TeV. Furthermore, a subset of the SUSY models (mSUGRA) proposes that the SUSY breaking is mediated by gravity, which incorporates the gravitational interaction to particle physics.

Moreover, because the Higgs boson in the Standard Model has not been observed, some other models have proposed different assumptions of the symmetry breaking. There are also many theories providing solutions to questions such as flavour mixing, CP-violation in strong interactions, new generation of particles and so on. The unsolved areas in particle physics request evidence from observations, therefore they supply great new physics potential for experiments to exploit.



# Chapter 2

## Heavy quark physics

### 2.1 Heavy quark production

In hadron-hadron collisions, the leading-order processes for a heavy quark production contain both light quark annihilation and gluon-gluon fusion such as

$$\begin{aligned}
 (a) \quad & q(p_1) + \bar{q}(p_2) \rightarrow Q(p_3) + \bar{Q}(p_4) \\
 (b) \quad & g(p_1) + g(p_2) \rightarrow Q(p_3) + \bar{Q}(p_4)
 \end{aligned}
 \tag{2.1}$$

Figure. 2.1 shows the leading-order Feynman diagrams of these processes which contribute to the matrix elements in  $\mathcal{O}(\alpha_s)$ .

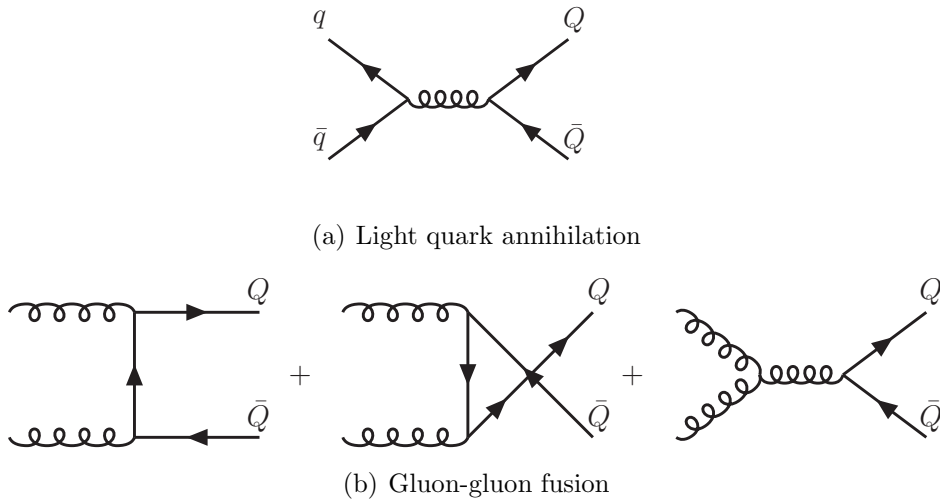


Figure 2.1: Leading-order Feynman diagrams for heavy quark production [4]

In the centre-of-mass frame of the incoming hadrons, we can write the parton four-momenta as

$$\begin{aligned}
 p^\mu &= (E, p_x, p_y, p_z) \\
 &= (m_T \cosh y, p_T \sin \phi, p_T \cos \phi, m_T \sinh y)
 \end{aligned}
 \tag{2.2}$$

where the transverse mass is defined as  $m_T = \sqrt{p_T^2 + m^2}$ . The rapidity  $y$  is given by

$$y = \frac{1}{2} \ln \left( \frac{E + p_z}{E - p_z} \right) \quad (2.3)$$

The propagators in the diagrams (Fig. 2.1) are expressed in terms of  $m_T$  and  $y$ :

$$\begin{aligned} (p_1 + p_2)^2 &= 2p_1 \cdot p_2 = 2m_T^2(1 + \cosh \Delta y) \\ (p_1 - p_3)^2 - m^2 &= -2p_1 \cdot p_3 = -m_T^2(1 + e^{-\Delta y}) \\ (p_2 - p_3)^2 - m^2 &= -2p_2 \cdot p_3 = -m_T^2(1 + e^{\Delta y}) \end{aligned} \quad (2.4)$$

where  $\Delta y = y_3 - y_4$  is the rapidity difference between the heavy quarks. They are all off-shell by a quantity of order  $m^2$ . It means that in the production of a heavy quark, the lower cut-off on the virtuality of the propagators is provided by the heavy quark mass  $m_Q$ . As  $m_Q > \Lambda_{\text{QCD}}$ , the heavy quark production should be described by perturbative QCD. The cross section is proportional to  $\alpha_s^2$ , with  $\alpha_s$  evaluated at the heavy quark mass scale.

The cross section for a hard scattering process initiated by two hadrons with momenta  $P_1$  and  $P_2$  is written as

$$\sigma(P_1, P_2) = \sum_{i,j} \int dx_1 dx_2 f_i(x_1, \mu^2) f_j(x_2, \mu^2) \hat{\sigma}_{ij}(p_1, p_2, \alpha_s(\mu^2), Q^2/\mu^2) \quad (2.5)$$

where  $x_i$  is the fraction of the momenta of those partons in the incoming hadron that participate in the hard interaction. The characteristic scale of the hard scattering is denoted by  $Q$ . The functions  $f_i(x, \mu^2)$  are the QCD parton distributions defined at a factorisation scale  $\mu$ . A parton emitted with a small transverse momentum less than  $\mu$  is considered to be absorbed into the parton distribution while a parton with a large transverse momentum contributes to the cross section. The short-distance cross section for the scattering of partons of types  $i$  and  $j$  is denoted by  $\hat{\sigma}_{ij}$ . To the leading order, the differential parton cross section is obtained from the invariant matrix element

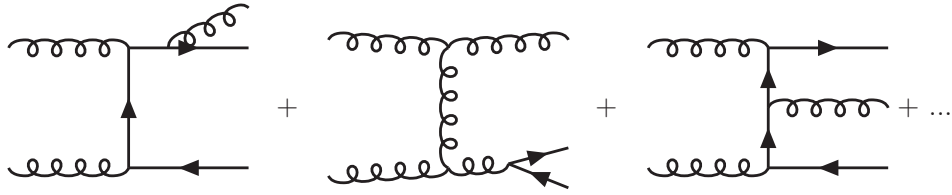
$$\begin{aligned} \frac{d\hat{\sigma}_{ij}}{dy_3 dy_4 d_{p_T}^2} &= \frac{1}{16\pi^2 \hat{s}^2} \overline{\sum} |M_{ij}|^2 \\ &= \frac{1}{64\pi^2 m_T^4 [1 + \cosh(\Delta y)]^2} \overline{\sum} |M_{ij}|^2 \end{aligned} \quad (2.6)$$

where  $\hat{s} = (p_1 + p_2)^2$ , and  $1/(2\hat{s})$  is the parton flux for massless incoming particles. The matrix elements squared from the two production processes have been averaged (summed) over initial (final) colours and spins in  $\overline{\sum} |M_{ij}|^2$ . So the integrated cross section is suppressed by a power of  $m_T^2$ .

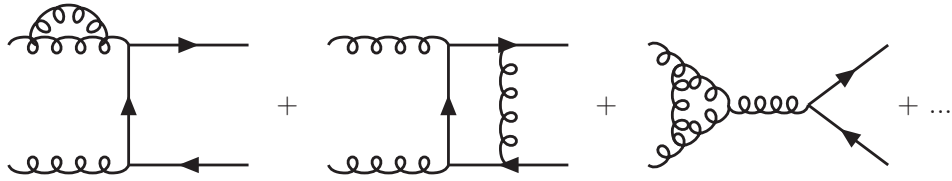
Including higher-order corrections, the short-distance cross section in Eq. (2.5) is expressed as

$$\hat{\sigma}_{ij}(s, m^2, \mu^2) = \frac{\alpha_s^2(\mu^2)}{m^2} \mathcal{F}_{ij} \left( \rho, \frac{\mu^2}{m^2} \right) \quad (2.7)$$

where  $\rho = 4m^2/\hat{s}$ . It is the dimensionless function  $\mathcal{F}_{ij}$  that involves a perturbative expansion and details about the full calculation of the functions  $F_{ij}^{(1)}$  are given in Ref. [6].



(a) Real emission diagrams



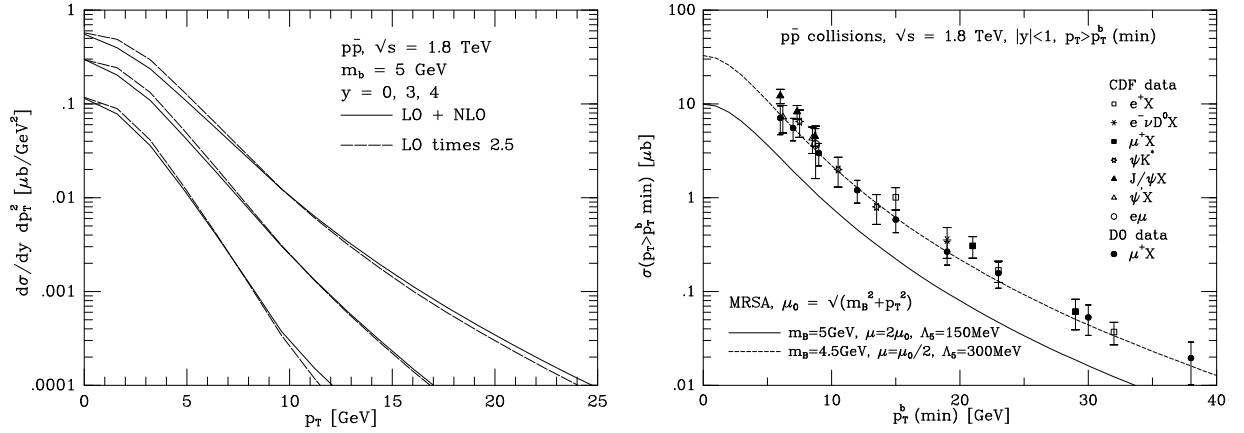
(b) Virtual emission diagrams

Figure 2.2: Higher-order corrections to the heavy quark production [4].

Examples of the higher-order corrections to the cross section are illustrated in diagrams in Fig. 2.2, involving both real and virtual corrections.

The theoretical uncertainties on the prediction of the next-to-leading order cross section are dominated by the heavy quark mass  $m$ . As the mass decreases, the value of  $x$  at which the parton distributions are evaluated become smaller and the cross section rises because of the growth of the parton flux. Secondly, the value of the strong coupling  $\alpha_s$  is correlated with the shape of the gluon distribution and can therefore also introduce uncertainty. The comparisons in Ref. [7] conclude that within the large uncertainties in the theoretical estimates, current data on the hadroproduction of charm quarks can be explained with a charm quark mass of the order of 1.5 GeV. The theoretical uncertainty for bottom quark production at collider energies is very large. The reason is the very small value of  $x$  at which the parton distributions are probed. Studies of the Tevatron<sup>1</sup> data ( $\sqrt{s} = 1.8$  TeV) show that the bottom cross section is sensitive to the gluon distribution function at values of  $x < 10^{-2}$  where the measurements are not precise. Nevertheless, the shape of the transverse momentum and rapidity distributions is well described by lowest-order perturbation theory as demonstrated in Fig. 2.3(a) where the calculation including the next-to-leading-order correction is also shown. In addition, Fig. 2.3(b) depicts the theoretical prediction for the  $p_T$  dependence of the bottom production cross section at the Tevatron and data from the CDF and D0 collaborations. The data appear to agree with the theoretical calculation within the theoretical uncertainties.

<sup>1</sup>a proton-antiproton accelerator and collider at FermiLab with two experiments, D0 and CDF.



(a) Predicted  $p_T$  distribution for bottom quark production at 1.8 TeV  $p\bar{p}$  collisions [6]

(b) The cross section for bottom production at Tevatron [8,9]

Figure 2.3: Calculations of the  $p_T$  distribution for bottom quark production in 1.8 TeV  $p\bar{p}$  collisions at leading order, and including next-to-leading-order 2.3(a) and the  $p_T$  dependence of the bottom production at the Tevatron 2.3(b).

## 2.2 Heavy quark decays

The decays of hadrons containing  $c$  and  $b$  quarks can be treated by the *spectator model* [4] where quarks that accompany the heavy quark  $Q$  in the hadron are assumed to play no role in the decay. Considering only the CKM-favoured decay modes, the main decay channels for  $b$  quarks are  $b \rightarrow c\bar{u}d, c\bar{c}s, c\bar{l}\bar{\nu}_l$  ( $l = e, \mu, \tau$ ), and for  $c$  quarks are  $c \rightarrow s\bar{d}u, s\bar{\mu}\nu_\mu, s\bar{e}\nu_e$ , as illustrated in Fig. 2.4.

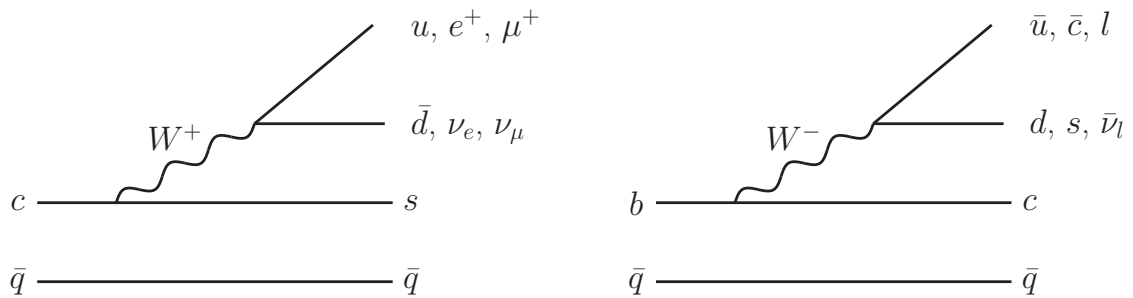


Figure 2.4: CKM-favoured spectator diagrams for  $c$  meson (left) and  $b$  meson (right) decays.

The semileptonic width, taking into account the finite masses of the quarks, is found to be

$$\Gamma_{sl}^Q = \frac{G_F^2 m_Q^5}{192\pi^3} |V_{Qq}|^2 f\left(\frac{m_q}{m_Q}\right) \quad (2.8)$$

where  $G_F$  is the Fermi constant and the function  $f(\epsilon)$  is given by

$$f(\epsilon) = (1 - \epsilon^4)(1 - 8\epsilon^2 + \epsilon^4) - 24\epsilon^4 \ln \epsilon \quad (2.9)$$

Including the CKM-disfavoured mode  $c \rightarrow d$ , the semileptonic decay width of the  $c$  quark is

$$\Gamma_{sl}^{(c)} = \Gamma_0(m_c) [f(m_s/m_c)|V_{cs}|^2 + f(m_d/m_c)|V_{cd}|^2] \quad (2.10)$$

with uncertainties subject to the quark mass and the strong interaction corrections. As for the  $b$  quark, the contribution from the CKM-disfavoured mode to the total semileptonic decay rate is negligible, so the theoretical decay width is

$$\Gamma_{sl}^{(b)} = \Gamma_0(m_b)f(m_c/m_b)|V_{cb}|^2 \quad (2.11)$$

Strong interactions will somewhat modify this formula.

The spectator model can be extended to predict the hadronic decay of a heavy quark as long as the final state develops independently of the other quarks in the heavy hadron. The width for the hadronic decay in the spectator model is simply given by the weak decay of the heavy quark followed by the subsequent decay of the resulting virtual  $W$  boson. Because of the three colours of quarks, the hadronic decay is three times as likely as the semileptonic decay to  $e\nu_e$  or  $\mu\nu_\mu$ , if we ignore strong interaction effects. In that case the spectator model predicts branching ratios

$$\begin{aligned} BR(c \rightarrow eX) &= \frac{1}{1 + 1 + 3} \\ BR(b \rightarrow eX) &= \frac{1}{3 \times (1 + 0.2) + 2 + 0.2} = 0.17 \end{aligned} \quad (2.12)$$

For B decays, the phase spaces for the final states ( $c\bar{c}s$  and  $c\tau\bar{\nu}_\tau$ ) are reduced to about 20% of the  $c\bar{u}d$  mode due to the heavy masses involved.

According to the spectator model, lifetimes for all charmed or bottomed hadrons are equal. However, it is inconsistent with the lifetime difference between  $D^+$  and  $D^0$  [2]. The failure is caused by the strong hadronic resonances and final state interactions in D meson decays. For B mesons, the modifications to the spectator predictions are smaller.

## 2.3 Quarkonium

A bound state of a heavy quark-antiquark pair,  $Q\bar{Q}$ , is called quarkonium. The first quarkonium state, which is made up of  $c\bar{c}$  and named  $J/\psi$ , was discovered in late 1974 when a narrow vector state of mass around 3.1 GeV, decaying into  $e^+e^-$  and  $\mu^+\mu^-$ , was observed simultaneously at Brookhaven and SLAC [10]. The analogous bound state in the  $b$  sector was later seen with the observation of the  $\Upsilon(1S)$  at Fermilab in 1977. Since the discoveries of  $J/\psi$  and  $\Upsilon$ , many excited levels of these  $Q\bar{Q}$  systems have been discovered subsequently. Because the top quark decays before forming a bound state, only charmonium ( $c\bar{c}$ ) and bottomonium ( $b\bar{b}$ ) have been found by experiments. Meanwhile, the ground state in the



intermediate  $b\bar{c}$  (and  $\bar{b}c$ ) system, the  $B_c$  meson, has also been observed [11]. Models which describe the  $c\bar{c}$  and  $b\bar{b}$  systems should also be able to predict the  $b\bar{c}$  (and  $\bar{b}c$ ) system and therefore measurements on the properties of the  $B_c$  meson, which are not precise at present, will serve as complementary tests of the theoretical models for quarkonium.

### 2.3.1 Quarkonium spectrum

A quarkonium state is characterised by the radial excitation level  $n$ , the total spin of the quark-antiquark pair  $S$ , the total orbital angular momentum  $L$ , and the total angular momentum  $J$  ( $J = L + S$ ). In the framework of non-relativistic QCD, charge conjugation  $C = (-1)^{L+S}$  and parity  $P = (-1)^{L+1}$  are conserved in the quarkonium system, so that the notation  $J^{PC}$  is also used to label the quarkonia. As the quark-antiquark pair must be in an angular momentum state consistent with the quantum numbers of the meson, sometimes the spectroscopic notation  $n^{2S+1}L_J$  is also invoked. Table 2.1 summarises the masses of the observed quarkonia along with their notations.

Meson	$n^{2S+1}L_J$	$J^{PC}$	Mass [MeV]
$\eta_c(1S)$	$1^1S_0$	$0^{-+}$	$2980.4 \pm 1.2$
$J/\psi(1S)$	$1^3S_1$	$1^{--}$	$3096.916 \pm 0.011$
$\chi_{c0}(1P)$	$1^3P_0$	$0^{++}$	$3414.75 \pm 0.31$
$\chi_{c1}(1P)$	$1^3P_1$	$1^{++}$	$3510.66 \pm 0.07$
$h_c(1P)$	$1^1P_1$	$1^{+-}$	$3525.93 \pm 0.27$
$\chi_{c2}(1P)$	$1^3P_2$	$2^{++}$	$3556.20 \pm 0.09$
$\eta_c(2S)$	$2^1S_1$	$0^{-+}$	$3637 \pm 4$
$\psi(2S)$	$2^3S_1$	$1^{--}$	$3686.09 \pm 0.04$
$\eta_b$	$1^1S_0$	$0^{-+}$	$9388.9^{+3.1}_{-2.3} \pm 2.7$ [12]
$\Upsilon(1S)$	$1^3S_1$	$1^{--}$	$9460.30 \pm 0.26$
$\chi_{b0}(1P)$	$1^3P_0$	$0^{++}$	$9859.44 \pm 0.42 \pm 0.31$
$\chi_{b1}(1P)$	$1^3P_1$	$1^{++}$	$9892.78 \pm 0.26 \pm 0.31$
$\chi_{b2}(1P)$	$1^3P_2$	$2^{++}$	$9912.21 \pm 0.26 \pm 0.31$
$\Upsilon(2S)$	$2^3S_1$	$1^{--}$	$10023.26 \pm 0.31$
$\chi_{b0}(2P)$	$2^3P_0$	$0^{++}$	$10232.5 \pm 0.4 \pm 0.5$
$\chi_{b1}(2P)$	$2^3P_1$	$1^{++}$	$10255.46 \pm 0.22 \pm 0.50$
$\chi_{b2}(2P)$	$2^3P_2$	$2^{++}$	$12268.65 \pm 0.22 \pm 0.50$
$\Upsilon(3S)$	$3^3S_1$	$1^{--}$	$10355.2 \pm 0.5$

Table 2.1: Standard notations of quarkonia and their masses [2].

Figures 2.5 and 2.6 illustrate the spectra of the current known  $c\bar{c}$  and  $b\bar{b}$  states and their decays. The largest observed degrees of excitation come from the  $\psi(nS)$  and  $\Upsilon(nS)$ , reaching up to  $n=6$  for the  $\Upsilon$  system. Excitation energies are relatively small compared with the scale of the bottomonium reduced mass  $\mu_b = m_b/2 \sim 2.5$  GeV, but not that of charmonium  $\mu_c \sim 0.8$  GeV.

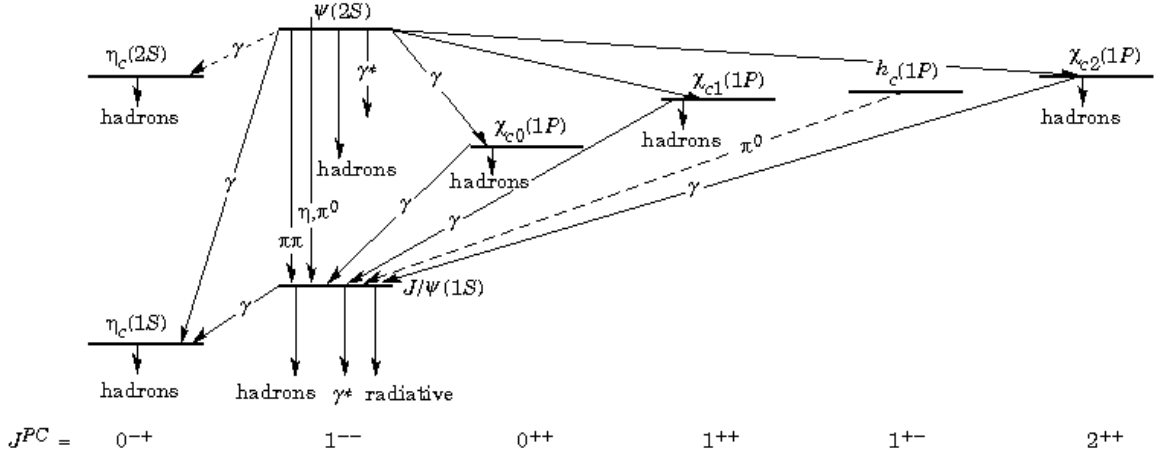


Figure 2.5: Current known states of the charmonium system and transitions. Uncertain states and transitions are indicated by dashed lines. The notation  $\gamma^*$  refers to decay processes involving intermediate virtual photons, including decays to  $e^+e^-$  and  $\mu^+\mu^-$  [2].

Many theoretical models have attempted to provide interpretations of quarkonium systems. The following subsections will present some of these models.

### Non-relativistic potential model

The potential model is an effective theory in which the quarks move non-relativistically inside hadrons. In analogy to positronium, the system is considered to involve a typical velocity  $v$  given by  $\alpha_s$  evaluated at a scale corresponding to the typical size of the bound state

$$v \sim \alpha_s\left(\frac{1}{r}\right), \quad r \sim \frac{1}{mv} \quad (2.13)$$

Since  $v$  is larger than  $\alpha_s(m^2)$ , higher-order corrections to the non-relativistic approximation are potentially more important than higher-order perturbative corrections. So far the theoretical calculations of charmonium and bottomonium and their spectra measured by many experiments suggest that the potential of quarkonium possesses a radial dependence of an approximately Coulomb form at small distances due to gluon exchange

$$V(r) \sim -\frac{4}{3} \frac{\alpha_s(1/r^2)}{r} \quad (r \rightarrow 0) \quad (2.14)$$

and is confining at large distances due to increasing coupling strength,

$$V(r) \sim kr \quad (r \rightarrow \infty) \quad (2.15)$$

where  $k$  is the string tension and the factor of  $4/3$  arises from the  $SU(3)$  colour factors. Below we will briefly list several models that have been widely used for explaining the quarkonium spectroscopy. Although these potentials have different asymptotic behaviours

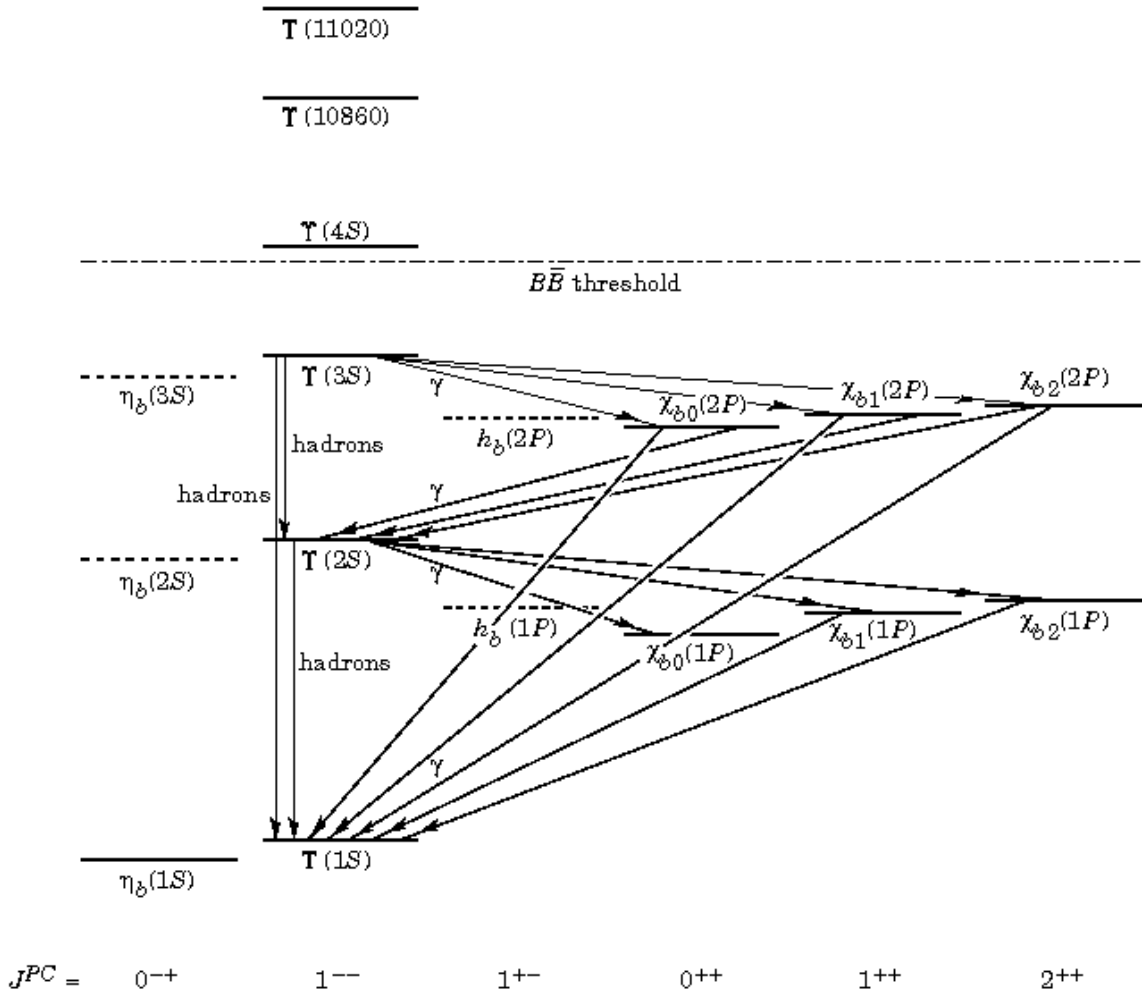


Figure 2.6: Experimentally established states (solid lines) of the  $b\bar{b}$  states and observed hadronic and radiative transitions. The threshold for open beauty production is shown along with  $\Upsilon$  states above it. [2]

at small and large distances, they coincide with each other in the region  $0.1 \text{ fm} < r < 1 \text{ fm}$ , where  $r$  is the average distances between heavy quarks in the  $c\bar{c}$  and  $b\bar{b}$  systems. Understanding the exact shape of the strong potential requires input from measurements of the  $b\bar{b}$ ,  $c\bar{c}$  and  $\bar{b}c$  systems.

### Cornell model [13]

$$V_C(r) = -\frac{4}{3} \frac{\alpha_s}{r} + \frac{r}{a^2} + c_0 \quad (2.16)$$

This model can describe the fine and hyperfine structures of charmonium levels in the leading non-relativistic treatment. In combination with charmonium data, the coefficients in this model have been determined as:

$$\alpha_s = 0.36, \quad a = 2.34 \text{ GeV}^{-1}, \quad c_0 = -0.25 \text{ GeV}, \quad m_c = 1.84 \text{ GeV} \quad (2.17)$$

### Logarithmic potential [14]

$$\begin{aligned} V_L(r) &= c_L + d_L \ln(\Lambda_L r) \\ \Lambda_L &= 1 \text{ GeV} \\ m_b &= 4.906 \text{ GeV}, \quad m_c = 1.5 \text{ GeV} \\ c_L &= -0.6635 \text{ GeV}, \quad d_L = 0.733 \text{ GeV} \end{aligned} \quad (2.18)$$

### Power (Martin) potential [15]

$$\begin{aligned} V_M(r) &= -c_M + d_M (\Lambda_M r)^k \\ \Lambda_M &= 1 \text{ GeV}, \quad k = 0.1 \\ m_b &= 5.174 \text{ GeV}, \quad m_c = 1.8 \text{ GeV} \\ c_M &= 8.064 \text{ GeV}, \quad d_M = 6.869 \text{ GeV} \end{aligned} \quad (2.19)$$

### Richardson potential [16]

$$V(q^2) = -\frac{4}{3} \frac{12\pi}{33 - 2n_f} \frac{1}{q^2} \frac{1}{\ln(1 + q^2/\Lambda^2)} \quad (2.20)$$

$V(r)$  is the Fourier transform of Eq. (2.20), with  $\Lambda = 398 \text{ MeV}$  based on the  $J/\psi$  data.

**Buchmüller-Tye potential [17]** In addition to the asymptotic and confining properties specified above in Eqs. (2.14) and (2.15), the Buchmüller-Tye potential covers the effects of two-loop running at small distances and an interpolation between the limits of small and large distance. The asymptotic limits of the static  $Q\bar{Q}$  potential can be described as

$$V(r) \sim kr \quad (r \rightarrow \infty) \quad (2.21)$$

$$V(r) \sim \frac{1}{r \ln(1/\Lambda_{\text{QCD}}^2 r^2)} \left[ 1 + \mathcal{O} \left( \frac{1}{\ln(1/\Lambda_{\text{QCD}}^2 r^2)} \right) \right] \quad (r \rightarrow 0) \quad (2.22)$$

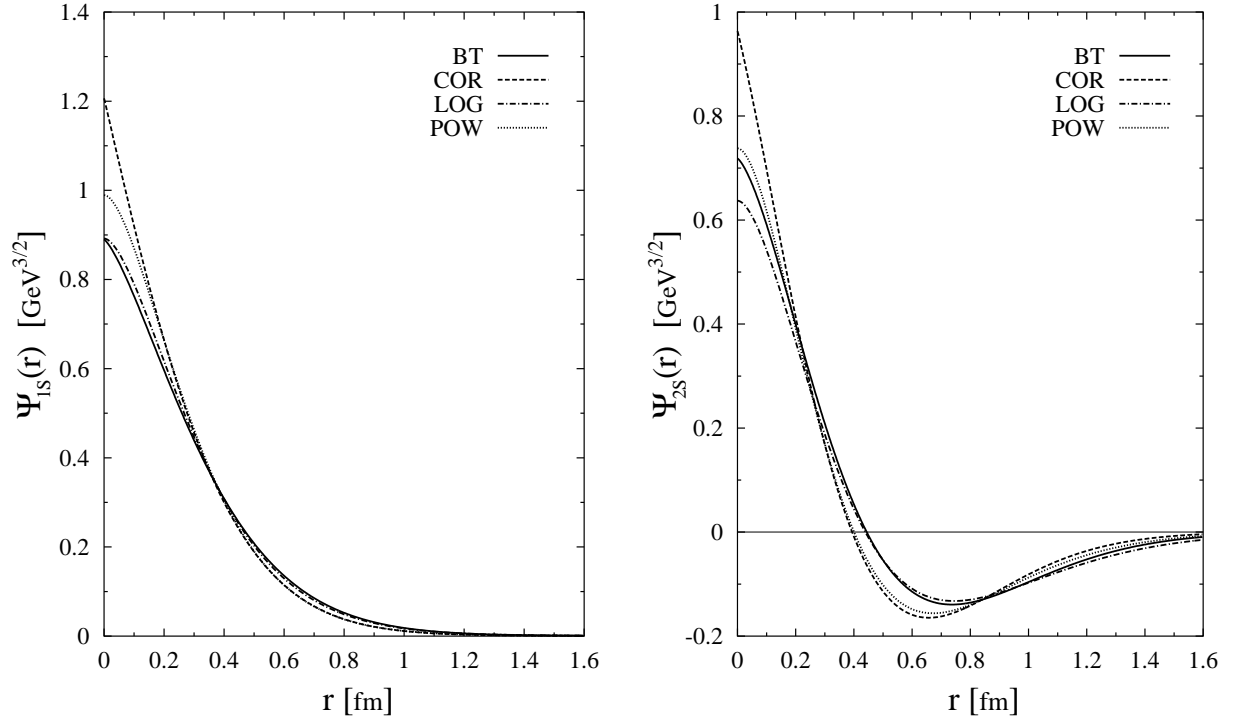


Figure 2.7: Radial wave functions  $\Psi_{nL}(r)$  for the  $J/\psi$  (left) and  $\psi(2S)$  states for potentials models: Buchmüller-Tye potential (BT), Cornell potential (COR), Logarithmic potential (LOG) and Power (POW) potential [18].

Energy levels and wave functions of the quarkonium system are obtained by solving the non-relativistic Schrödinger equation in terms of the constituent masses and the potential function. The wavefunction,  $\Psi(r) = \Psi_{nL}(r)Y_{Lm}(\theta, \phi)$ , with  $\Psi_{nL}(r)$  and  $Y_{Lm}(\theta, \phi)$  being the radial and orbital parts of the wavefunction, plays a key role in predictions of quarkonium properties. The radial wavefunctions from various potential models for the  $J/\psi$  and  $\psi(2S)$  are shown in Fig. 2.7, where the values of the wavefunctions at small values of  $r$  differ by up to 30%.

### Spin dependent potential

The potential model description can be extended by including the spin-dependent interactions. Starting from an interaction suggested by QED but allowing for a more general vertex structure, the expansion in inverse powers of the heavy quark masses yields a sum of static and spin-dependent contributions. The spin potential ( $V_{\text{spin}}$ ) contains spin-orbit ( $V_{LS}$ ), tensor ( $V_T$ ) and spin-spin ( $V_{SS}$ ) components giving the spin-singlet/triplet splittings,

$$V_{\text{spin}}(r) = V_{LS}(\mathbf{L} \cdot \mathbf{S}) + V_T(r) \left[ S(S+1) - \frac{3(\mathbf{S} \cdot \mathbf{r})(\mathbf{S} \cdot \mathbf{r})}{r^2} \right] + V_{SS}(r) \left[ S(S+1) - \frac{3}{2} \right] \quad (2.23)$$

and full calculations are included in Ref. [19].

## Lattice QCD

Lattice QCD attempts to solve the equations of QCD numerically on a discretised space time. The implementation of the lattice calculation is expected to demonstrate the potential picture as a consequence of QCD and specify the quark-antiquark potential itself. Results of lattice simulations [20,21] are consistent with parameterising the long-range part of the static  $Q\bar{Q}$  potential in pure  $SU(3)$  gauge theory as

$$V(r) = br - \frac{a}{r} + V_0 \quad (2.24)$$

where  $a$ ,  $b$ ,  $V_0$  are constants. The coefficient  $b$  is commonly described as the string tension in the lattice-gauge studies and its value is estimated from a string model relation involving the typical slope  $\alpha'$  of a hadronic Regge<sup>II</sup> trajectory

$$b = (2\pi\alpha')^{-1} \simeq 0.18 \text{ GeV}^2 \quad (2.25)$$

Numerical studies imply a relation between the string tension and the confinement scale  $\Lambda_{\overline{MS}}$ <sup>III</sup> in QCD.

$$\Lambda_{\overline{MS}} = (0.318 \pm 0.058)\sqrt{b} \simeq 0.13 \pm 0.02 \text{ GeV} . \quad (2.26)$$

### 2.3.2 Quarkonium production

Production of quarkonium states can be subdivided into two parts: first a heavy quark and antiquark pair is produced in the regime of perturbative QCD; then the formation of a bound state, which is driven by non-perturbative QCD. Since the discovery of  $J/\psi$ , many theoretical models have been proposed to interpret the rate of the quarkonium production measured by experiments. Below, some of these models are briefly introduced.

#### Colour Singlet Model

The leading order diagrams for the production of a  $Q\bar{Q}$  pair have already been shown in Fig. 2.1, where the quark-antiquark annihilation diagram produces a  $Q\bar{Q}$  pair in an octet state, and the gluon-gluon fusion mechanism produces a  $Q\bar{Q}$  pair in either a singlet or an octet state, but mainly the latter. The Colour Singlet Model (CSM) [23] assumes that any particular quarkonium state can only be produced from a heavy quark pair with the same quantum numbers. It means that the quark pair must have the same spin and colour state as the final quarkonium state, i.e. colour neutral. Then the formation of a quarkonium bound state is parameterised by non-perturbative theory in the CSM into one single term, assuming the constituent quarks are at rest in the meson frame, known as the static approximation. The short-distance cross section for the whole process is approximated in the CSM as:

$$d\hat{\sigma}(ij \rightarrow H + X) = d\hat{\sigma}(ij \rightarrow Q\bar{Q}[n^{2S+1}L_J] + X)|\Psi_{nL}^{(k)}(0)|^2 \quad (2.27)$$

<sup>II</sup>The slope of the Regge trajectory which classifies a ground state hadron and its rotational excitations [22]

<sup>III</sup>Modified minimal subtraction scheme, a particular renormalisation scheme which chops off the poles to eliminate divergences in perturbative calculations beyond the leading order.

where the radial wave functions at the origin can be extracted from the non-relativistic potential models introduced above. As the wave function  $\Psi_{nL}(0)$  is zero for P-wave states (e.g.  $\chi$  states), the calculation needs to consider the next term in the expansion of amplitude,  $\Psi'_{nL}(0)$ . At order  $\alpha_s^2$  there is only one diagram that can contribute as shown in Fig. 2.8(a) for the production of  $\eta$  and  $\chi$  states. Because of the C-parity conservation, the production of  $J/\psi$  from gluon-gluon fusion at leading order is forbidden, so it is described in the CSM at order  $\alpha_s^3$  as shown in Fig. 2.8(b). The CSM predicts that  $\sigma(J/\psi)$  should be smaller than  $\sigma(\chi_c)$  which is in disagreement with the data at fixed target energies where rather similar rates were observed [24]. Moreover, discrepancies between the CSM calculation and CDF data were also seen (as shown in Fig. 2.9).

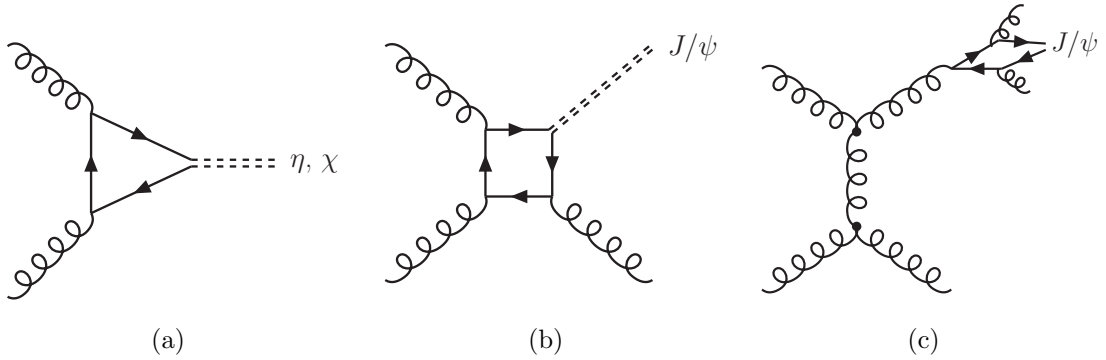


Figure 2.8: Leading order diagrams in the Colour Singlet Model for the production of  $\eta, \chi$  states (a) and  $J/\psi$  (b), and the gluon fragmentation in the CSM model(c).

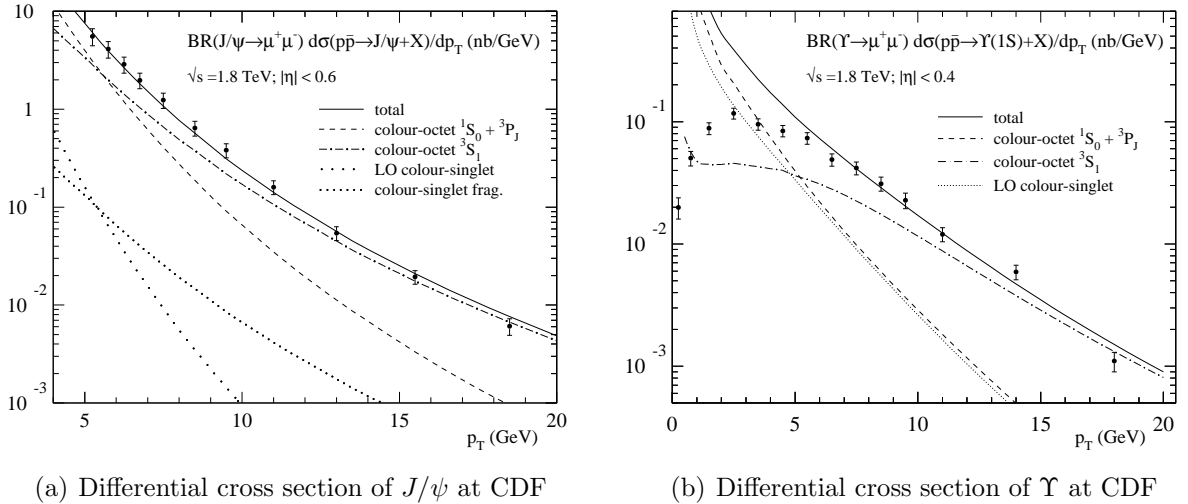


Figure 2.9: Differential cross section of  $J/\psi$  and  $\Upsilon$  productions at CDF, with theoretical predictions from colour singlet model and colour octet model [25]

### Fragmentation Contribution

In addition to the colour singlet model, fragmentation processes [26] were proposed to account for the discrepancies seen in CDF data. It suggests that a high  $p_T$  parton can fragment into a  $Q\bar{Q}$  pair which then hadronises into a heavy quarkonium state. An example of the diagram contributing to the  $J/\psi$  production through gluon fragmentation is shown in Fig. 2.8(c). For a leading order non-fragmentation singlet process, the produced quark and antiquark require an additional large momentum transfer to form a bound state, adding a power of  $1/p_T^2$  to the process. On the other hand, although the fragmentation process is of higher order in  $\alpha_s$ , it is enhanced by a power of  $p_T^4/(2m_Q)^2$  at large  $p_T$  and can therefore dominate the production at  $p_T \gg 2m_Q$ . As shown in Fig. 2.9(a), the differential production cross section of quarkonium rises at high  $p_T$  region in the colour singlet fragmentation model. This region will be the main region of study at the LHC experiments.

### Colour Octet Model

The Colour Octet Model (COM) [26,27] was proposed to extend the CSM calculation and solve the quarkonium deficit. It allows the heavy quark pair produced in the hard process to have different quantum numbers and evolve into a particular quarkonium state through radiation of soft gluons during hadronisation. This approach separates the perturbative hard process from the non-perturbative dynamics, in which the heavy bound states are inherently non-relativistic. The latter process can be described in the formalism of NRQCD (non-relativistic QCD) where a production cross section of a heavy quarkonium state  $H$  can be expressed as follows:

$$d\sigma(ij \rightarrow H + X) = \sum_{\mathcal{Q}} d\hat{\sigma}(Q\bar{Q}[\mathcal{Q}] + X') \langle O^H(\mathcal{Q}) \rangle \quad (2.28)$$

$d\hat{\sigma}(Q\bar{Q}[\mathcal{Q}] + X')$  describes the short-distance production of a  $Q\bar{Q}$  pair,  $Q\bar{Q}[\mathcal{Q}]$  is the Fock state component of the quarkonium wave function in the colour, spin, and angular momentum state  $\mathcal{Q} \equiv {}^{2S+1}L_J^{[1,8]}$ , and  $\langle O^H(\mathcal{Q}) \rangle$  is the vacuum expectation value of the operator describing the hadronisation into the final state  $H$ . Using NRQCD velocity scaling rules [27], the quarkonium state can be expanded in terms of the heavy quark velocity  $v$ , for example, the S-wave vector meson can schematically be written as:

$$\begin{aligned} |\Psi_{\mathcal{Q}}\rangle &= O(1)|Q\bar{Q}[{}^3S_1^{(1)}]\rangle + O(v)|Q\bar{Q}[{}^3P_J^{(8)}]g\rangle + O(v^2)|Q\bar{Q}[{}^1S_0^{(8)}]g\rangle \\ &+ O(v^2)|Q\bar{Q}[{}^3S_1^{(1,8)}]gg\rangle + O(v^2)|Q\bar{Q}[{}^3D_J^{(1,8)}]gg\rangle + \dots \end{aligned} \quad (2.29)$$

where at the lowest order in  $v$  it is reduced to the CSM case. For P-wave quarkonia, contributions from colour-octet S-wave states are at the same order in  $v$  as those from the leading colour-singlet P-wave states.

Although the parameters of the non-perturbative matrix elements in NRQCD are free, they are independent of the hard process, thus can be extracted from multiple experiments, the so-called ‘‘universality’’ of NRQCD. As seen in Fig. 2.9(a), the application of NRQCD in the COM model provides an acceptable description of the differential  $J/\psi$  production



cross section to CDF data. For the  $\Upsilon$  production in Fig. 2.9(b), corrections at low  $p_T$  are required [28].

There are also other models proposed for the quarkonium production (such as  $k_T$  factorisation) but none of them has fully explained Tevatron data for  $J/\psi$  and  $\Upsilon$ . The mechanism of heavy quarkonium production still contains many puzzles for future theoretical and experimental studies. The LHC data from higher energy collisions are expected to provide more information for testing the models.

## 2.4 Physics of $B_c$ mesons

The  $B_c$  meson is a bound state of the two different heavy quarks, bottom and charm. Because of its bare flavour, it is constrained to decay weakly, offering a unique window into heavy quark dynamics that is inaccessible through  $b\bar{b}$  and  $c\bar{c}$  states. Its mass is predicted over a large range by non-relativistic potential models, perturbative QCD, and lattice calculations. This section will present an overview of the theoretical predictions of the  $B_c$  meson properties. Sensitivity of observing  $B_c$  mesons experimentally will be covered in Chapter 5.

### 2.4.1 Mass spectrum

Concerning the spectroscopy, the  $\bar{b}c$  system can be treated as heavy quarkonium. As it is the only system consisting of two different heavy quarks, its mass spectrum can test the self-consistency of the models predicted based on charmonium and bottomonium data. Within the framework of the QCD non-relativistic potential models, it is advantageous to use the potential models whose parameters are flavour independent so that the parameters which were fixed by the  $c\bar{c}$  and  $b\bar{b}$  data do not need to be interpolated to the values in the intermediate region of the  $\bar{b}c$  systems. The potential models have been introduced in Sec. 2.3.1, and four of them have been reviewed for the  $\bar{b}c$  system in Ref. [29].

In accordance with the virial theorem, the average kinetic energy of the quarks in the bound state is determined by

$$\langle T \rangle = \frac{1}{2} \left\langle \frac{rdV}{dr} \right\rangle \quad (2.30)$$

For the logarithmic potential (Eq. (2.18)),  $\langle T_L \rangle$  is independent of the flavours. And in the Martin potential,

$$\langle T_M \rangle = \frac{k}{2+k} (c_M + E) \quad (2.31)$$

where  $E$  is the binding energy of the quarks in the quarkonium. Phenomenologically we can get  $|E| \ll c_M$  so that, neglecting the binding energy, the average kinetic energy of the heavy quarks is constant, independent of the quark flavours and the excitation number. The accuracy of such an approximation is about 10% [29]. According to the Feynman-Hellmann theorem, the system with reduced mass  $\mu$  has

$$\frac{dE}{d\mu} = -\frac{\langle T \rangle}{\mu} \quad (2.32)$$

Since  $\langle T \rangle$  is approximated to be constant, the energy difference for the radial excitations of the heavy quarkonium levels does not depend on the reduced mass of the system,

$$E(\bar{n}, \mu) - E(n, \mu) = E(\bar{n}, \mu') - E(n, \mu') \quad (2.33)$$

where  $\bar{n}$  and  $n$  refer to the different states of quarkonium with the reduced masses  $\mu$  and  $\mu'$ . Therefore, in the approximation of both the low value for the binding energy of quarks and no spin-dependent splitting, the heavy quarkonium state density is independent of the flavours

$$\frac{d\rho(n)}{dm_Q} = \text{constant} \quad (2.34)$$

Eq. (2.33) and (2.34) have been phenomenologically confirmed for the vector S-levels of the  $b\bar{b}$ ,  $c\bar{c}$ ,  $s\bar{s}$  system [30]. Solving the Schrödinger equation with the Martin potential (Eq. (2.19)), the average kinetic energies of the levels lying below the threshold for decaying into a B-D pair<sup>IV</sup> are presented in Table 2.2. The additional term to the radial potential due to the orbital rotation is

$$\Delta V_l = \frac{\vec{L}^2}{2\mu r^2} \quad (2.35)$$

which weakly influences the value of the average kinetic energy as shown in Table 2.2. Besides, for the level with  $L \neq 0$ , the binding energy is determined by the orbital rotation energy, which is independent of the quark flavours in the Martin potential. As a result, the structure of the non-split levels of the  $\bar{b}c$  system with  $L \neq 0$  must quantitatively repeat the structure of the charmonium and bottomonium levels.

nL	1S	2S	2P	3P	3D
$\langle T[GeV] \rangle$	0.35	0.38	0.37	0.39	0.39
$\Delta V_l[GeV]$	0.00	0.00	0.22	0.14	0.29

Table 2.2: Average kinetic and orbital energies of the quark motion in  $\bar{b}c$  system.

As mentioned before, when taking into account the spin-dependent potential, the mass splitting occurs. The spin potential in the  $\bar{b}c$  system has the form:

$$\begin{aligned} V_{spin}(\mathbf{r}) = & \left( \frac{\mathbf{L} \cdot \mathbf{S}_c}{2m_c^2} + \frac{\mathbf{L} \cdot \mathbf{S}_b}{2m_b^2} \right) \left( -\frac{dV(r)}{rdr} + \frac{8}{3}\alpha_s \frac{1}{r^3} \right) \\ & + \frac{4}{3}\alpha_s \frac{1}{m_c m_b} \frac{\mathbf{L} \cdot \mathbf{S}}{r^3} + \frac{4}{3}\alpha_s \frac{2}{3m_c m_b} \mathbf{S}_c \cdot \mathbf{S}_b [4\pi\delta(\mathbf{r})] \\ & + \frac{4}{3}\alpha_s \frac{1}{m_c m_b} [3(\mathbf{S}_c \cdot \mathbf{n})(\mathbf{S}_b \cdot \mathbf{n}) - \mathbf{S}_c \cdot \mathbf{S}_b] \frac{1}{r^3} \quad (\mathbf{n} = \mathbf{r}/r), \quad (2.36) \end{aligned}$$

where  $V(r)$  in the first term of Eq. (2.36) is the phenomenological potential confining the charm and bottom quarks in the system. The rest terms are the relativistic corrections

<sup>IV</sup>Refer to as BD threshold with the value  $M_{\text{threshold}} = M_B + M_D \approx 7.2$  GeV

arising from the one-gluon exchange between the two quarks, and  $\alpha_s$  is the effective constant of the quark-gluon interaction, which can be extracted from the observed splitting in the charmonium

$$M(J/\psi) - M(\eta_c) = \alpha_s \frac{8}{9m_c^2} |\Psi_{1S}(0)|^2 \approx 117 \text{ MeV}. \quad (2.37)$$

$\Psi_{1S}(0)$  is the value of the radial wave function at the origin calculated in the potential model. The corresponding  $\alpha_s$  is equal to 0.44 in the Martin potential.

As mentioned in Eq. (1.22), for the one-loop approximation at the scale  $p^2$ , the running coupling constant is determined as

$$\alpha_s(p^2) = \frac{12\pi}{(33 - 2N_f) \ln(p^2/\Lambda_{QCD}^2)} \quad (2.38)$$

Using the kinetic energy,

$$\langle T \rangle = \frac{\langle p^2 \rangle}{2\mu} \quad (2.39)$$

we have

$$\alpha_s(p^2) = \frac{12\pi}{33 - 2N_f} \ln(2\langle T \rangle \mu / \Lambda_{QCD}^2) \quad (2.40)$$

As the kinetic energy of the quark motion depends weakly on the heavy quark flavours, the effective coupling constant  $\alpha_s$  is basically determined by the reduced mass of the heavy quarkonium, in particular for the  $\Upsilon$  system. Thus when calculating the splitting of the  $\bar{b}c$  levels, the dependence of  $\alpha_s$  on the reduced mass of the heavy quarkonium should be taken into account. For the  $\bar{b}c$  system,  $\alpha_s$  is estimated by the Martin potential as in Table 2.3 [29].

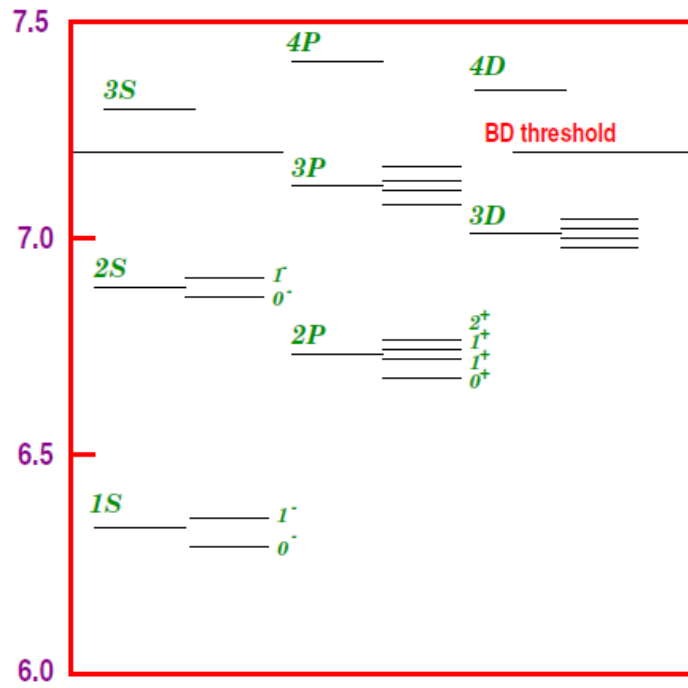
nL	1S	2S	2P	3P	3D
$\alpha_s$	0.394	0.385	0.387	0.382	0.383

Table 2.3: Effective coupling constants for different states in  $\bar{b}c$  system calculated with the Martin Potential.

In contrast to the  $LS$ -coupling in the  $\bar{c}c$  and  $\bar{b}b$  systems, Eq. (2.36) shows that there is a  $jj$ -coupling in the heavy quarkonium where the heavy quarks have different masses, like the  $\bar{b}c$  system. In this case,  $LS_c$  is diagonalised at the given  $J_c$  momentum ( $J_c = L + S_c, J = J_c + S_b$ ), and  $J$  is the total spin of the system. Consequently, instead of using the notation  $n^{2S+1}L_J$  as in the  $\bar{c}c$  and  $\bar{b}b$  system, we use the  $n^{2j_c}L_J$  to describe the split levels of the  $\bar{b}c$  system. The  $B_c$  mass spectrum, including the splittings is shown in Fig. 2.10 and Table 2.4<sup>V</sup>.

By now, theories have predicted the existence of 16 narrow ( $\bar{b}c$ ) states below the  $BD$  threshold (Fig. 2.10). Because there are no strong and electromagnetic annihilation decay

<sup>V</sup>The states  $2P1^+$  and  $2P1'^+$ ,  $3D2^-$  and  $3D2'^-$  are the mixings of the states with total quark spin  $S = 1$  and  $S = 0$ .

Figure 2.10: The mass spectrum of the  $B_c$  meson.

State	Mass [GeV] (Martin [15])	Mass [GeV] (Buchmüller-Tye [17])
$1^1S_0$	6.253	6.264
$1^1S_1$	6.317	6.337
$2^1S_0$	6.867	6.856
$2^1S_1$	6.902	6.899
$2^1P_0$	6.683	6.700
$2P\ 1^+$	6.717	6.730
$2P\ 1'^+$	6.729	6.736
$2^3P_2$	6.743	6.747
$3^1P_0$	7.088	7.108
$3P\ 1^+$	7.113	7.135
$3P\ 1'^+$	7.124	7.142
$3^3P_2$	7.134	7.153
$3D\ 2^-$	7.001	7.009
$3^5D_3$	7.007	7.005
$3^3D_1$	7.008	7.012
$3D\ 2'^-$	7.016	7.012

Table 2.4: The mass spectrum of the  $B_c$  meson.

channels for the  $\bar{b}c$  family below that threshold, the  $\bar{b}c$  excited states will transit radiatively into the ground long-lived pseudoscalar state in a cascade way with the emission of photons or  $\pi$  mesons. For detailed calculations we refer the readers to Ref. [31,32].

Another powerful tool in the study of the heavy quark bound state is the QCD sum rules [33,34,35], which attempt to connect different contributions: the loop calculations in the QCD perturbation theory and the non-perturbative calculations for the hadrons, with quark and gluon condensates. The calculations for the masses of the vector and pseudoscalar  $\bar{b}c$  states in the QCD sum rules agree with the potential model,

$$M(1^1S_0) \approx M(1^1S_1) \approx 6.3 - 6.5 \text{ GeV} . \quad (2.41)$$

However, the accuracy from the sum rules is lower because of the modelling of the non-resonant hadronic part of the current correlator and the parameters of the sum rule scheme.

Ref. [36] has shown that the lightest vector quarkonium could be presented by the QCD sum rules as

$$\frac{f_V^2 M_V^2}{M_V^2 - q^2} = \frac{1}{\pi} \int_{s_i}^{s_{th}} \frac{ds}{s - q^2} \text{Im}\Pi_V^{\text{QCD(pert)}}(s) + \Pi_V^{\text{QCD(nonpert)}}(q^2) \quad (2.42)$$

where  $\Pi_v$  is the vector correlator function,  $s_i = (m_c + m_b)^2$  is the kinematical threshold of the perturbative contribution,  $s_{th}$  is the threshold of the non-resonant hadronic contribution which is estimated to be equal to the perturbative contribution at  $s > s_{th}$ , and  $f_V$  is the leptonic constant of the vector state with the mass  $M_V$ . For the  $n$ th derivative of Eq. (2.42) at  $q^2 = 0$  we get

$$f_V^2 (M_V^2)^{-n} = \frac{1}{\pi} \int_{s_i}^{s_{th}} \frac{ds}{s^{n+1}} \text{Im}\Pi_V^{\text{QCD(pert)}}(s) + \frac{(-1)^n}{n!} \frac{d^n}{d(q^2)^n} \Pi_V^{\text{QCD(nonpert)}}(q^2) \quad (2.43)$$

So the mass of the vector  $B_c^*$  states can be obtained from the ratio of the  $n$ th derivative to the  $(n + 1)$ th one and the result depends on the  $n$  value and the Borel transformation parameter. Furthermore, the choice of the values for the hadronic continuum threshold energy and the quark mass shall also be taken into account. In fact, the dependence causes considerable parametric uncertainties in the estimates of the masses for the lightest pseudoscalar, vector, and scalar ( $\bar{b}c$ ) states.

### 2.4.2 $B_c$ decays

The  $B_c$  meson is expected to decay through the weak interaction. The decay process can be subdivided into three types:

- c-spectator mode ( $\bar{b} \rightarrow \bar{c}W^+$ ): the  $\bar{b}$  quark decays with the spectator c quark, leading to final states such as  $J/\psi l \bar{\nu}_l$  and  $J/\psi \pi$ , as in Fig. 2.11(a);
- b-spectator mode ( $c \rightarrow sW^+$ ): the c quark decays with the spectator  $\bar{b}$  quark, leading to final states such as  $B_s l \bar{\nu}_l$  and  $B_s \pi^+$ , as in Fig. 2.11(b);
- annihilation channel ( $\bar{b}c \rightarrow W^+$ ): giving final states such as  $B_c \rightarrow l \bar{\nu}_l(c\bar{s}, u\bar{s})$ , as in Fig. 2.11(c).

So the total width is the sum of the widths from the decay modes:

$$\Gamma = \Gamma_{\bar{b}} + \Gamma_c + \Gamma_{ann.} \quad (2.44)$$

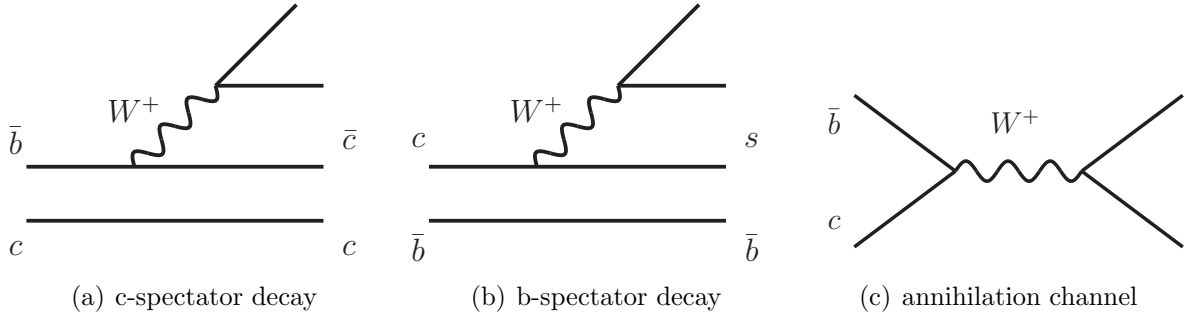


Figure 2.11: Diagrams of the three types of  $B_c$  decays.

The spectator mechanism gives the decay widths :

$$\Gamma_b = \frac{G_F^2 |V_{bc}|^2 m_b^5}{192\pi^3} \times 9 \quad (2.45)$$

$$\Gamma_c = \frac{G_F^2 |V_{cs}|^2 m_c^5}{192\pi^3} \times 5 \quad (2.46)$$

which can be approximated by  $\Gamma(B)$  and  $\Gamma(D)$ . The contribution from the annihilation channel is relatively small and the width can be reliably estimated in the framework of an inclusive approach,

$$\Gamma(ann.) = \sum_i \frac{G_F^2}{8\pi} |V_{bc}|^2 f_{B_c}^2 M_{B_c} m_i^2 \left(1 - \frac{m_i^2}{M_{B_c}^2}\right)^2 C_i \quad (2.47)$$

where  $C_i = 1$  for the  $\tau\nu_\tau$  channel and  $C_i = 3|V_{cs}|^2$  for the  $c\bar{s}$  channel, and  $m_i$  is the mass of the heaviest fermion ( $\tau$  or  $c$ ). In the case of non-leptonic decays, including the strong

interaction will enhance the widths in Eqs. (2.45), (2.46), and (2.47), due to the parameters in the non-leptonic weak Lagrangian, denoted as  $a_1$  and  $a_2$ .

In the framework of the inclusive approach, the width for the annihilation  $c\bar{s}$  channel is increased by a factor of  $a_1 = 1.22 \pm 0.04$  [37] when including the hard gluon corrections to the effective four-quark interaction of weak currents. As for the non-annihilation decays, in the approach of the Operator Product Expansion (OPE) [38] for the quark currents in weak decays, one takes into account the  $\alpha_s$  corrections to the free quark decays and the interference between the decaying quark and the spectator. In this way the  $\bar{b} \rightarrow \bar{c}c\bar{s}$  decay mode is suppressed due to the interference with the  $c$  spectator. Besides, the  $c$ -quark decays with the spectator  $b$ -quark are suppressed compared with the free quark decays due to a large bound energy in the initial state.

In the exclusive approach, widths of different decay modes calculated in the potential models are summed up. For the semileptonic decays, the hadronic final states are saturated by the lightest bound  $1S$ -state in the  $\bar{c}c$  system (i.e.  $\eta_c$  and  $J/\psi$ ) and the  $1S$ -states in the  $\bar{b}s$ -system (i.e.  $B_s$  and  $B_s^*$ ) due to the  $\bar{b} \rightarrow \bar{c}l^+\nu_l$  and  $c \rightarrow sl^+\nu_l$  transitions. The  $\bar{b} \rightarrow \bar{c}u\bar{d}$  channel can be calculated through the given decay width of  $\bar{b} \rightarrow \bar{c}l^+\nu_l$  taking into account the colour factor and hard gluon corrections to the four-quark interaction. Alternatively, it can be obtained as a sum over the widths of decays to the  $u\bar{d}$  bound states.

Regarding the main uncertainty related to the choice of quark masses (particularly for the charm quark), the calculation results for the total  $B_c$  width in the inclusive OPE and exclusive potential model approaches are consistent with each other [37]:

$$\tau[B_c^+]_{\text{OPE, PM}} = 0.55 \pm 0.15 \text{ ps} , \quad (2.48)$$

and also agrees with the measured result of  $B_c$  lifetime.

The calculation using the QCD sum rules takes into account the saturation of hadronic final states as in the exclusive potential model approaches, as well as the factorisation that relates the semileptonic and hadronic decay modes. The heavy quark masses are fixed in the QCD sum rules for bottomonia and charmonia, so that the accuracy of the sum rule calculations for the total width of  $B_c$  is determined by the choice of scale  $\mu$  for the hadronic weak Lagrangian in decays of  $c$  quark. Supposing that the preferred choice of scale in the  $c \rightarrow s$  decays of  $B_c$  is  $\mu^2 \approx (0.85 \text{ GeV})^2$ , in the framework of semi-inclusive sum-rule calculations, the prediction is [39]

$$\tau[B_c]_{\text{SR}} = 0.48 \pm 0.05 \text{ ps} . \quad (2.49)$$

Branching ratios of the exclusive  $B_c$  decays are calculated at the fixed values of correction factors  $a_{1,2}$  and  $B_c$  lifetime in Ref. [37]. For observing  $B_c$  mesons in the ATLAS experiment, the most favourable decay channels are  $B_c \rightarrow J/\psi + X$  ( $X$  means other possible decay products) because of the efficient muon triggers. Branching ratios for these channels calculated using QCD sum rules [37] are listed in Table 2.5. The values agree with the predictions based on the potential models, and the marginal deviations obtained in some potential models are also shown in Table 2.5. Relevant to our analysis work (described in Chapter 5) is the branching ratio of the hadronic channel  $B_c \rightarrow J/\psi\pi$ , which is estimated to be  $1.3 \times 10^{-3}$  [37]. The semileptonic channel  $B_c \rightarrow J/\psi e^+\bar{\nu}_l$  has a branching ratio of 1.9% [37].

Mode	BR, %
$B_c^+ \rightarrow J/\psi e^+ \nu$	1.9 [1]
$B_c^+ \rightarrow J/\psi \tau^+ \nu$	0.48 [0.35]
$B_c^+ \rightarrow J/\psi \pi^+$	0.13 [0.08]
$B_c^+ \rightarrow J/\psi \rho^+$	0.40 [0.2]
$B_c^+ \rightarrow J/\psi K^+$	0.011 [0.007]
$B_c \rightarrow J/\psi K^{*+}$	0.022 [0.016]
$B_c^+ \rightarrow J/\psi D_s^+$	0.17 [0.05]
$B_c^+ \rightarrow J/\psi D_s^{*+}$	0.67 [0.5]
$B_c^+ \rightarrow J/\psi D^+$	0.009 [0.002]
$B_c^+ \rightarrow J/\psi D^{*+}$	0.028 [0.014]

Table 2.5: Branching ratios of exclusive  $B_c^+$  decays with  $J/\psi$  in the decay products at the fixed choice of factors:  $a_1^b = 1.14$  and  $a_2^b = -0.20$  in the non-leptonic decays of  $\bar{b}$  quark. The lifetime of  $B_c$  is appropriately normalised by  $\tau[B_c] \approx 0.45$  ps. The numbers in square brackets present the marginal values obtained in some potential models in order to show the possible range of variation [37].

### 2.4.3 $B_c$ production

The production of  $B_c$  requires the joint production of the heavy quarks  $\bar{b}$  and  $c$ , which results in the low value of the  $B_c$  production cross section in comparison with the  $J/\psi$  and  $\Upsilon$  families. Similar to the quarkonium production, the production of  $B_c$  is determined by including the interactions:

1. the perturbative hard production of  $c\bar{c}$  and  $b\bar{b}$ ,
2. a soft non-perturbative binding of quarks in the final state, which can be estimated in the framework of non-relativistic potential models.

Therefore, the yield of  $B_c$  mesons is estimated to be of the order of  $10^{-3}$  with respect to beauty hadrons [40].

At LHC energies, the hadronic  $B_c$  production is dominated by gluon-gluon fusion  $gg \rightarrow B_c + b + \bar{c}$  because of the high gluon luminosity. To the leading approximation of QCD perturbation theory, the calculation requires contributions of 36 diagrams in the fourth order of the  $\alpha_s$ . The major mechanism for producing high momenta  $B_c$  mesons is heavy quark fragmentation [41] in which a  $\bar{b}$  quark is produced at a large momentum by a hard scattering and subsequently fragments into a meson,  $Q \rightarrow (Q\bar{q}) + q$ , factorised by:

$$\frac{d\sigma}{dp_T} = \int \frac{d\hat{\sigma}(\mu; gg \rightarrow Q\bar{Q})}{dk_T} \Big|_{k_T=p_T/x} \cdot D^{Q \rightarrow (Q\bar{q})}(x; \mu) \frac{dx}{x} \quad (2.50)$$

where  $\mu$  is the factorisation scale, and  $d\hat{\sigma}/dk_T$  the cross section for the gluon-gluon production of quarks  $Q\bar{Q}$ . The fragmentation function  $D^{\bar{b} \rightarrow B_c}(z, \mu)$  is determined by the



parameters  $\alpha_s$ ,  $m_b$ ,  $m_c$  and the radial wave function  $\Psi(0)$  of the bound state at the origin,

$$D_{\bar{b} \rightarrow B_c}(z, \mu_o) = \frac{2\alpha_s(2m_c)^2|\Psi(0)|^2}{81\pi m_c^3} \frac{rz(1-z)^6}{(1-(1-r)z)^6} \\ \times [6 - 18(1-2r)z + (21 - 74r + 68r^2)z^2 \\ - 2(1-r)(6 - 19r + 18r^2)z^3 + 3(1-r^2)(1-2r+2r^2)z^4] \quad (2.51)$$

where  $r = m_c/(m_b + m_c)$ . The calculation for the complete set of diagrams of  $\mathcal{O}(\alpha_s^4)$  has been estimated in Ref. [42] and the result determines a low boundary of the momentum region  $p_T^{min}$  where the production mechanism enters the regime of  $\bar{b}$ -quark fragmentation. The result of  $p_T^{min}$  from the calculation is much greater than  $M(B_c)$  [37], so that the fragmentation approximation is only valid for high  $p_T$  production  $p_T(B_c) > M(B_c)$ .

However, the convolution of the parton cross section with the gluon distributions inside the initial hadrons can suppress contributions at large transverse momenta, as well as the subprocesses with large energy in the center-of-mass system of the partons. So the main contribution to the total cross section of hadronic  $B_c$  production is given by the region of partonic energies less than or comparable to the  $B_c$  meson mass. In this region, the fragmentation model does not apply and instead the process of recombination of heavy quarks dominates. In Ref. [40], including all the contributions and using the CTEQ5L parameterisation for the parton distributions, the total hadronic cross sections for the  $B_c$  mesons is estimated to be  $0.8 \mu\text{b}$  at  $\sqrt{s} = 14 \text{ TeV}$ . Estimates of cross sections for different S-states are shown in Table 2.6. For P-wave states, the leading colour-singlet matrix element

$B_c$ state	$1S_0$	$1S_1$	$2S_0$	$2S_1$
cross section [ $\mu\text{b}$ ]	0.19	0.47	0.05	0.11

Table 2.6: Production cross section predicted for each  $B_c$  S-state at  $\sqrt{s} = 14 \text{ TeV}$ .

and the leading colour-octet matrix elements are both suppressed by a factor of  $v^2$  (relative velocity of the charm quark) with respect to the colour-singlet matrix element for S-wave. After summing over the different spin states, the total cross section for the production of P-wave levels is equal to 7% of the S-state cross section. In total, at the LHC with luminosity  $\mathcal{L} = 10^{34} \text{ cm}^{-2}\text{s}^{-1}$  and  $\sqrt{s} = 14 \text{ TeV}$ , we could expect  $4.5 \times 10^{10} B_c^+$  events per year.

Theoretical uncertainties on the  $B_c$  production come from the free parameters that are involved in Eq. (2.50). As shown previously in Fig. 2.7, different forms of the strong potential do not predict identical radial wave function at the origin,  $\Psi_{nL}(0)$ , which is included in the fragmentation model for the formation of  $B_c$  mesons (Eq. (2.51)). Therefore the shape of the strong potential can lead to uncertainties. And the choice of the quark mass value  $m_c$  and  $m_b$  can also generate uncertainties in Eq. (2.51). Besides, the choice of the factorisation scale ( $Q^2$ ), the running of  $\alpha_s$ , and the parton distribution function (PDF) are the main uncertainties in the perturbative production of  $Q\bar{Q}$  pairs. Uncertainties of the  $B_c$  cross section have been investigated in Ref. [43]. The choice of the energy scale of  $Q^2$  was found to give the biggest effect on the  $B_c^+$  production cross section (a factor around  $\frac{1}{3}$ ), as shown in Fig. 2.12.

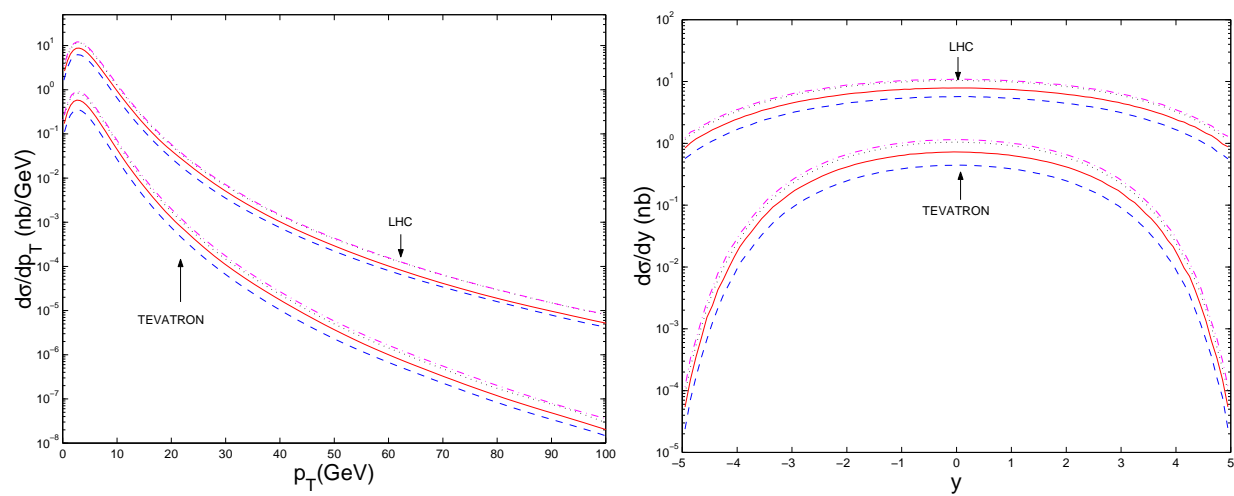


Figure 2.12:  $B_c$  differential distributions versus its transverse momentum  $p_T$  and rapidity  $y$  for four typical choices of the characteristic energy scale  $Q^2$ . The gluon distribution is chosen as CTEQ5L and the running  $\alpha_s$  is in leading order. The choice of  $Q^2$  is: solid line  $Q^2 = \hat{s}/4$ ; dotted line  $Q^2 = p_T^2 + m_{B_c}^2$ ; dashed line  $Q^2 = \hat{s}$ ; and dash-dot line  $Q^2 = p_{Tb}^2 + m_b^2$  ( $\hat{s}$ , the center-of-mass energy of the process). The upper (lower) three lines corresponding to the distributions in LHC (TEVATRON) [43].



# Chapter 3

## LHC and the ATLAS experiment

At present, the Large Hadron Collider (LHC) is the largest particle collider in the world. Since the first collision in 2009, the LHC keeps setting new records for the collision energy. Currently it is operating with proton-proton collisions steadily at an unprecedented centre-of-mass energy,  $\sqrt{s} = 7$  TeV, which will continue until the end of 2011. The energy is planned to be raised after a technical stop starting in 2011 to eventually reach the design energy of 14 TeV and the design luminosity of  $10^{34}$  cm<sup>-2</sup>s<sup>-1</sup>. There are six experiments at the LHC: the two large multi-purpose experiments, ATLAS (A Toroidal LHC ApparatuS) and CMS (Compact Muon Solenoid), which will be operated at the maximum available luminosity (up to the design peak luminosity of  $10^{34}$  cm<sup>-2</sup>s<sup>-1</sup>) to study the Standard Model symmetry breaking and new physics; the specialised large ion collider experiment, ALICE (A Large Ion Collider Experiment), planned for running with peak luminosity up to  $10^{27}$  cm<sup>-2</sup>s<sup>-1</sup> to study the quark-gluon plasma in lead ion collisions; the dedicated B physics experiment, LHCb (Large Hadron Collider beauty), which investigates invisible anti-matter using b quarks with a reduced luminosity of  $2 \times 10^{32}$  cm<sup>-2</sup>s<sup>-1</sup>; and two smaller-size experiments, LHCf (Large Hadron Collider forward) and TOTEM (TOTAl Elastic and diffractive cross section Measurement), which focus on physics in the forward particles.

The LHC experiments apply a standard definition of coordinates and observables for the studies of the detector performance and physics. The nominal interaction point defines the origin of the coordinate system while the beam direction defines the  $z$ -axis, and the  $x - y$  plane is the plane transverse to the beam direction. The positive  $x$ -axis is defined as pointing from the interaction point to the centre of the LHC ring, and the positive  $y$ -axis is pointing upwards. The azimuthal angle  $\phi$  is measured around the beam axis and the polar angle  $\theta$  is the angle with respect to the beam axis. The pseudorapidity is defined as  $\eta = -\ln \tan(\theta/2)$  and the transverse observables are defined in the  $x$ - $y$  plane, such as the transverse momentum  $p_T$  ( $p_T = p \sin \theta$ ), the transverse energy  $E_T$  and the missing transverse energy  $E_T^{\text{miss}}$ . Distances in the  $\eta - \phi$  space are defined as  $\Delta R = \sqrt{\Delta^2 \eta + \Delta^2 \phi}$ , and the impact parameters of tracks are defined using the variables:  $d_0$  the distance of closest approach of the track to the primary vertex in the  $r$ - $\phi$  projection, and  $z_0$  the  $z$  coordinate of the track at the point of closest approach. The five components  $(d_0, z_0, \phi_0, \theta, q/p)$  define the perigee parameters of a track at the closest approach to a reference point.

At the LHC design centre-of-mass energy, 14 TeV, the total  $b\bar{b}$  production cross section

from the proton-proton collisions is assumed to be  $500 \mu\text{b}$ . Among the LHC experiments, both the ATLAS and CMS detectors have the tracking systems covering the central rapidity region,  $|\eta| < 2.5$ . In view of trigger rates and pile-up, the initial running period will be most feasible for B-physics in these two experiments. On the other hand, the LHCb detector is a forward single-arm spectrometer covering  $1.9 < \eta < 4.9$ , and designed to perform B physics throughout its lifetime. In addition, the ATLAS and CMS experiments will apply a higher  $p_T$  threshold in the trigger system due to the limited bandwidth. The  $\eta$  and  $p_T$  coverages of the tracking systems in these experiments are illustrated in Fig. 3.1. For more details about the B physics programs in the LHC experiments, I refer readers to my document No.1 listed on Pg. ii.

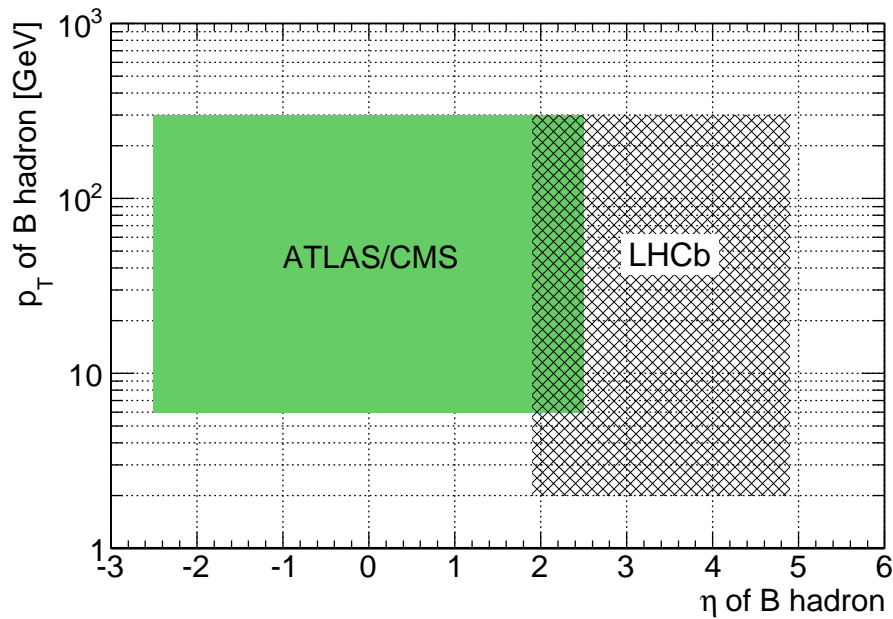


Figure 3.1: The  $\eta$  and  $p_T$  coverages of the detector tracking system for B physics measurements in the ATLAS, CMS and LHC experiments.

### 3.1 The LHC machine

The LHC [44] is a two-ring-superconducting hadron accelerator and collider at CERN. Installed in the 26.7 km long tunnel previously used for the electron-positron collider LEP, the gigantic LHC collider is designed to accelerate two counter-rotating particle beams (protons or lead ions) and collide them at high energy and luminosity. As illustrated in Fig. 3.2, the LHC rings are subdivided into 8 sectors, each of which comprises one arc section and one straight section. Each straight section is approximately 528 meters long serving as experimental or utility insertion. The ATLAS and CMS experiments are located at diametrically opposite straight sections, point 1 for ATLAS and point 5 for

CMS. At point 2 there is the ALICE experiment. The LHCb experiment is sited at point 8. TOTEM is located near the CMS detector and LHCf is next to the ATLAS detector. Meanwhile, point 2 and point 8 also contains injection systems for Beam 1 and Beam 2. Beam crossings only take place at these four locations. Each arc of the LHC is occupied by 46 half arc cells that are 53.45 m long. And each half arc cell contains one short straight section (SSS) holding one quadrupole magnet to focus or defocus beams, and three 14.3 meters long dipole magnets for beam accelerations. All dipole magnets of one arc form one electrical circuit while the quadrupoles of each arc form two electrical circuits, one from the focusing quadrupole magnets in Ring 1 and Ring 2, and the other one from the defocusing quadrupole magnets of Beam 1 and Beam 2.

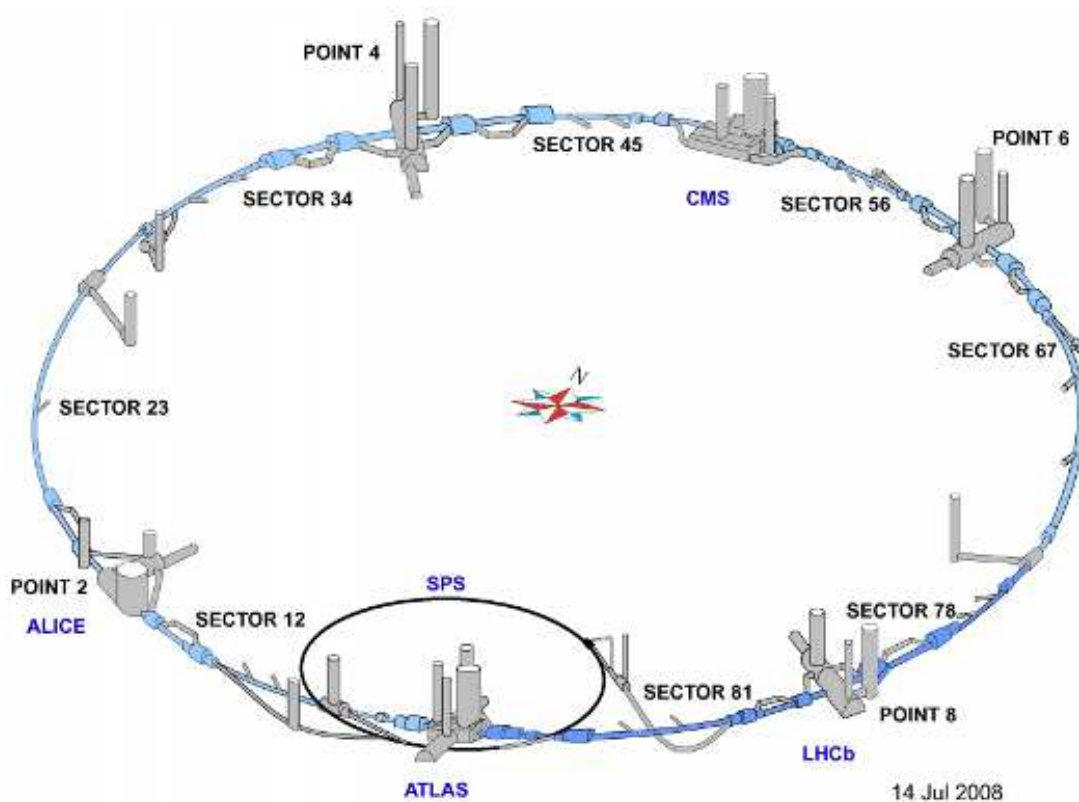


Figure 3.2: Overall view of the Large Hadron Collider and the experiments.

Inheriting the accelerator chain from the LEP<sup>1</sup>, the LHC makes use of the proton injector chain, Linac 2 - Proton Synchrotron Booster (PSB) - Proton Synchrotron (PS) - Super Proton Synchrotron (SPS). The injector complex is depicted in Fig. 3.3. Protons from the source Linac 2 are boosted in the PSB. Later the PSB delivers 6 bunches of protons in 2 batches to the PS. In the nominal mode of operation for filling the LHC, the PS splits proton bunches and finally injects 72 bunches of protons spaced by 25 ns in batches to the SPS. Next, the SPS accelerates the 26 GeV proton batches from the

<sup>1</sup>The Large Electron Positron (LEP) collider at CERN operated from 1989 to 2000.

PS to 450 GeV then transfer them to one or the other LHC ring via the transfer lines. The process is repeated until both rings are filled and then the beams are accelerated to the collision energy. The LHC operates proton-proton collisions which requires opposite magnetic dipole fields in both rings. Superfluid helium is used to cool the superconducting magnets to a temperature below 2 K and provides a magnetic field of 8.33 T corresponding to a beam energy of 7 TeV.

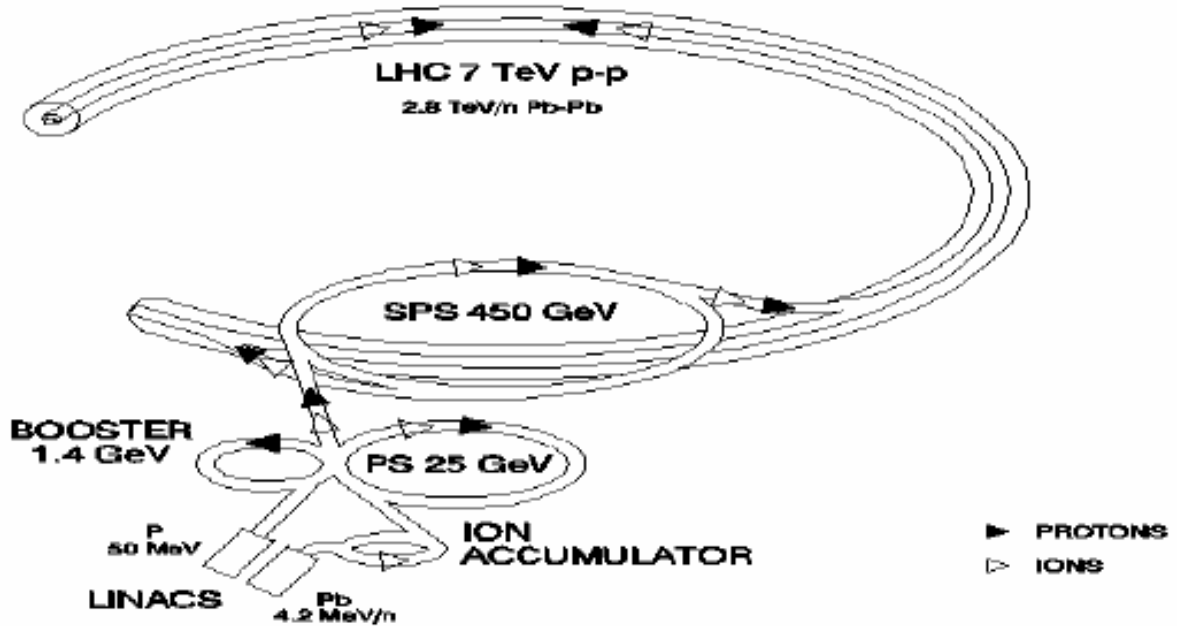


Figure 3.3: The LHC injector complex.

The heavy ion collisions have been scheduled to begin one year after the start-up of the proton collisions using beams of fully stripped lead ions which is expected to yield a total centre-of-mass energy of 1.15 PeV and a nominal luminosity of  $10^{27} \text{ cm}^{-2}\text{s}^{-1}$ . Collisions between ion beams will be provided at point 2 for the specialised ALICE experiment whilst the CMS and ATLAS detectors also plan to study ion collisions with similar luminosity. The injection scheme of lead ions starts with the lead linac delivering a pulse of  $\text{Pb}^{54+}$  to LEAR which cools the beam until a new linac pulse arrives. After the accumulation of 20 such batches, the beam contains  $1.2 \times 10^9$  ions captured in four buckets. The four bunches are then accelerated to 14.8 MeV/u and transferred directly into the PS. In the PS, the bunches are further accelerated to a momentum of 6.15 GeV/c/u and compressed. Afterwards, the SPS receives the four bunches in one batch and transfers it to either of the LHC rings.

## 3.2 The ATLAS experiment

ATLAS is a general-purpose detector at the LHC with the goal of exploring the new frontier in particle physics. The detector is designed to accommodate the wide spectrum of possible physics signature at the TeV mass scale where ground breaking discoveries are expected. Focus is on the investigation of the electroweak symmetry breaking and the search for the Higgs boson, as well as the search for physics beyond the Standard Model. The performance of the detector has also been optimised towards precision measurements of benchmark physics.

The ATLAS detector is a cylinder with an overall length of 44 m and a diameter of 25 m, forward-backward symmetric with respect to the interaction point. The layout of the detector is shown in Fig. 3.4 with four main subsystems: the inner detector (ID) which contains a pixel detector, a semiconductor tracker (SCT), and a transition radiation tracker (TRT), the electromagnetic and hadronic calorimeters, the muon chambers and the magnet system including a solenoid magnet serving for the ID and toroid magnets for the muon system. Details about these subsystems will be covered in this chapter.

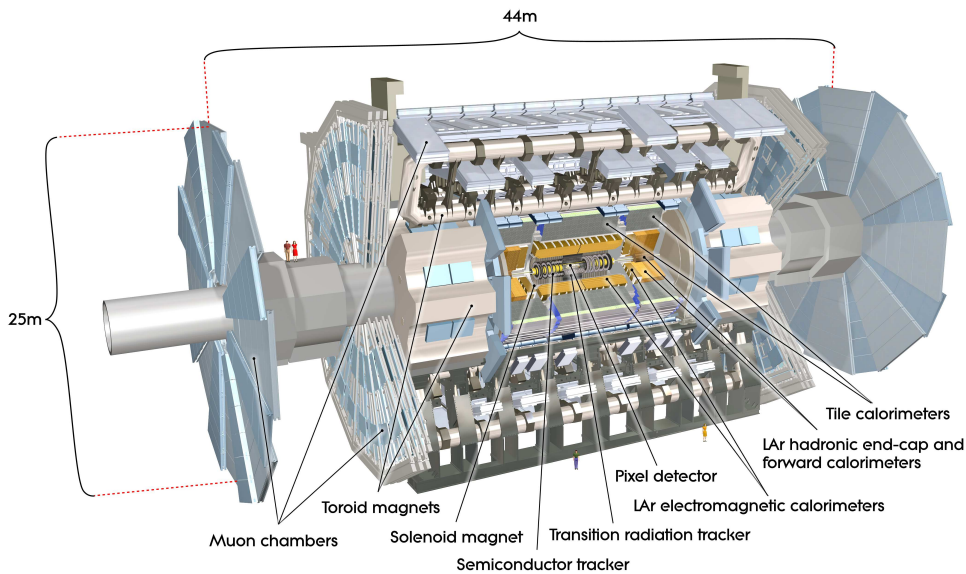


Figure 3.4: Cut-away view of the ATLAS detector [45].

### Inner detector

The inner detector plays a crucial role in momentum and vertex measurements, pattern recognition, and electron identification in ATLAS achieved by high granularity silicon pixel detectors (Pixel) and microstrip tracker (SCT), in combination with the straw tubes from the transition radiation tracker (TRT). The detector layout is illustrated in Fig. 3.5. It is 6.2 meters long and 2.1 meters high, immersed in a 2 T magnetic field generated by the central solenoid. The ID barrel (end-cap) parts consists of 3 ( $2 \times 3$ ) Pixel layers, 4 ( $2 \times 9$ )



layers of double-sided silicon strip modules and 73 ( $2 \times 160$ ) layers of TRT straws. With all the trackers, the inner detector has full coverage in  $\phi$  and covers the region  $|\eta| < 2.5$ , and a sensitive radial distance from the interaction point of 50.5 mm up to 1066 mm.

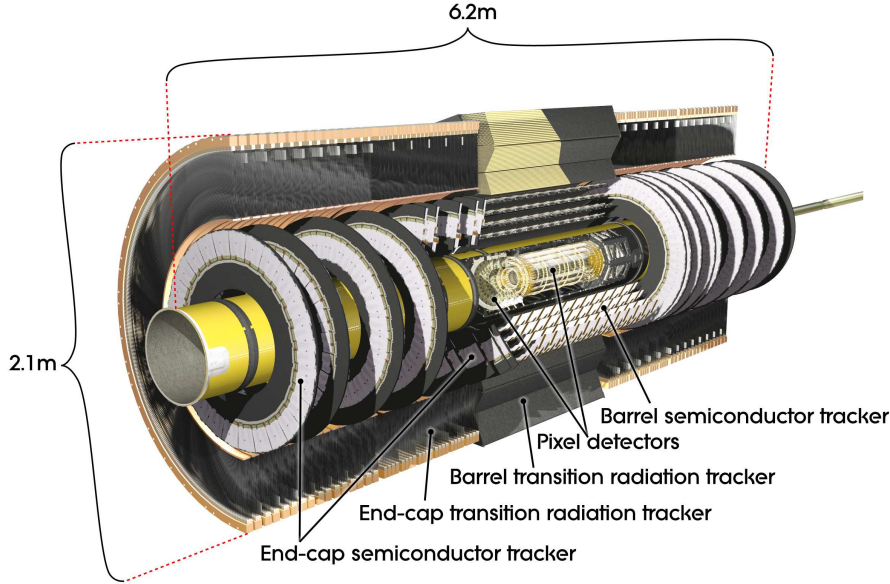


Figure 3.5: Cut-away view of the ATLAS inner detector [45].

## Calorimeters

The ATLAS calorimeters consists of a high resolution electromagnetic calorimeter and a hadronic calorimeter, shown in Fig. 3.6. The calorimeters cover the range  $|\eta| < 4.9$ , using different techniques adapted to the requirements of the physics of interest and of the radiation environment over this  $\eta$  range. The liquid-argon electromagnetic sampling calorimeters (LAr), designed for excellent energy and position resolution, cover the pseudorapidity range  $|\eta| < 3.2$ . Over the  $\eta$  region that is overlapped with the inner detector ( $|\eta| < 2.5$ ), the electromagnetic calorimeter is segmented in three sections in depth. The fine granularity is devoted to precision measurement of electrons and photons. For the end-cap inner wheel ( $|\eta| > 1.5$ ), the LAr technology is applied to complement the hadronic calorimeters where the calorimeter is segmented in three sections in depth with a coarser lateral granularity. The hadronic calorimeter in the range  $|\eta| < 1.7$  is provided by a scintillator-tile calorimeter placed directly outside the LAr calorimeter envelope with one barrel covering the region  $|\eta| < 1.0$  and two extended barrels for  $0.8 < |\eta| < 1.7$ . Both barrel and extended barrels are divided azimuthally into 64 modules. Radially the tile calorimeter extends from an inner radius of 2.28 m to an outer radius of 4.25 m and it is segmented in three layer in depth. The Hadronic End-cap Calorimeter (HEC) consists of two independent wheels in each side, installed directly behind the end-cap electromagnetic calorimeter. The HEC covers the region  $1.5 < |\eta| < 3.2$  overlapping with the forward calorimeter and the tile calorimeter in

order to reduce the drop in material density at the transition regions. The LAr Forward Calorimeter (FCal) provides both electromagnetic and hadronic energy measurements over  $3.1 < |\eta| < 4.9$  and meanwhile reduce radiation background levels for the muon spectrometer. The coarser granularity above  $|\eta| = 2.5$  is sufficient to satisfy the physics requirement for jet reconstruction and  $E_T^{\text{miss}}$  measurement.

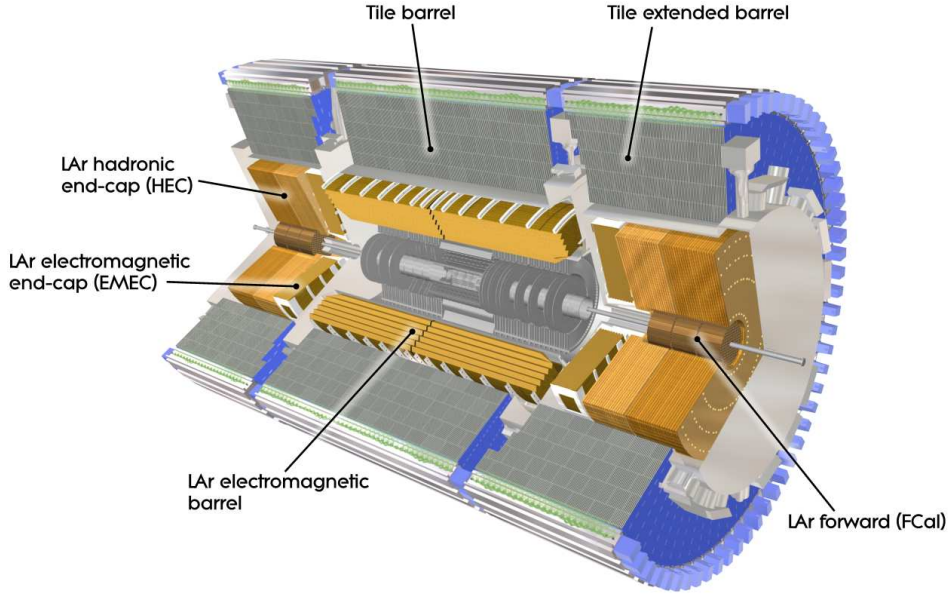


Figure 3.6: Cut-away view of the ATLAS calorimeter system [45].

### Muon spectrometer

The muon spectrometer occupies the outer part of the ATLAS detector covering  $|\eta| < 2.7$  (Fig. 3.7). It is based on the magnetic deflection of muon tracks in the large superconducting air-core toroid magnets, instrumented with separate trigger and high-precision tracking chambers. The barrel toroid provides the magnetic field over  $1.4 < |\eta| < 1.6$  and the two smaller end-cap magnets cover  $1.6 < |\eta| < 2.7$ . In the transition region,  $1.4 < |\eta| < 1.6$ , muons tracks are bent by a combination of barrel and end-cap fields. In the barrel region, tracks are measured in chambers arranged in three cylindrical layers around the beam axis; in the transition and end-cap regions, the chambers are installed in three-layer planes perpendicular to the beam. Over most of the  $\eta$ -range, a precision measurement of the track coordinates in the principal bending direction of the magnetic field is provided by the Monitored Drift Tubes (MDT). At large pseudorapidities, Cathode Strip Chambers (CSC) with higher granularity are used in the innermost plane over  $2 < |\eta| < 2.7$ . The trigger system covers the pseudorapidity range  $|\eta| < 2.4$  with Resistive Plate Chambers (RPC) in the barrel and Thin Gap Chambers (TGC) in the end-cap regions. The trigger system of the muon spectrometer provides bunch-crossing identification and well-defined

$p_T$  thresholds. It measures the muon coordinate in the direction orthogonal to that used by the precision-tracking chambers.

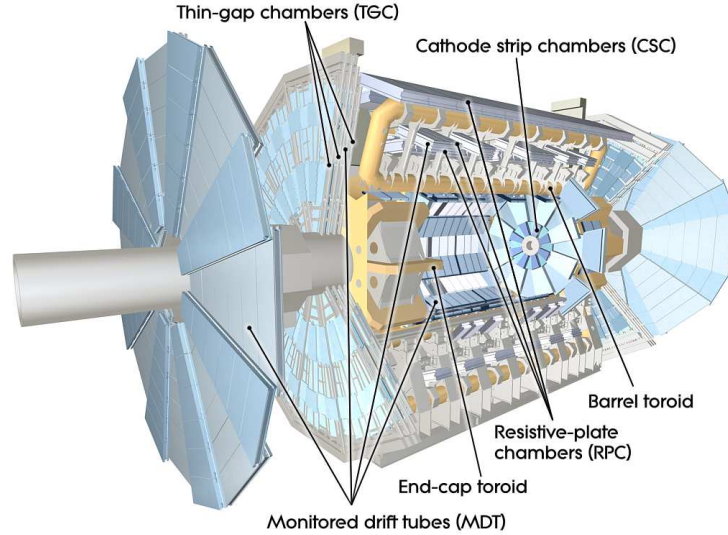


Figure 3.7: Cut-away view of the ATLAS muon system [45].

### Magnet system

The ATLAS magnet system is an arrangement of four superconducting magnets, a central solenoid surrounded by three large air-core toroids (shown in Fig. 3.8). The solenoid is aligned on the beam axis and provides a 2 T axial magnetic field for the inner detector while minimising the material in front of the barrel electromagnetic calorimeter. In the muon spectrometer, the three large air-core toroids generate the magnetic field to deflect muon tracks. The two end-cap toroids are inserted at each end of the barrel toroids and lined up with the central solenoid. Each of the three toroids consists of eight coils assembled radially and symmetrically around the beam axis. The end-cap toroid coil system is rotated by 22.5 degree respecting the barrel toroid coil system in order to optimise the bending power in the transition region where two magnets overlap. The barrel toroid provides a magnetic field of approximately 0.5 T in the range  $|\eta| < 1.4$ , and the end-cap toroids offer about 1 T in the region  $1.6 < |\eta| < 2.7$ .

### Trigger system

The bunch crossing rate of the LHC is expected to be 40 MHz at design luminosity. The trigger system in the ATLAS detector needs to reduce the event rate down to 200 Hz allowing for optimal use of the bandwidth to record signal events. The trigger system has three distinct levels: the hardware based Level 1 trigger (L1), the software based High Level triggers including Level 2 trigger (L2) and the event filter (EF). Each trigger level refines the trigger decisions based on the information passed at the previous level.

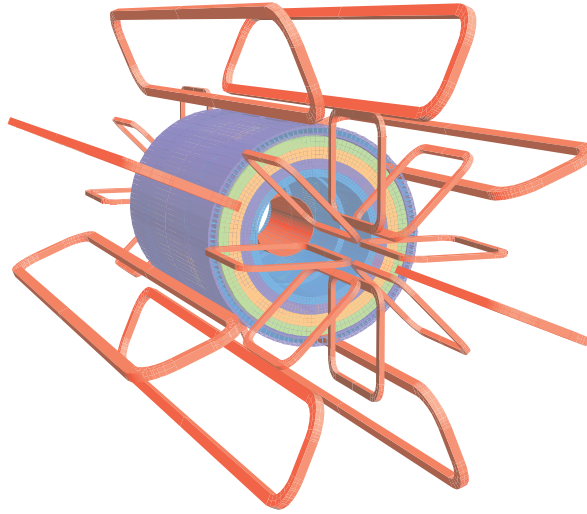


Figure 3.8: Geometry of magnet windings and tile calorimeter steel. The eight barrel toroid coils with the end-cap coils interleaved are visible. The solenoid winding lies inside the calorimeter volume [45].

The infrastructure of the trigger system is demonstrated in Fig. 3.9. At Level 1, the data acquisition system (DAQ) receives and buffers the event data from the detector readout electronics and the L1 trigger uses the detector information to make the decision in less than  $2.5 \mu\text{s}$ , reducing the rate to about 75 kHz. The L1 trigger is able to search for high transverse momentum muons, electrons, photons and  $\tau$  leptons decaying into hadrons, as well as large missing and total transverse energy. In each event, the trigger defines one or several Regions-of-Interest (RoI's) in terms of the geographical coordinates in  $\eta$  and  $\phi$  to identify interesting regions for physics objects. The selection relies on the information from sub-systems: high  $p_T$  muon candidates are identified by the trigger chambers in the muon system; whereas calorimeter selections at L1 are based on the reduced-granularity information from all the calorimeters. Results from the L1 muon and calorimeter triggers are processed by the central trigger processor (CTP) which implements a trigger menu combining trigger selections for physics objects. Events passing the L1 trigger selection are delivered to the next level of the trigger system via detector readout electronics. The L2 selection is seeded by the RoI information from the L1 trigger and additionally uses the information from the full granularity of the detector to refine the decision. The L2 trigger menus are designed to reduce the trigger rate to 3.5 kHz with an average event processing time of about 40 ms. The final event selection is carried out by the event filter which reduces the event rate down to 200 Hz by implementing offline analysis procedures. In addition, the event filter classifies the selected events to a predetermined set of event streams and pass them to the sub-farm output nodes, (SFO's). The average event processing time at EF is restricted to be the order of four seconds. The events received by an SFO are stored in the local file system according to the classification given by the even filter. In the end, the event files are transferred to the central data-recording facility for offline processing.

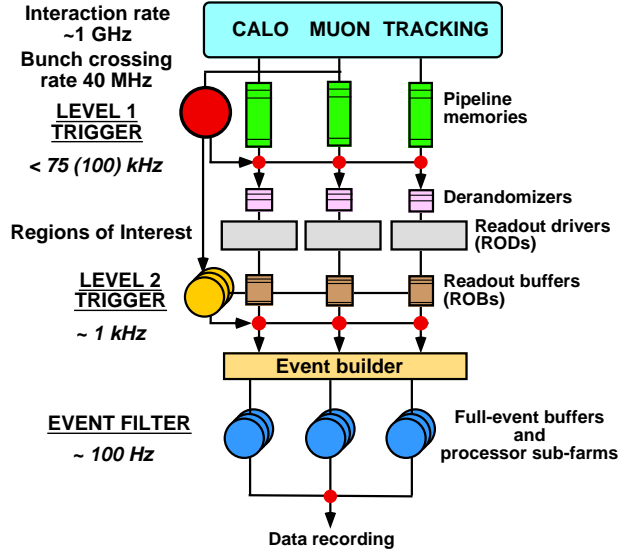


Figure 3.9: Diagram of the ATLAS trigger and DAQ system [46].

### Overall performance

Excellent detector performance is required in order to achieve the physics goals at ATLAS. For instance, exploring the full range of the possible Higgs boson masses requires high-resolution measurements of electrons, photons, and muons, excellent secondary vertex detection for  $\tau$  leptons and  $b$ -quarks, high-resolution calorimetry for jets and missing  $E_T$ . The general performance goals are summarised in Table 3.1 which have been investigated based on full simulations of the ATLAS detector response (described in the next chapter).

Detector component	Required resolution	$\eta$ coverage Measurement	$\eta$ coverage Trigger
Tracking	$\sigma_{p_T}/p_T = 0.05\% p_T \oplus 1\%$	$\pm 2.5$	
EM calorimetry	$\sigma_E/E = 10\%/\sqrt{E} \oplus 0.7\%$	$\pm 3.2$	$\pm 2.5$
Hadronic calorimetry (jets) barrel and end-cap forward	$\sigma_E/E = 50\%/\sqrt{E} \oplus 3\%$ $\sigma_E/E = 100\%/\sqrt{E} \oplus 10\%$	$\pm 3.2$ $3.1 <  \eta  < 4.9$	$\pm 3.2$ $3.1 <  \eta  < 4.9$
Muon spectrometer	$\sigma_{p_T}/p_T = 10\%$ at $p_T = 1$ TeV	$\pm 2.7$	$\pm 2.4$

Table 3.1: General performance goals of the ATLAS detector. The units for  $E$  and  $p_T$  are in GeV. [47]

# Chapter 4

## Expected performance of the ATLAS experiment

The expected performance of the ATLAS detector is examined in Ref. [47] where the experimental sensitivities to a wide variety of measurements and potential observations of new physical processes were investigated. The studies were done using the Monte Carlo samples of physic processes generated with the centre-of-mass energy of 14 TeV, and fully simulated with the ATLAS detector response. As the focus of this thesis is the B hadron measurements and the performance of ATLAS tracking system, this chapter will summarise the relevant performance studies in Ref. [47], i.e. tracking, muon reconstruction and the muon trigger system.

### 4.1 Tracking

At the LHC design luminosity of  $10^{34} \text{ cm}^{-2}\text{s}^{-1}$ , approximately 1000 particles will emerge from the collision point every 25 ns within  $|\eta| < 2.5$ , producing a very large track density in the detector. The inner detector (ID) in the ATLAS experiment is expected to achieve precise momentum and vertex resolution, and electron identification. The tracking and vertex information from the ID is essential for the follow-up measurements in the calorimeters and muon spectrometer, such as the missing  $E_T$  measurement, reconstructions of electrons, photons, and muons.

As mentioned in the previous chapter, the ID consists of three layers of pixel detectors (Pixel), four layers of silicon strip detectors (SCT) and a transition radiation Tracker (TRT) composed of straw proportional tubes. It surrounds the LHC beam-pipe that is inside a radius of 36 mm. A plan view of the inner detector showing the major elements is illustrated in Fig. 4.1 and the basic parameters of the inner detector are summarised in Table. 4.1.

The silicon detectors, pixels and SCT, are designed for precision tracking, covering the region  $|\eta| < 2.5$ . In the barrel region, they are arranged on concentric cylinders around the beam axis and in the end-cap regions both are installed on disks perpendicular to the beam axis. The highest granularity is achieved around the vertex region using silicon pixel

Item		Radial extension (mm)	Length (mm)	
<b>Pixel</b>	Overall envelope	$45.5 < R < 242$	$0 <  z  < 3092$	
	3 cylindrical layers	Sensitive barrel	$50.5 < R < 122.5$	$0 <  z  < 400.5$
	2 × 3 disks	Sensitive end-cap	$88.8 < R < 149.6$	$495 <  z  < 650$
<b>SCT</b>	Overall envelope	$255 < R < 549$ (barrel)	$0 <  z  < 805$	
		$251 < R < 610$ (end-cap)	$810 <  z  < 2797$	
	4 cylindrical layers	Sensitive barrel	$299 < R < 514$	$0 <  z  < 749$
	2 × 9 disks	Sensitive end-cap	$275 < R < 560$	$839 <  z  < 2735$
<b>TRT</b>	Overall envelope	$554 < R < 1082$ (barrel)	$0 <  z  < 780$	
		$617 < R < 1106$ (end-cap)	$827 <  z  < 2744$	
	73 straws planes	Sensitive barrel	$563 < R < 1066$ (barrel)	$0 <  z  < 712$
	160 straws planes	Sensitive end-cap	$644 < R < 1004$ (barrel)	$848 <  z  < 2710$

Table 4.1: Main parameters of the inner detector

sensors segmented in  $R$ - $\phi$  and  $z$  with typically three pixel layers crossed by each track. The first “vertexing layer” (B-Layer) is at a radius of 51 mm. The intrinsic accuracies in the barrel are  $10 \mu\text{m}$  ( $R$ - $\phi$ ) and  $115 \mu\text{m}$  ( $z$ ) and in the disks are  $10 \mu\text{m}$  ( $R$ - $\phi$ ) and  $115 \mu\text{m}$  ( $R$ ). For the SCT, eight strip layers (four space points) are crossed by each track. In the barrel region, the detector uses small-angle (40 mrad) stereo strips with one set of strips in each layer parallel to the beam direction to measure the  $R$ - $\phi$  coordinates. The intrinsic accuracies per module are  $17 \mu\text{m}$  ( $R - \phi$ ) in both the barrel and the disks,  $580 \mu\text{m}$  ( $z$ ) in the barrel and  $580 \mu\text{m}$  ( $R$ ) in the disks.

A large number of hits are provided by the TRT which is using straw drift tubes of 4mm diameter and covers the range to  $|\eta| = 2.0$ . The typical number of TRT hits per track is 30 while the maximum is 36. In the barrel region, the straws are of length 144 cm, in parallel to the beam axis. In the end-cap region, the 37 cm long straws are arranged radially in wheels. The intrinsic accuracy in  $R$ - $\phi$  is  $130 \mu\text{m}$  per straw. The large number of straw hits from the TRT contribute significantly to the momentum measurement at the outer radius of the ID, complemented by the silicon trackers at small radii. The TRT hits at a larger radius enables the inner detector to accomplish very robust pattern recognition and high precision in both the  $R$ - $\phi$  and  $z$  coordinates. With the solenoid field of 2 T, the ID is able to measure charged tracks with transverse momentum  $p_T > 0.5 \text{ GeV}$  and  $|\eta| < 2.5$ , although the efficiency at low momentum is degraded due to material effects. The intrinsic measurement performance expected for each ID sub-system is summarised in Table 4.2.

The inner detector provides tracking measurements in a range matched by the precision measurements of the electromagnetic calorimeter. The electron identification is enhanced by the detection of transition-radiation photons in the TRT straw tubes. Besides, the silicon trackers pursue impact parameter measurements and vertex reconstruction for heavy-flavour and  $\tau$ -lepton tagging, and the secondary vertex measurement is improved by the innermost layer of pixels, at a radius of about 5 cm. The concentration of this section is the expected performance of the inner detector in terms of tracking, vertexing and particle

identification. The impact of the inner detector alignment, as one of the main topics in the thesis, is described separately in Chapter 6.

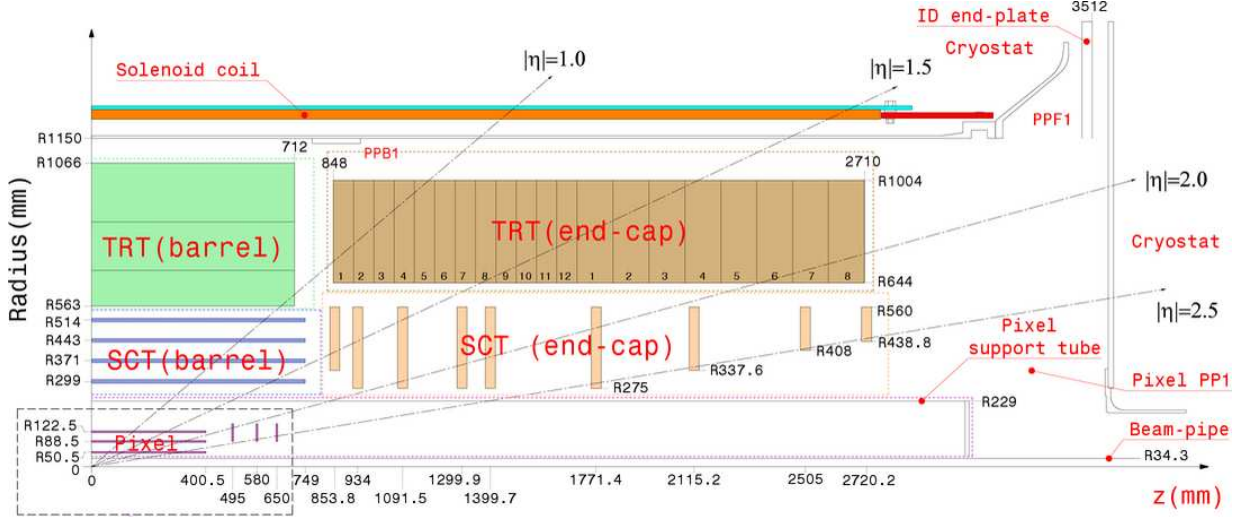


Figure 4.1: The layout of the inner detector and its major elements with active dimensions and coverages.

Item	Intrinsic accuracy ( $\mu\text{m}$ )	Alignment tolerances ( $\mu\text{m}$ )		
		Radial (R)	Axial (z)	Azimuth ( $R-\phi$ )
<b>Pixel</b>				
Layer-0	10 ( $R-\phi$ ) 115 ( $z$ )	10	20	7
Layer-1 and -2	10 ( $R-\phi$ ) 115 ( $z$ )	20	20	7
Disks	10 ( $R-\phi$ ) 115 ( $z$ )	20	100	7
<b>SCT</b>				
Barrel	17 ( $R-\phi$ ) 580 ( $z$ )	100	50	12
Disks	17 ( $R-\phi$ ) 580 ( $z$ )	50	200	12
<b>TRT</b>	130			30

Table 4.2: Intrinsic measurement accuracies and mechanical alignment tolerances for the inner detector sub-systems, as defined by the performance requirements of the ATLAS experiment. The numbers in the table correspond to the single-module accuracy for the pixels, to the effective single-module accuracy for the SCT and to the drift-time accuracy of a single straw for the TRT [47].

### Track reconstruction

The reconstruction of tracks after the inner detector read-out system is carried out by the modular and flexible reconstruction software which allows for standardised interfaces to all reconstruction tools, such as track extrapolation, track fitting, and vertex fitting. The extrapolation algorithms combines propagation tools with an accurate and optimised



description of the active and passive material of the full detector to allow for material corrections during reconstruction. The suite of track-fitting tools includes global- $\chi^2$  and Kalman-filter techniques, and other specialised fitters such as dynamic noise adjustment (DNA) [48], Gaussian-sum filters (GSF) [49] and deterministic annealing filters [50]. The tools which cope with electron bremsstrahlung (DNA and GSF) will be run after the track reconstruction for electron-photon identification. Other common tracking tools are provided for applying calibration corrections at later stages of the pattern recognition, correcting for module deformations or resolving hit-association ambiguities. In general, the offline tracking procedure in the inner detector can be sub-divided into three stages:

**Pre-processing stage** The raw data read out by the pixel and SCT detectors are converted into clusters and the TRT raw timing information is translated into calibrated drift circles. The SCT clusters are transformed into space-points, using a combination of the cluster information from opposite sides of each SCT module.

**Track-finding stage** Different tracking strategies are implemented for seeking tracks. The default tracking exploits the high granularity of the pixel and SCT detectors to find prompt track originating from the interaction region. First, track seeds are formed from a combination of space-points in the three pixel layers and the first SCT layer and then extended throughout the SCT to form track candidates. Next, the track candidates are fitted with further quality cuts. Afterwards, “outlier” clusters which are excluded in the track fit are removed, ambiguities in the cluster-to-track association are resolved, and fake tracks are rejected. The selected tracks are then extended into the TRT to associate drift-circle information in a path around the extrapolation. At last, the extended tracks are compared to the silicon-only track candidates and hits on track extensions causing bad fits are labelled as outliers and excluded in the fit. A complementary track-finding strategy, called back-tracking, searches for unused track segments in the TRT and extends them into the SCT and pixel detectors to improve the tracking efficiency for secondary tracks from conversion or decays of long-lived particles.

**Post-processing stage** A dedicated vertex finder is applied to reconstruct primary vertices at the last stage. Afterwards, other vertexing algorithms are used to reconstruct photon conversions and secondary vertices.

### Tracking performance

The expected performance of the tracking system for reconstructing single particles and particles in jets has been investigated in Ref. [47] where a precision modelling of the individual detector response including noise and inefficiencies, geometry and passive material in the simulation were included. A common set of selections cuts for reconstructed tracks were applied in the Monte Carlo study. Prompt particles which came from the primary vertex were required to have  $p_T > 1$  GeV and  $|\eta| < 2.5$ . Standard quality cuts required tracks to contain at least seven silicon hits (pixels and SCT). In addition, the transverse impact parameter  $d_0$  and the longitudinal one  $z_0$  must fulfil the criteria of  $d_0 < 1$  mm

and  $|z_0 - z_v| \sin \theta < 10$  mm where  $z_v$  is the position of the primary vertex and  $\theta$  is the polar angle of the track. The b-tagging cuts which are for identifying the jets containing  $b$  quarks were defined by: at least two hits in the pixels, one of which should be in the vertex layer, as well as  $|d_0| < 1$  mm and  $|z_0 - z_v| \sin \theta < 1.5$  mm. A reconstructed track was matched to a Monte Carlo particle if at least 80% of the hits were found to be created by that particle. The tracking efficiency was defined as the fraction of particles which are matched to reconstructed tracks passing the quality cuts, and the fake rate was defined as the fraction of reconstructed tracks passing the quality cuts but not matched to a particle.

**Track parameter resolution** The resolution of a track parameter  $X$  is expressed as a function of  $p_T$ :

$$\sigma_X(p_T) = \sigma_X(\infty)(1 \oplus p_X/p_T) \quad (4.1)$$

where  $\sigma_X(\infty)$  is the asymptotic resolution expected at infinite momentum,  $p_X$  represents the value of  $p_T$  for which the intrinsic resolution and the multiple scattering contribution are equal for the parameter  $X$  and  $\oplus$  denotes addition in quadrature. The expression is working well at high  $p_T$  where the resolution is dominated by the intrinsic detector resolution and at low  $p_T$  where the resolution is driven by multiple scattering.  $\sigma_X(\infty)$  and  $p_X$  are implicitly functions of the pseudorapidity. Figure 4.2 shows the momentum resolution for isolated muons without a beam constraint and neglecting effects of misalignment, miscalibration and pile-up. The resolution are taken as the RMS (Root Mean Square) evaluated over a range which includes 99% of the data (corresponding to  $\pm 3\sigma$  for a Gaussian distribution). As the TRT measurements can only cover the region  $|\eta| < 2.0$ , the momentum resolution is degraded beyond  $|\eta| = 2.0$  as is clearly reflected in Fig. 4.2. Due to the different momentum resolution in  $\eta$ , the reconstructed mass resolutions of resonances varies in accordance with the regions where the decay products are found. For instance, Fig.4.3 shows that the mass resolution of  $J/\psi$  from  $J/\psi \rightarrow \mu\mu$  in the end-cap regions is twice as high as in the barrel region.

Table 4.3 shows the values of  $\sigma_X(\infty)$  and  $p_X$  for tracks in the barrel and end-caps. The impact parameter resolutions are quoted only for tracks with a hit in the vertexing layer.

Track parameter	$0.25 <  \eta  < 0.5$		$1.50 <  \eta  < 1.75$	
	$\sigma_X(\infty)$	$p_X(\text{GeV})$	$\sigma_X(\infty)$	$p_X(\text{GeV})$
Inverse transverse momentum ( $q/p_T$ )	$0.34 \text{ TeV}^{-1}$	44	$0.41 \text{ TeV}^{-1}$	80
Azimuthal angle ( $\phi$ )	$70 \mu\text{rad}$	39	$92 \mu\text{rad}$	49
Polar angle ( $\cot \theta$ )	$0.7 \times 10^{-3}$	5.0	$1.2 \times 10^{-3}$	10
Transverse impact parameter ( $d_0$ )	$10 \mu\text{m}$	14	$12 \mu\text{m}$	20
Longitudinal impact parameter ( $z_0 \times \sin \theta$ )	$91 \mu\text{m}$	2.3	$71 \mu\text{m}$	3.7

Table 4.3: Expected track-parameter resolutions (RMS) at infinite transverse momentum,  $\sigma_X(\infty)$ , and transverse momentum,  $p_X$ , at which the multiple scattering contribution equals that from the detector resolution. The momentum and angular resolutions are shown for muons whereas the impact parameter resolutions are for pions.

The determination of the lepton charge at high  $p_T$  is required to be better than  $3\sigma$  in

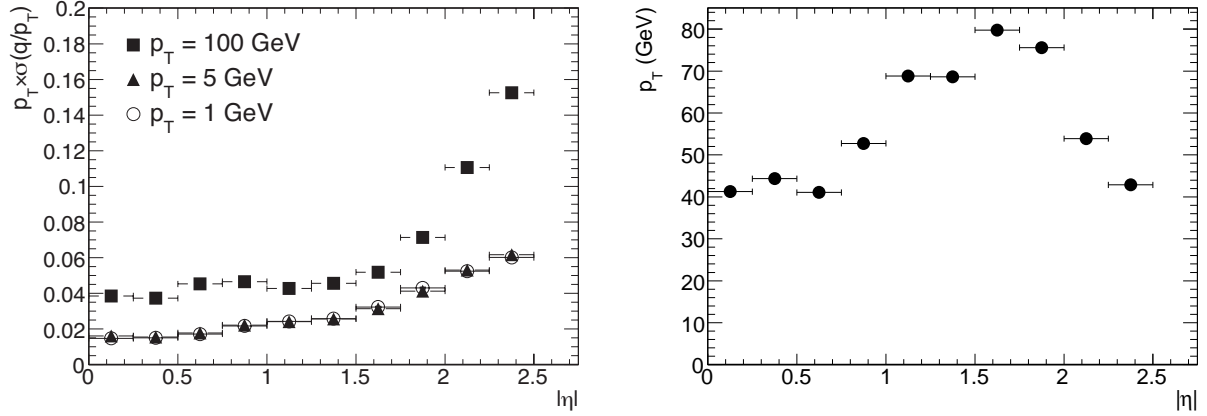


Figure 4.2: Relative transverse momentum resolution (left) as a function of  $|\eta|$  for muons with  $p_T = 1, 5$  and  $100$  GeV. Transverse momentum, at which the multiple-scattering contribution equals the intrinsic resolution (according to Eq. (4.1)), as a function of  $|\eta|$  (right) [47].

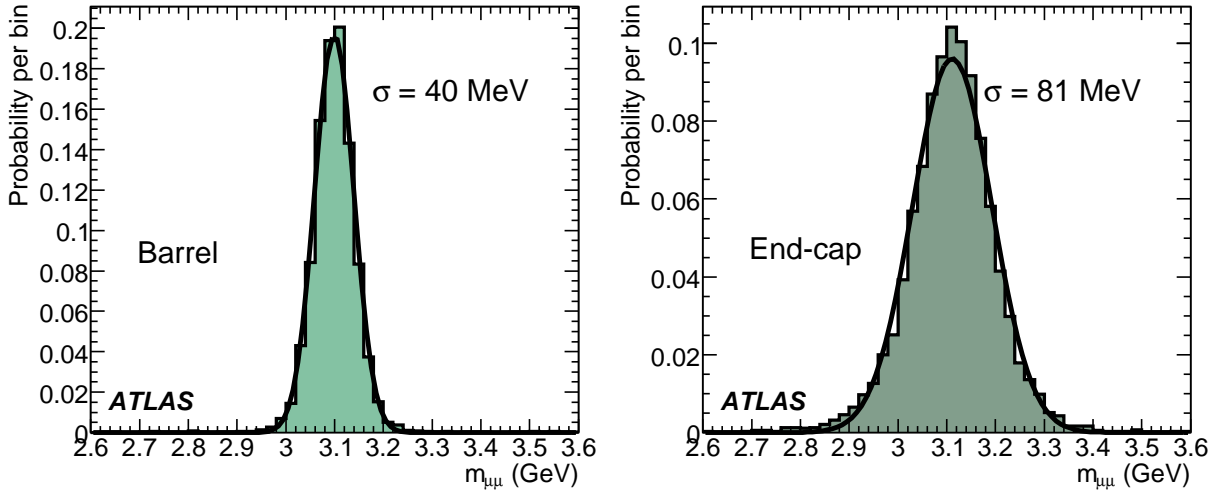


Figure 4.3: Probability for the reconstructed invariant mass of muon pairs from  $J/\psi \rightarrow \mu\mu$  for both muons with  $|\eta| < 0.8$  (left) and  $|\eta| > 1.5$  (right) [47].

order to get a good measurement of charge asymmetries, such as arising from the decays of heavy gauge bosons ( $W'$  and  $Z'$ ). The muon charge determination relies on the muon system at high momentum, and the inner detector tracking play a leading role for measuring the charge of electrons. For electrons, not only the intrinsic resolution should be taken into account, there are also complicated effects from bremsstrahlung which lowers the track momentum and the conversion of bremsstrahlung photons causing problems for pattern-recognition and degraded charge determination. At high momentum (e.g. 2 TeV), the resolution of  $q/p_T$  for muons is determined by the intrinsic resolution of the detector whereas for electrons the charge misidentification can be partially compensated for by the bremsstrahlung. At low energy (e.g. 0.5 TeV), the effects of conversion are significant for electrons. The fractions of muons and electrons for which the sign of the charge is misidentified is shown in Fig. 4.4. All the studies have been done under the assumption of perfect alignment, as any misalignment will degrade the charge sign determination.

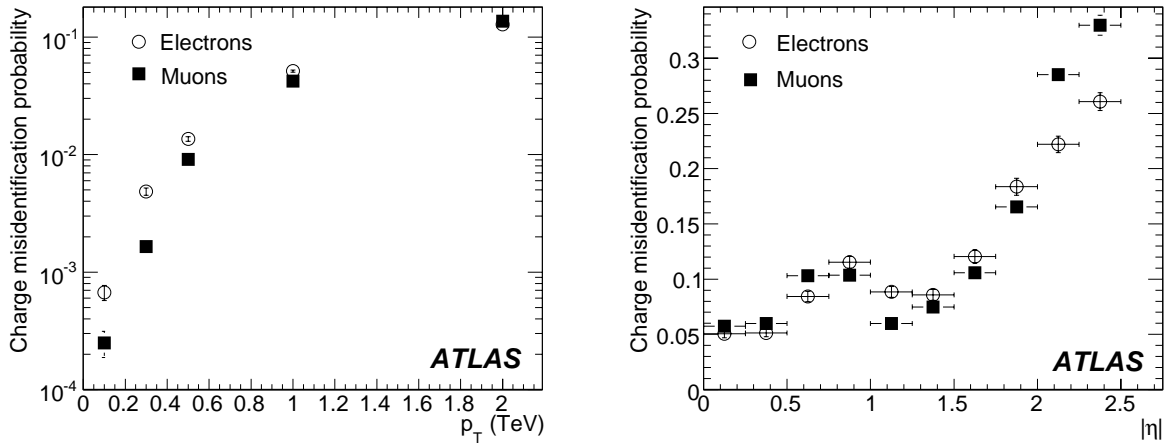


Figure 4.4: Charge misidentification probability for high-energy muons and electrons as a function of  $p_T$  for particles with  $|\eta| \leq 2.5$  (left) and as a function of  $|\eta|$  for  $p_T = 2$  (right). [47]

**Track reconstruction efficiency** Track reconstruction efficiency for isolated muons, pions and electrons are shown in Figs. 4.5 and 4.6. Pions are affected by hadronic interactions in the ID material as well as multiple scattering. The reconstruction inefficiencies of electrons arise from the effects of bremsstrahlung. As a result, the efficiency curve as a function of  $\eta$  for pions and electrons reflect the shape of the amount of material in the inner detector. The efficiency goes up and becomes more uniform in  $|\eta|$  at high energies.

The general tracking strategy described above is aimed at tracking with  $p_T > 0.5$  GeV. For low- $p_T$  tracks below 0.5 GeV, particularly in the minimum bias events, reconstruction is difficult because of the high curvature of the tracks, increased multiple scattering, reduced number of the hits, etc. To enhance the reconstruction efficiency in this region, an additional strategy is introduced to the unused pixel and SCT hits. To further aid the reconstruction, the algorithm for the space-point track seeding is modified to use looser

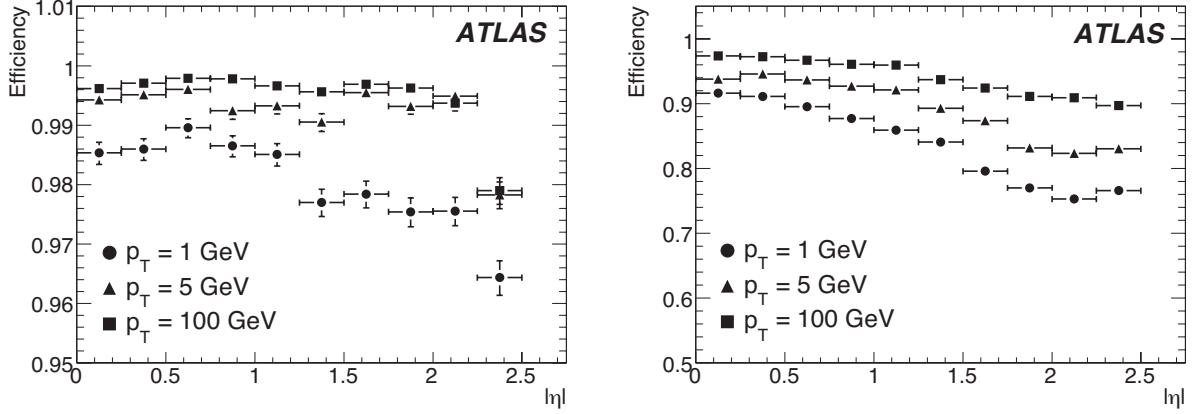
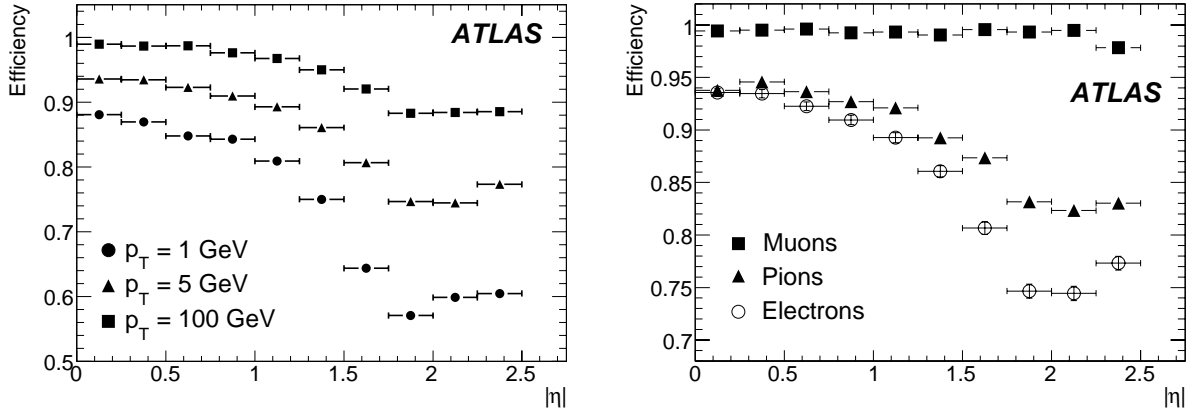


Figure 4.5: Track reconstruction efficiencies as a function of  $|\eta|$  for muons (left) and pions (right) with  $p_T = 1, 5$  and  $100$  GeV. [47]



(a) Track reconstruction efficiencies as a function of  $|\eta|$  for electrons with  $p_T = 1, 5$  and  $100$  GeV. [47]

(b) Track reconstruction efficiencies as a function of  $|\eta|$  for muons, pions and electrons with  $p_T = 5$  GeV. The inefficiencies for pions and electrons reflect the material effects in the inner detector. [47]

Figure 4.6: Track reconstruction efficiencies as a function of  $|\eta|$ .

internal cuts and the cut on the number of precision hits is reduced to at least five hits. Tracks are accepted with  $p_T > 0.1$  GeV, and in some cases, inefficiencies for  $p_T > 0.5$  GeV are recovered. The resulting track reconstruction efficiency is shown in Fig. 4.7. The distribution of fake tracks after low- $p_T$  tracking is shown in Fig. 4.8.

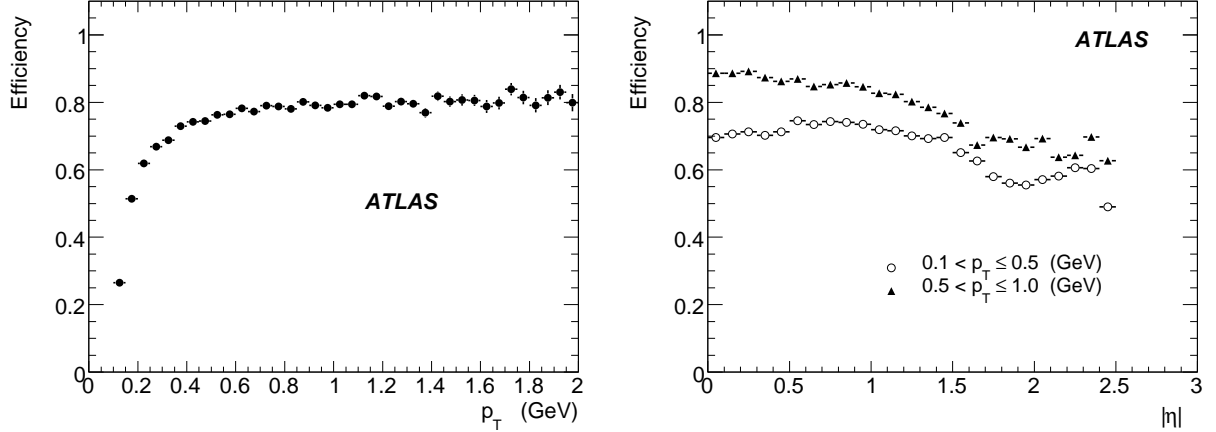


Figure 4.7: Track reconstruction efficiencies as a function of  $p_T$  for  $|\eta| < 2.5$  (left) and as a function of  $|\eta|$  for two different  $p_T$  ranges (right) in minimum bias events (non-diffractive inelastic events). [47]

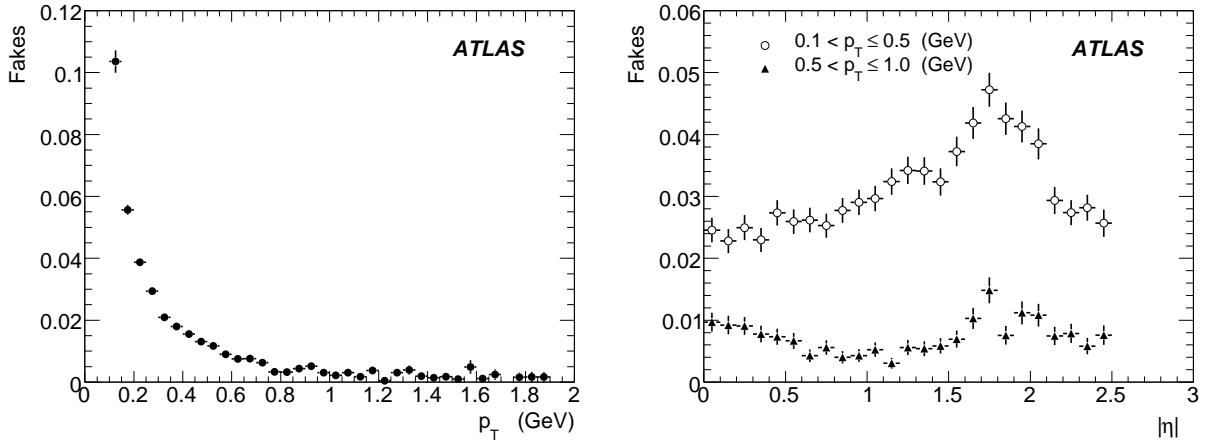


Figure 4.8: Fake rates as a function of  $p_T$  for  $|\eta| < 2.5$  and  $p_T > 0.1$  GeV (left) and as a function of  $|\eta|$  for two different  $p_T$  ranges (right) in minimum bias events (non-diffractive inelastic events). [47]

### Primary vertex reconstruction

Vertexing tools implement the higher-level tracking algorithms to find the primary vertex. To study the resolution of the primary vertex,  $t\bar{t}$  events and  $H \rightarrow \gamma\gamma$  events were used

where  $m_H$  was simulated to be 120 GeV. The primary vertex in  $H \rightarrow \gamma\gamma$  was based on tracks reconstructed from the underlying event and did not include the measurement of photon in the electromagnetic calorimeter. Fig. 4.9 shows the residuals of the primary vertex reconstruction without any beam constraint in  $x$  and  $z$  axes. The primary vertex in  $t\bar{t}$  events has a large track multiplicity and involves a great deal of high- $p_T$  tracks, resulting in a narrower and more Gaussian distribution than in  $H \rightarrow \gamma\gamma$  events. Table 4.4 shows the resolutions of the primary vertex reconstruction in these  $t\bar{t}$  and  $H \rightarrow \gamma\gamma$  events with and without a beam constraint in the transverse plane and the efficiencies to reconstruct and select correctly these primary vertices in the presence of pile-up at a luminosity of  $10^{33} \text{ cm}^{-2}\text{s}^{-1}$ .

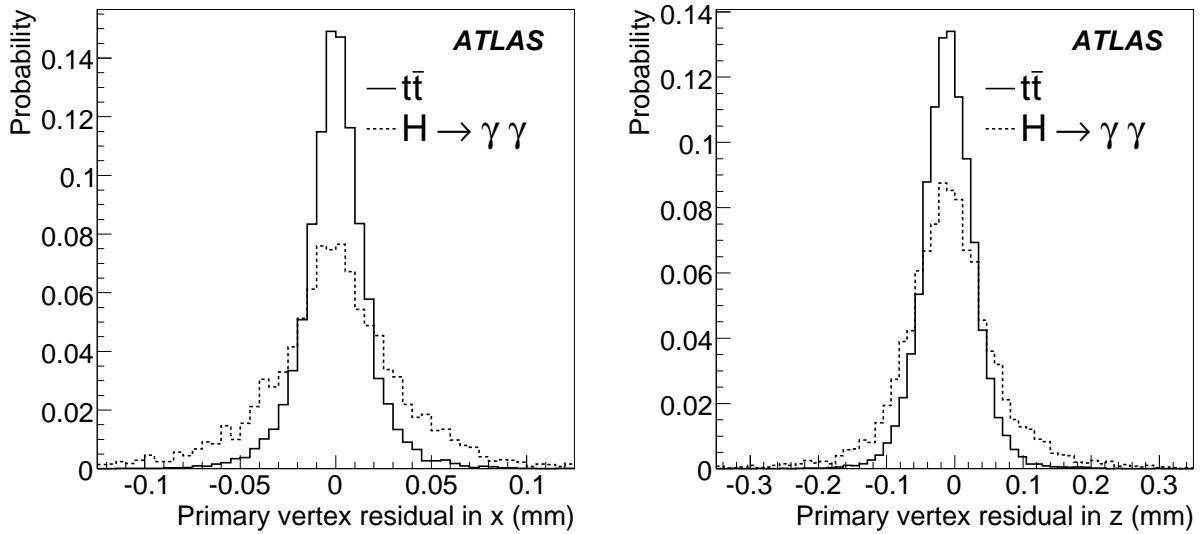


Figure 4.9: Primary vertex residual along  $x$ , in the transverse plane (left), and along  $z$ , parallel to the beam (right), for events containing top-quark pairs and  $H \rightarrow \gamma\gamma$  decays with  $m_H = 120$  GeV. Pile-up and beam constraint are not considered here. [47]

### Electron reconstruction and identification

The material of the inner detector leads to a significant amount of bremsstrahlung for electrons, consequently biases the fitted parameters. Studies show that electrons can lose on average between 20 and 50% of the energy when they leave the SCT. To improve the reconstructed track parameter, the offline electron reconstruction recovers the energy loss using the so-called bremsstrahlung recovery procedures, DNA and GSF. These algorithms are implemented to improve electron reconstruction and not to degrade pions or muons. Since the procedures rely on the inner detector information, they provide improvement only for electron energies below  $\sim 25$  GeV. Fig. 4.10 shows the improvements from the bremsstrahlung recovery for the reconstructed  $J/\psi \rightarrow ee$  mass. Integrating over the full pseudorapidity region of the ID, and without the recovery, only 42% of events are reconstructed within  $\pm 500$  MeV of the  $J/\psi$  nominal mass whereas after the recovery the

Event Type	x-y resolution ( $\mu\text{m}$ )	z resolution ( $\mu\text{m}$ )	Reconstruction eff. (%)	Selection eff. (%)
$t\bar{t}$ (no BC)	18	41	100	99
$t\bar{t}$ (BC)	11	40	100	99
$H \rightarrow \gamma\gamma$ (no BC)	36	72	96	79
$H \rightarrow \gamma\gamma$ (BC)	14	66	96	79

Table 4.4: Primary vertex resolutions (RMS), without and with a beam constraint (BC) in the transverse plane, for  $t\bar{t}$  events and  $H \rightarrow \gamma\gamma$  events with  $m_H = 120$  GeV in the absence of pile-up at a luminosity of  $10^{33}$   $\text{cm}^{-2}\text{s}^{-1}$ . The efficiencies shown here are the efficiencies to reconstruct and then select hard scattering vertex within  $\pm 300$   $\mu\text{m}$  of the true vertex position in  $z$ . The hard scattering vertex is selected as the primary vertex with the largest  $\Sigma p_T^2$ , summed over all its constituent tracks.

acceptance increases to 53% for DNA and 56% for GSF. With the standalone ID tracking, the  $J/\psi$  signal in the end-caps is hardly observed because of the increased material. The reduction in the end-caps arises from the energy lost by electrons when they traverse the pixels (O(30%)) as well as from the change in track directions. With the information from

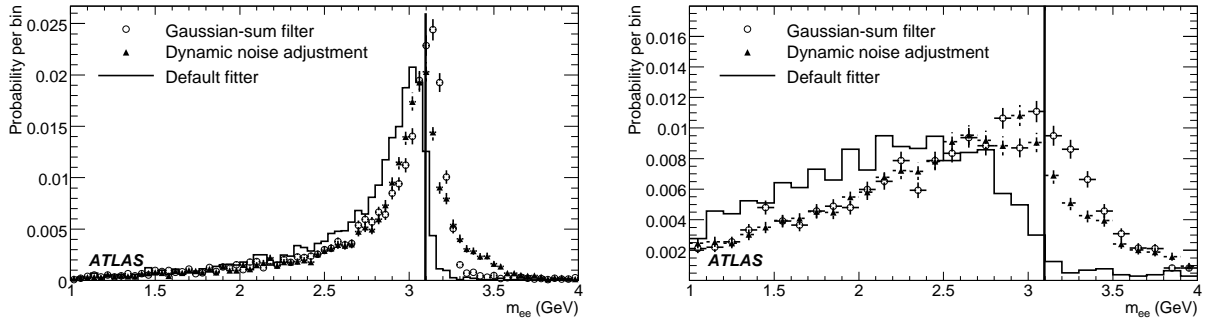


Figure 4.10: Probabilities for the reconstructed invariant mass of electron pairs from  $J/\psi \rightarrow ee$  decays in events with  $B_d^0 \rightarrow J/\psi(ee)K_s^0$  for both electrons with  $|\eta| < 0.8$  (left) and  $|\eta| > 1.5$  (right). The results are shown for the default Kalman fitter and two bremsstrahlung recovery algorithms. The true  $J/\psi$  mass is shown by the vertical lines. [47]

transition radiations, the TRT plays a central role in electron identification, cross-check and complementing the electromagnetic calorimeters typically at energies below 25 GeV.

### Photon conversion

The probability of photon conversion is independent of the energy for  $p_T > 1$  GeV. Study [47] shows 10-50 % of photons have converted into an electron-positron pair before leaving the SCT. Figure 4.11 shows the efficiency for reconstructing conversions of photons with  $p_T = 20$  GeV and  $|\eta| < 2.1$  as a function of the conversion radius and  $|\eta|$ . Tracks are reconstructed using the standard tracking algorithm combined with the back-tracking algorithm. As shown in the figure, at radii above 50 cm the efficiencies for photon



conversion falls because of the single track efficiency. The vertexing tools can be used to reconstruct the photon conversion from track pairs with high efficiency up to radii of 50 cm. However, the overall conversion efficiency can be greatly increased at large radii by flagging single TRT tracks as photon conversion using the capability of TRT to identify electrons and to reject pions.

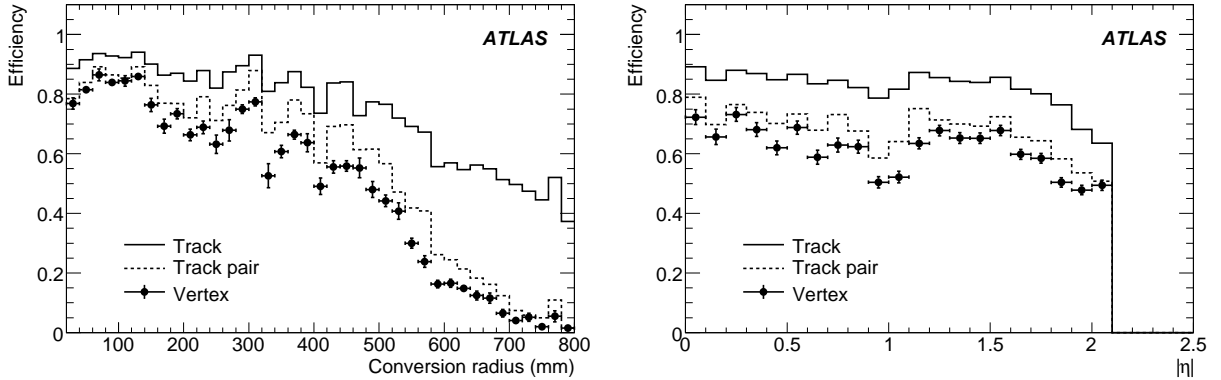


Figure 4.11: Efficiency to reconstruct conversions of photons with  $p_T = 20$  GeV and  $|\eta| < 2.1$ , as a function of the conversion radius (left) and pseudorapidity (right). Comparisons are made among the efficiencies to reconstruct single tracks from conversions, the track pair from the conversion, and the conversion vertex [47].

## Summary

The inner detector tracking and vertexing algorithms have been developed to perform optimal reconstructions of the large amount of charged particles from the collisions at the LHC. For high- $p_T$  muons in the barrel region, the resolution for  $1/p_T$  is expected to be  $0.34 \text{ TeV}^{-1}$  and the resolution for  $d_0$  is expected to be  $10 \mu\text{m}$ . Muons with  $p_T > 1$  GeV can be identified with efficiencies over 98%, and for high- $p_T$  muons the efficiency can exceed 99.5% across the full tracking coverage. In the inner detector, electrons can be identified by the transition radiation emitted in the TRT but suffer from bremsstrahlung. A reasonable reconstruction can be achieved in the barrel region but not the end-caps because of the increased amount of bremsstrahlung. For electrons and pions with momenta around 5 GeV, the reconstruction efficiencies are both between 70% and 95%. The inner detector is able to reconstruct pions down to 0.2 GeV with efficiencies around 50%. Tests of the vertexing algorithm show that primary vertices in  $t\bar{t}$  events can be identified with 99% efficiency in the presence of low-luminosity pile-up. Photon conversions can be identified by reconstructing pairs of tracks or tagging single electrons in the TRT with 80% efficiency all the way up to a radius of 800 mm.

## 4.2 Muon reconstruction and triggers

Among the physics targets for ATLAS, muons (especially high- $p_T$  muons) are involved in many signal channels. Efficient muon reconstruction is crucial for the searches. The ATLAS detector has been designed to perform precise measurements of muons up to 1 TeV. The primary detector system built to achieve this is the muon spectrometer, shown in Fig. 4.12. It covers the pseudorapidity range  $|\eta| < 2.7$  and allows identification of muons with momenta above 3 GeV. The muon spectrometer comprises three systems, a superconducting toroid magnet, precision detectors (MDT and CSC) and trigger systems (RPC and TGC). The MDT and CSC, for precision measurements, are located in three widely-separated stations at increasing distance from the collision region. Each station includes multiple closely-packed layers with a precision better than  $100 \mu\text{m}$  in each layer, measuring the  $\eta$ -coordinate in which most of the magnetic field deflection occurs. The CSC is installed at the high- $|\eta|$  region ( $|\eta| > 2.0$ ) in the inner-most station additionally providing a rough measurement of the  $\phi$ -coordinate and MDT provides measurements in the rest area of the muon system. The RPC and TGC are located in the barrel and end-cap regions separately for rough measurements of both  $\eta$  and  $\phi$  directions.

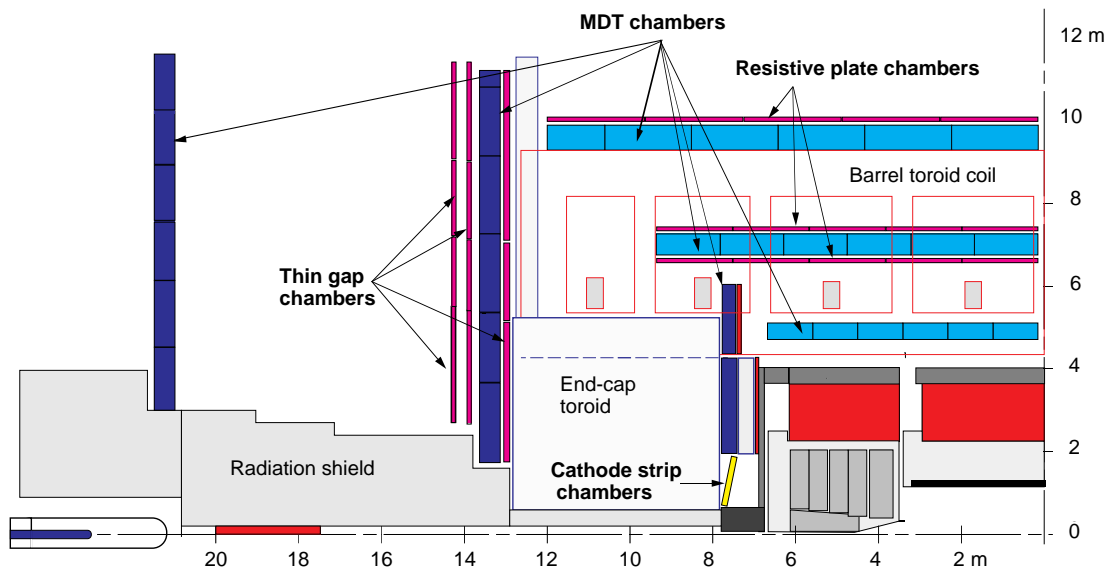


Figure 4.12: The ATLAS muon spectrometer.

High  $p_T$  muons typically transverse all three stations. However, there are  $\eta - \phi$  regions reserved for services where the stations do not provide good measurements, also some regions overlap, causing two measurements from a single station. Resolution and efficiency in these regions are degraded correspondingly. Contributions to the muon spectrometer momentum resolution vary with respect to  $p_T$  as shown in Fig. 4.13. At low momentum, the resolution is dominated by fluctuations in the energy loss of the muons traversing the material before reaching the spectrometer. Multiple scattering in the spectrometer becomes important in the intermediate momentum range. For  $p_T > 300$  GeV, the single-hit resolution that is limited by detector properties, and alignment and calibration dominate

the resolution.

Measurements done in the other systems provide complementary information for muon identification and reconstruction. The calorimeter with a thickness of more than 10 interaction lengths, absorbs hadrons, electrons and photons and provide a direct measurement of the energy loss for the muons that pass by. The inner detector inside the calorimeter overlaps with the muon spectrometer for  $|\eta| < 2.5$  and provide important confirmation of muons found by the spectrometer. For  $p_T$  roughly in the range between 30 and 200 GeV, the momentum measured by the inner detector and muon spectrometer could be combined to give better precision.

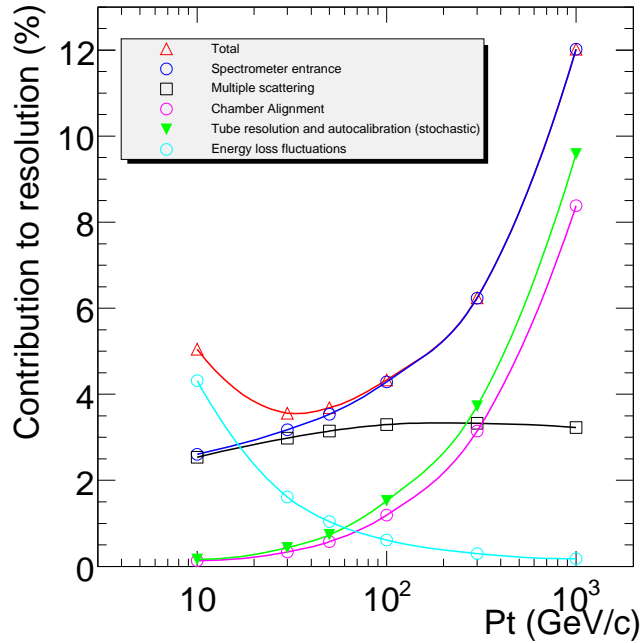


Figure 4.13: Contributions to the momentum resolution for muons reconstructed in the Muon Spectrometer as a function of  $p_T$  for  $|\eta| < 1.5$ .

### 4.2.1 Muon reconstruction

ATLAS employs multiple strategies for identifying and reconstructing muons. Based on the algorithm, there are three types of muons reconstructed for physics analysis.

- *Standalone* muons are reconstructed by first finding tracks in the muon spectrometer and then extrapolating them to the beamline.
- *Combined* muons are found by matching standalone muons to nearby inner detector tracks and then combining the measurements from the two systems.
- *Tagged* muons are sought by extrapolating inner detector tracks to the spectrometer detectors and searching for nearby hits.

The current baseline reconstruction includes two algorithms for each of the above categories. The algorithms are grouped into families so that the output data contains two collections of muons labelled by the name of the combined algorithms: Staco [51] and Muid [52]. Both collections gives similar performance and are used for physics analysis. Comparisons of the performance of these two muon collections are underway. Table 4.5 summarises the three categories of reconstructed muons in ATLAS and the two muon collections with the corresponding algorithms.

	Categories of reconstructed muons		
	Standalone muons	Combined muons	Tagged muons
<b>Staco</b> collection	Muonboy	Staco	MuTag
<b>Muid</b> collection	Moore	Muid	MuGirl

Table 4.5: Two collections of muons from the standard ATLAS reconstruction, and their algorithm applied in each muon category.

### Standalone muons

The standalone algorithms first build track segments in each of the three muon stations and then link them to form tracks. The algorithm from the Staco family is called Muonboy which finds the spectrometer tracks and extrapolate them to the beamline. The Muid family uses the Moore algorithm to find the tracks and performs the inward extrapolation at the first stage. The extrapolation must account for the multiple scattering and energy loss in the calorimeter, for which Muonboy assigns energy loss based on the material crossed in the calorimeter while Moore additionally uses the calorimeter energy measurements if they are significant and the muons appears to be isolated.

The Standalone muons have the advantage of larger  $|\eta|$  coverage (up to 2.7) than the inner detector tracks ( $< 2.5$ ) but there are holes at  $|\eta|$  near 0.0 and 1.2 reserved for services. Low momentum muons ( $\sim$  a few GeV) that do not penetrate to the outermost stations are difficult to reconstruct here. Muons produced in the calorimeter, e.g. from  $\pi$  and  $K$  decays, are likely to be found in the standalone reconstruction as a background for physics analysis, i.e. “fake” muons. Some of such late muons can also be the signal of interest for a few exotic channels.

### Combined muons

The primary track reconstruction algorithm are used for finding the inner detector tracks from muons. Space points are identified in the pixel and SCT which are linked to form track seeds in the inner four layer. Tracks are found by extending the seeds to add measurements from the outer layers. The algorithm is expected to give high detection efficiency over the full ID acceptance,  $|\eta| < 2.5$ .

Both Staco and Muid algorithms match muon spectrometer tracks with inner detector tracks to form combined muons. Pairs are retained according to the quality of the match,

$\chi_{match}$ , defined as the difference between outer and inner track vectors weighted by their combined covariance matrix:

$$\chi_{match}^2 = (\mathbf{T}_{MS} - \mathbf{T}_{ID})^T (\mathbf{C}_{ID} + \mathbf{C}_{MS})^{-1} (\mathbf{T}_{MS} - \mathbf{T}_{ID}) . \quad (4.2)$$

Here  $\mathbf{T}$  denotes a vector of track parameters, expressed at the point of closest approach to the beamline and  $\mathbf{C}$  is its covariant matrix. The Staco algorithm applies a statistical combination of the inner and outer track vectors to obtain the combined track vector:

$$\mathbf{T} = (\mathbf{C}_{ID}^{-1} + \mathbf{C}_{MS}^{-1})(\mathbf{C}_{ID}^{-1}\mathbf{T}_{ID} + \mathbf{C}_{MS}^{-1}\mathbf{T}_{MS}) \quad (4.3)$$

On the Muid side, a partial refit is taken, starting from the inner track vector and covariance matrix and adding the measurements from the outer track. The fit accounts for the material and magnetic field in the calorimeter and the muon spectrometer.

### Tagged muons

The spectrometer tagging algorithms, MuTag and MuGirl, propagate all inner detector tracks with sufficient momentum out to the first station of the muon spectrometer and search for nearby segments. MuTag is part of the Staco family while MuGirl belongs to the Muid family. MuTag defines a tag chi-square using the difference between any nearby segment and its prediction from the extrapolated track. MuGirl uses an artificial neural network to define a discriminant. In either case, if a segment is close enough to the predicted track position, then the inner detector track is tagged to be associated to a muon. MuGirl considers all inner detector tracks and redoes segment finding in the region around the track. Differently, MuTag only make uses of inner detector tracks and muon spectrometer segments that are not used by Staco. Therefore, MuTag serves only to supplement Staco while MuGirl attempts to find all muons.

In addition, the muon finding efficiency could be increased by including muons found by multiple algorithms and removing the overlaps, i.e. cases where the same muon is identified by two or more algorithms. When the muon collections are created, standalone muons that are successfully combined are not recorded separately. If a standalone muon is combined with more than one inner detector track, the case of “best match” is flagged. In the Staco collection, the tagged and combined muons do not overlap. In the Muid collection, overlaps between MuGirl and Muid muons are removed by creating a single muon when both have the same inner detector track.

### Performance

The performance of the muon reconstruction has been investigated for each muon category. Comparisons between Staco and Muid muon collections were made in terms of efficiency, fake rate, and resolutions using Monte Carlo  $t\bar{t}$  events with direct muons, and low- $p_T$  sample of direct  $J/\psi \rightarrow \mu\mu$ , produced for the  $\sqrt{s} = 14$  TeV scenario at the luminosity of  $10^{33} \text{ cm}^{-2}\text{s}^{-1}$ . In addition, the direct  $t\bar{t}$  sample was also overlaid with the cavern background twice as high as what was expected for  $10^{33} \text{ cm}^{-2}\text{s}^{-1}$ , referred to as high-luminosity

$t\bar{t}$  samples below. The *finding efficiency* is defined as the fraction of the true muons that are found and the *good efficiency* is the fraction of true muons that are found and classified as good if the evaluation distance

$$D_{eva} = \sqrt{(\mathbf{T}_{reco} - \mathbf{T}_{true})\mathbf{C}_{reco}^{-1}(\mathbf{T}_{reco} - \mathbf{T}_{true})} < 4.5 \quad (4.4)$$

which is equivalent to a chi-square probability above 0.0011. The *good fraction* is the fraction of found muons that are classified as good. The *fake rate* is defined to be the mean number of fake muons per event. The measurement of the transverse momentum of muons were examined in terms of the fractional momentum resolution:

$$\frac{\Delta p_T}{p_T} = \frac{1/p_{T_{reco}} - 1/p_{T_{true}}}{1/p_{T_{true}}} = \frac{p_{T_{true}} - p_{T_{reco}}}{p_{T_{reco}}}. \quad (4.5)$$

The distribution was fitted with a Gaussian and the resolution is defined to be the sigma of the fit.

**Standalone muon performance** The standalone muon efficiencies and fake rates in  $t\bar{t}$  direct muon samples are shown in Fig. 4.14 for low luminosity (no pile-up or cavern background) and the reference luminosity ( $10^{33} \text{ cm}^{-2}\text{s}^{-1}$  with cavern background safety factor 2.0). The efficiency was lost where the detector coverage was poor, i.e.  $|\eta| = 0.0$  and 1.2. In the other regions, the muon efficiency was close to 100% for Muonboy (Staco collection) and about 99% for Moore/Muid. The good fraction for Muid muons was slightly higher because of better handling of the material in the calorimeter. These two algorithms had similar fake rates at low luminosity whereas at the higher luminosity Moore/Muid rate increased much faster.

In addition, Ref. [47] also shows for the low- $p_T$  non-isolated muons from  $J/\psi$  decays, the Moore/Muid efficiency degraded significantly while Muonboy remained high. The average  $p_T$  resolution was similar for both algorithm, only degraded at intermediate  $|\eta|$  region ( $1.2 < |\eta| < 1.7$ ) because of the reduced number of measurements, the low field integral in the overlap between barrel and end-cap toroids, and the material in the end cap toroid.

**Inner detector performance for tracking muons** The efficiency of tracking muons in the inner detector was high for all  $\eta$  within the acceptance in all the samples. No evidence was seen for degradation when adding pile-up. Figure 4.15 shows the efficiency for  $t\bar{t}$  direct muons and Table 4.6 gives the integrated efficiencies for all the samples. The inner detector momentum resolution for muons is depicted in Fig. 4.16 which is the same as that for tagged muons (described later). The standalone and inner detector measurements are expected to complement one another to give high precision over the full  $\eta$  and  $p_T$  range.

**Combined muon performance** When matching inner detector and muon spectrometer tracks, both Staco and Muid calculate  $\chi_{match}^2$  as a discriminant for separating real and fake muons. The  $t\bar{t}$  direct muon efficiencies and fake rates in the combined muon class are shown in Fig. 4.17. Compared with the standalone muons (Fig. 4.14), Staco family

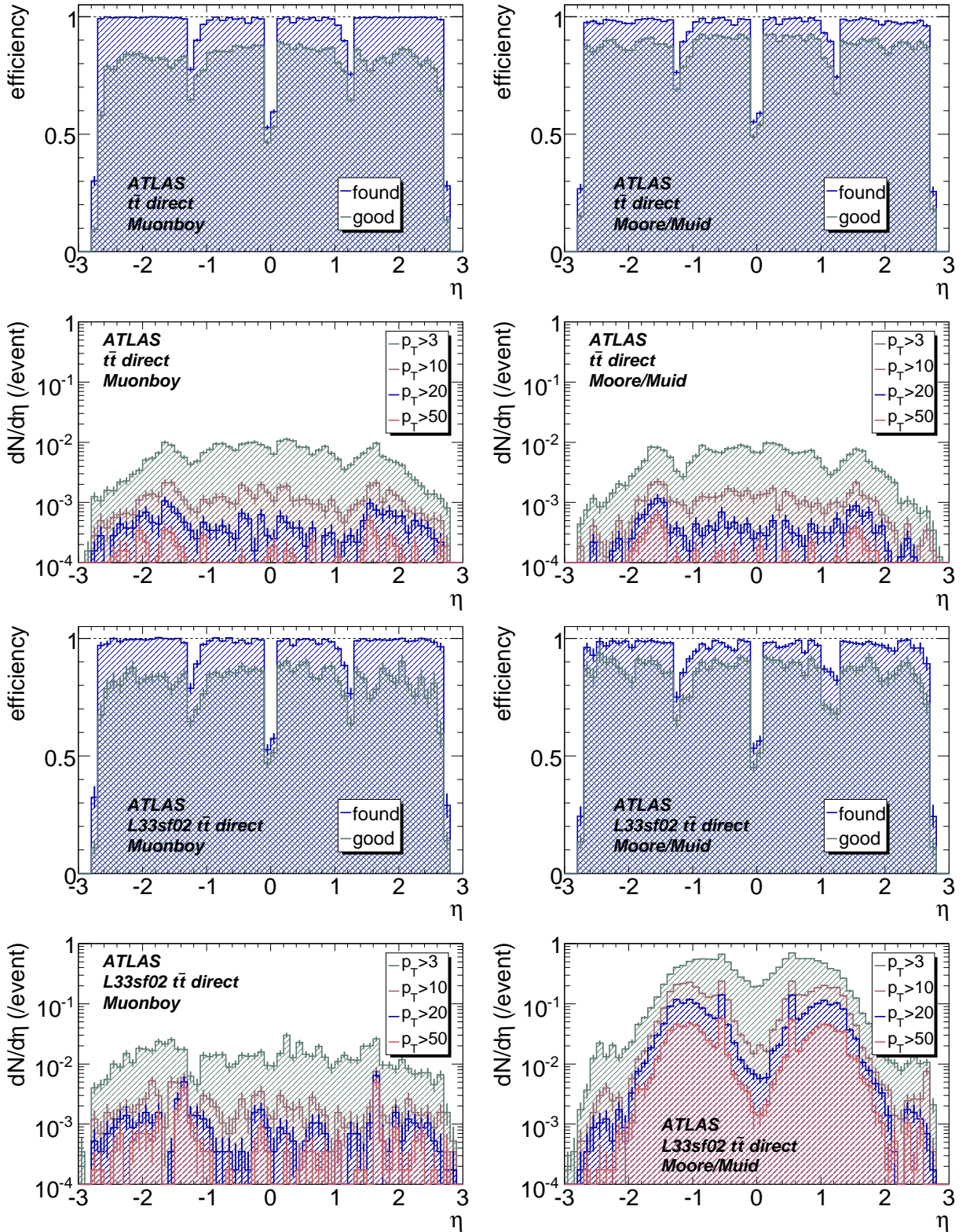


Figure 4.14: Standalone efficiency and fake rate as functions of true  $\eta$  for Muonboy (left) and Moore/Muid (right) for direct muons in  $t\bar{t}$  at low (top) and high (bottom) luminosity [47].

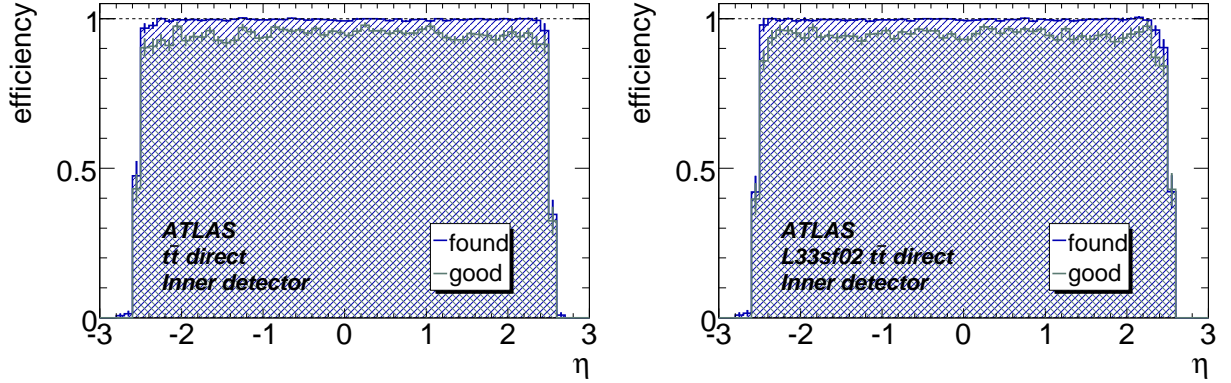


Figure 4.15: Inner detector  $t\bar{t}$  direct muon efficiency as a function of true  $\eta$  at low (left) and high (right) luminosity for  $p_T > 10$  GeV. In each figure, the upper curve is the efficiency to find the muon while the lower curve additionally requires a good match,  $D_{eva} < 4.5$  [47].

Sample	Efficiency	
	found	good
$t\bar{t}$ direct	0.996	0.950
high- $\mathcal{L}$ $t\bar{t}$ direct	0.995	0.947
$J/\psi$	0.995	0.941

Table 4.6: Inner detector efficiencies in the Monte Carlo samples where true muons are required to have  $|\eta| < 2.5$  and  $p_T > 10$  GeV. Efficiencies are presented both for all found muons and muons classified as good ( $D_{eva} < 4.5$ ) [47].

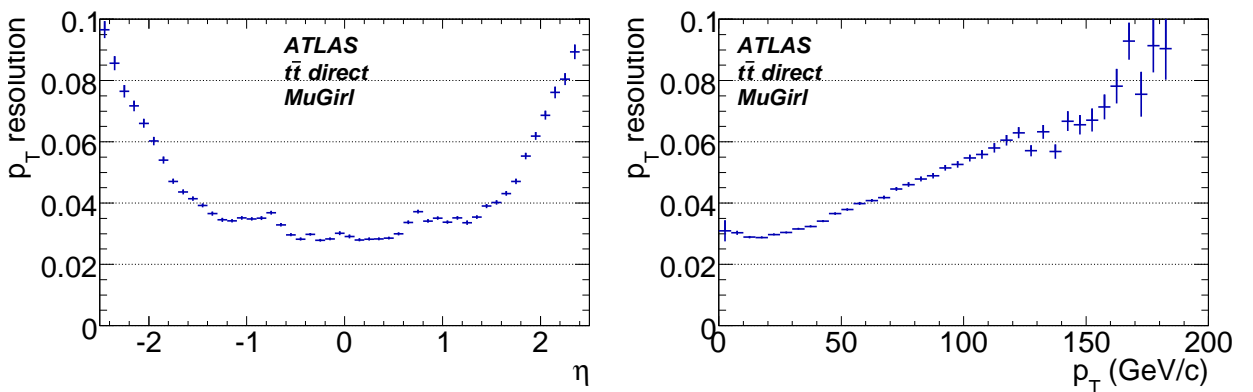


Figure 4.16: Inner detector fractional momentum resolution ( $\Delta p_T/p_T$ ) as a function of  $\eta$  (left) and  $\phi$  (right) in  $t\bar{t}$  direct events. The resolution is the same as that for MuGirl tagged muons because MuGirl does not refit the track from the inner detector. The efficiencies are for  $p_T > 10$  GeV. [47].



showed a small drop in efficiency with little reduction of the fake rate except for the lowest  $p_T$  threshold at high luminosity. The high- $p_T$  fake rate increased at either luminosity because low  $p_T$  standalone muons were matched to the high- $p_T$  inner detector tracks. At low luminosity, Muid  $t\bar{t}$  showed a small decrease in both efficiency and fake rate. When background was added, the fake rate for Muid combined muons did not increase as dramatically as the Moore standalone muons which shows the matching could suppress most of the fakes and the Muid high- $p_T$  fake rates are lower than those of Staco. However, the high-luminosity  $t\bar{t}$  Muid efficiency was significantly worse than of Staco. As expected, the resolution of combined muons was remarkably better than of the standalone muons for  $p_T$  below 100 GeV. Misreconstruction and charge misidentification rates were around 0.01% for the combined muons (0.1% for the standalone).

**Tagged muon performance** Among the two algorithms for tagging muons, MuTag is run to complement Staco so only MuGirl attempts to find all muons in the Muid collection. The MuGirl efficiency and fake rate for  $t\bar{t}$  direct muons are shown in Fig. 4.18. Compared with the combined muon results, MuGirl had lower efficiency and a substantially higher fake rate. Its performance degraded faster in high-luminosity  $t\bar{t}$  sample where background was added. However, in the  $J/\psi$  sample, MuGirl has shown a higher efficiency than Muid for reconstructing the low- $p_T$  muons. As MuGirl does not refit the tracks, its  $p_T$  resolution is just the resolution of the inner detector as shown in Fig. 4.16.

**Merged muon performance** The main focus of the muon merging scheme is to merge the combined and tagged muons separately within each collection, i.e. Staco+MuTag and Muid+MuGirl. Investigation with the Monte Carlo samples in Ref. [47] has shown that the merge provided only a small improvement in the Staco efficiencies but a substantial increase in the fake rate (factor of four) which may reflect the success of the Staco algorithm. For Muid, the efficiency gains were more significant, with the  $J/\psi$  efficiency increased by 10%. The fake rates were increased slightly above the MuGirl rates (factor of five). Overall, Muid+MuGirl performance was similar to that of Staco+MuTag. In both cases, the tagging algorithms provided a significant efficiency improvement for  $p_T$  below 10 GeV.

## Summary

The combined muons will be the starting point for most ATLAS analyses because their better momentum resolution and lower fake rate than the standalone muons or tagged muons. To extend the  $\eta$  coverage to 2.7, the combined muons can be supplemented with the standalone muons. Studies have shown that merging Muid+MuGirl has a performance similar to Staco or Staco+MuTag. Current studies using low- $p_T$  muons from collision data have also confirmed consistency between two muon families.



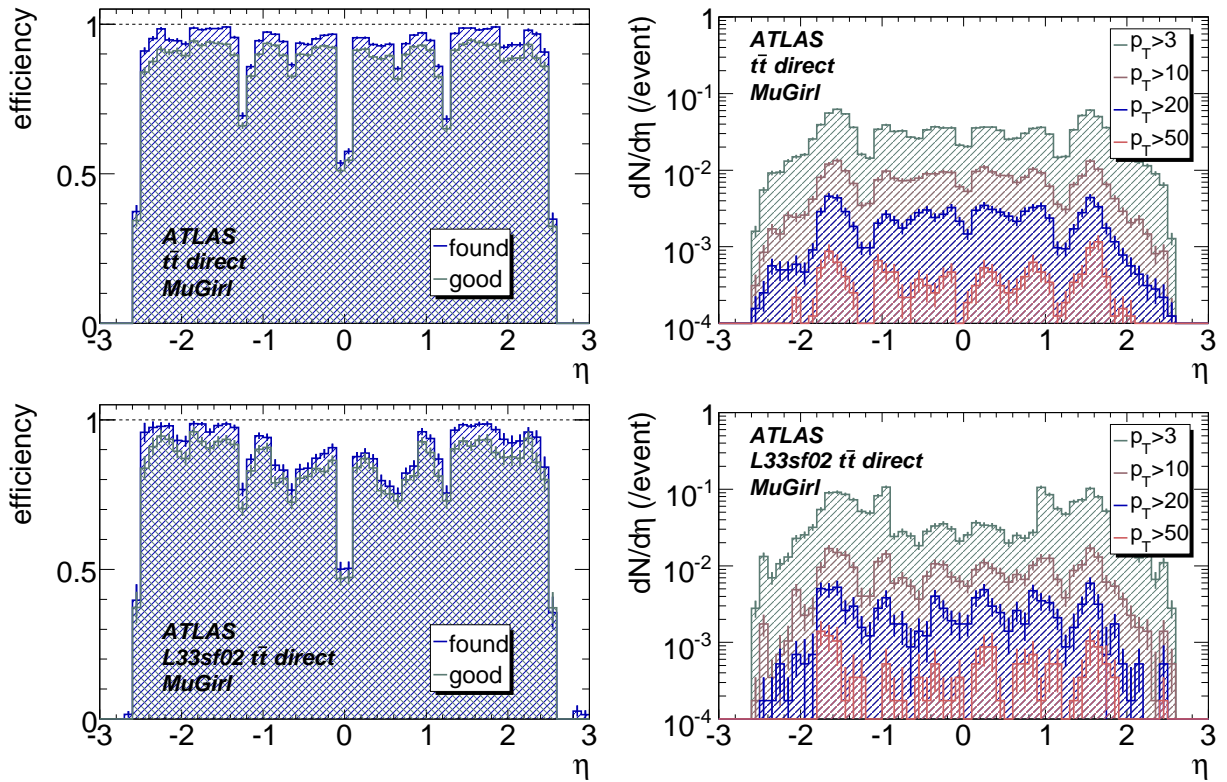


Figure 4.18: MuGirl efficiency (left) and fake rates (right) as a function of true  $\eta$  in  $t\bar{t}$  at low (top) and high (bottom) luminosity. The efficiency plot is for muons with true  $p_T \geq 10$  GeV, where the upper curve in each efficiency plot is the efficiency to find the muon and the lower curve additionally requires a good match between reconstructed and true track parameters [47].

### 4.2.2 Muon triggers

The ATLAS level-1 muon trigger is based on dedicated, fast and finely segmented muon chambers (RPC in the barrel and TGC in the end-caps) and a trigger logic implemented in hardware. The muon trigger system covers a pseudorapidity range up to  $|\eta| \sim 2.4$  and a full azimuthal angle ( $\phi$ ) range. A muon track must be triggered by the coincidence of two or three detector stations within a certain coincidence window. The transverse momentum of a muon candidate is determined by its deviation from the trajectory of a straight line. A three station coincidence is required for any  $p_T$  threshold in the endcap and forward regions ( $|\eta| > 1.05$ ) in order to suppress the background. Consequently the acceptance at large  $|\eta|$  becomes smaller for low- $p_T$  muons. The size of the RoI in the level-1 muon trigger, is  $\Delta\eta \times \Delta\phi = 0.1 \times 0.1$  in the barrel region ( $|\eta| < 1.05$ ) and  $\sim 0.03 \times 0.03$  in the endcap regions ( $1.05 < |\eta| < 2.4$ ). The level-1 trigger decisions are combined in the Muon Central Trigger Processor Interface (MuCTPI) which also calculates the multiplicity of muon candidates for each  $p_T$  threshold over the whole detector. The overlap handling is mandatory to avoid double-counting of single muon tracks. For most of the overlaps, the MuCTPI takes the muon candidate with the higher  $p_T$  when calculating the multiplicity and finding overlapping muons using Lookup Tables (LUT) that are generated based on the Monte Carlo simulation of single-muon events in the region of the level-1 muon system.

The level-2 trigger aims for confirming muon candidates flagged by the level-1 and improving the track parameters for each candidate. It processes data around the RoI provided by the level-1 trigger and use the full granularity of the detector readout within the RoI to make decisions. This software-based selection is performed in two stages. At the first stage, the muFast algorithm is applied to reconstruct the level-1 identified muon RoI in the whole spectrometer using the more precise MDT to provide a new  $p_T$  estimate and a new trigger element. In addition, muFast provides the region of the candidate which is related to track finding in the inner detector. The second stage is to identify combined muons where the muComb algorithm is used to match an ID track with the muFast candidate and to refine the  $p_T$  estimate. As many B decay events involves  $J/\psi$  signatures which can decay

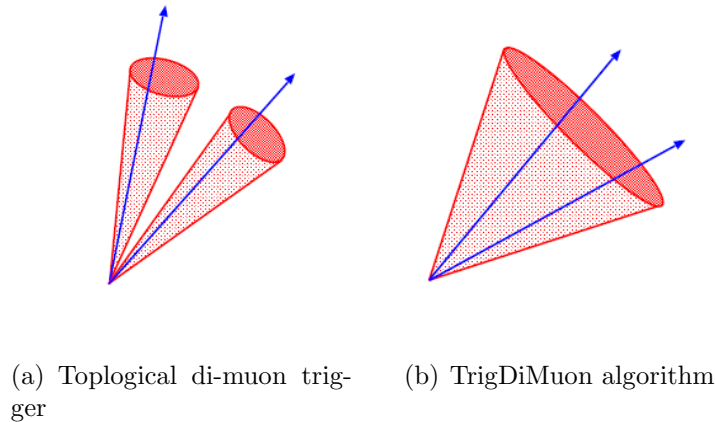


Figure 4.19: Two approaches of the RoI based di-muon trigger

into di-muon pairs, the di-muon triggers in ATLAS are essential for B physics searches. There are two approaches at level-2 for selecting di-muon events from a resonance such as  $J/\psi$  or  $\Upsilon$ , differing in the RoI found at the level-1. The first approach is to start with a di-muon trigger at level-1 which produces two muon RoIs as illustrated in Fig. 4.19(a). In this case, each muon is identified individually in its own RoI and the two muons are subsequently combined to form a resonance with the requirement of the invariant mass. This trigger strategy is known as “topological di-muon trigger”. Alternatively, we can also start with a level-1 single muon trigger and search for two muons in a wider  $\eta$  and  $\phi$  region at level-2, as shown in Fig. 4.19(b). This approach starts with reconstructing tracks in the inner detector and extrapolate the track to the muon spectrometer to tag muon tracks. Since it does not require the second muon identification at the level-1, it has an advantage of large acceptance of  $J/\psi$  events at low- $p_T$ . This trigger algorithm is implemented in the TrigDiMuon algorithm. Tables 4.7 and 4.8 list the efficiencies relative to events accepted at level-1 for TrigDiMuon and topological di-muon trigger run in different trigger chains, after the level-1 trigger, level-2 muFast, and level-2 muComb, with trigger thresholds of 4 GeV and 6 GeV using a sample of  $\Lambda_b \rightarrow J/\psi\Lambda$ , where  $J/\psi \rightarrow \mu(p_T > 2.5 \text{ GeV})\mu(p_T > 4 \text{ GeV})$ . The efficiency of TrigDiMuon for events accepted by level-1 and the level-2 single muon is between 70% for the 4 GeV trigger threshold and 60% for the 6 GeV thresholds. For the topological di-muon trigger, the efficiencies are around 33% for the 4 GeV threshold and 15% for the 6 GeV threshold. The topological di-muon triggers will be operated throughout the main data taking phase whereas the TrigDiMuon algorithm will be applied only during the early running stage.

Chain starting from	TrigDimuon (%)	Topological trigger (%)
level-1	73 (73)	51
muFast	71 (73)	43
muComb	70 (74)	33

Table 4.7: Efficiency, relative to level-1, of the two di-muon trigger algorithms for a trigger threshold of 4 GeV. In parenthesis is the efficiency calculated relative to  $J/\psi$  events that passed the single muon trigger which selects the input to TrigDimuon.

Chain starting from	TrigDimuon (%)	Topological trigger (%)
level-1	75 (75)	56
muFast	67 (77)	25
muComb	60 (78)	15

Table 4.8: Efficiency, relative to level-1, of the two di-muon trigger algorithms for a trigger threshold of 6 GeV. In parenthesis is the efficiency calculated relative to  $J/\psi$  events that passed the single muon trigger which selects the input to TrigDimuon.

# Chapter 5

## Prospects of observing $B_c \rightarrow J/\psi \pi$ events in ATLAS

### 5.1 Introduction

The  $B_c$  meson is a unique state carrying two different heavy flavours. An overview of the theoretical predictions on its properties has been given in Sec. 2.4. The ground state was observed first through semileptonic and subsequently hadronic decays by CDF [11,53,54,55] and D0 [56]. Its mass is predicted with large uncertainties by several theoretical models and the current best precision of the  $B_c$  mass measurement is achieved by CDF:

$$6275.6 \pm 2.9(\text{stat.}) \pm 2.5(\text{syst.}) \text{ MeV [55].}$$

Because of the high energy and high luminosity, the LHC should produce large statistical samples of  $B_c$  states. Measurements of the ground state and excited states will provide precision tests of the models and ultimately, the opportunity to extract the form of the strong potential. The  $B_c$  decays which contain a  $J/\psi \rightarrow \mu^+ \mu^-$  signature are preferable in ATLAS, owing to the efficient muon triggers. In the early data-taking era, we expect to reconstruct the ground state through its hadronic decay,  $B_c \rightarrow J/\psi \pi$ ,  $J/\psi \rightarrow \mu^+ \mu^-$ , in order to minimise dependence of the analysis upon the calorimeter absolute calibration. This chapter is focused on a Monte Carlo analysis of the ATLAS sensitivity for observing the  $B_c \rightarrow J/\psi \pi$  decays at 10 TeV towards  $1\text{fb}^{-1}$  of integrated luminosity (also addressed in document No.2 listed on Pg. ii).

### 5.2 Monte Carlo samples

The branching ratio of  $B_c \rightarrow J/\psi \pi$  is predicted to be  $1.3 \times 10^{-3}$  [37]. The most important backgrounds to the search for this channel are expected to be

1.  $b\bar{b} \rightarrow J/\psi X$  (the symbol X here denotes possible undetected decay particles)
2.  $pp \rightarrow J/\psi X$

3.  $B_c^+ \rightarrow J/\psi K^+$ , where the  $K$  is misidentified as a  $\pi$ . The branching ratio for this channel is predicted [37] to be 0.011%.
4.  $B_c^+ \rightarrow J/\psi \rho^+$ ,  $\rho^+ \rightarrow \pi^+ \pi^0$ , where the neutral pion goes undetected. The branching ratio for this channel is predicted [37] to be 0.4%.
5.  $B_c^+ \rightarrow J/\psi \mu^+ \nu$ , where the  $\mu$  is misidentified as a  $\pi$ .

Because of the large cross sections, channels 1 and 2 are common backgrounds for B decays that contain  $J/\psi$  products. As ATLAS is not expected to perform precise particle identification on pions or kaons, the Cabibbo-suppressed channel  $B_c \rightarrow J/\psi K$  is considered to be the background here. Given the inefficiency of low- $p_T$  muon reconstruction (referring to reconstruction efficiency of 94% for combined muons in  $J/\psi$  decays [47]), channel 5 is also included where the third  $\mu$  may be misidentified as a  $\pi$ .

Events  $b\bar{b} \rightarrow J/\psi X$  and  $pp \rightarrow J/\psi X$  were generated with Pythia [57]. The  $B_c$  mesons were produced with PythiaBc\_i which inherited from Pythia [57] to speed up  $B_c$  events simulation from gluon-gluon fusions, including  $b$  and  $c$  fragmentations as well as the recombination of heavy quarks. The matrix elements for these processes were calculated in Ref. [58]. Both generators applied the CTEQ6L1-LO parton distribution functions [59] to leading order in  $\alpha_s$ . All the B hadron decays were done with EvtGen [60]. We have studied the influence of the above  $B_c$  decay channels on our signal observation at the generator level where we reconstructed the invariant mass of  $B_c$  from the decay products, one  $\mu^+ \mu^-$  pair and one positive charged particle assumed to be a  $\pi$ . The result shown in Fig. 5.1 indicates that channels 4 and 5 have little contribution in the mass range around  $B_c$  ( $M_{B_c}^{PDG} = 6276$  MeV [2]) so that we excluded them in this analysis.

For the signal channel  $B_c^+ \rightarrow J/\psi \pi^+$ ,  $J/\psi \rightarrow \mu^+ \mu^-$ , we required one muon with  $p_T > 6$  GeV and a second with  $p_T > 4$  GeV at the generator level to simulate the effect of the dimuon trigger. Both muons were generated within pseudorapidity region  $|\eta| < 2.5$  corresponding to the coverage of the inner detector. No cuts were placed on the pion. Additionally, we investigated different choices of the  $p_T$  thresholds for di-muons during the event generation which was related to the trigger requirement in the offline reconstruction. Figure 5.2 illustrates the distribution of  $B_c^+$  cross section across the values of the  $p_T$  of the harder and softer muons from the  $J/\psi$  decay without any muon cuts applied at the generator level. The lines overlaid on the plots represent the  $p_T$  thresholds for di-muons: 6+4 GeV ( $p_T > 6$  GeV for the harder muon and  $p_T > 4$  GeV for the softer muon) and 4+4 GeV ( $p_T > 4$  GeV for both muons). Table 5.1 lists the acceptance of signal events passing each  $p_T$  requirement. Although the acceptance of the signal events is increased by 26% if we lower the threshold from 6+4 GeV to 4+4 GeV, the prompt  $J/\psi$  background ( $pp \rightarrow J/\psi X$ ) is increased more dramatically. As a result of that, we conclude that the 6+4 GeV threshold is most appropriate for this analysis.

Studies of the dominant backgrounds use Monte Carlo files of size 500,000 events (for  $pp$ ), 770,000 unique events (for  $b\bar{b}$ ), and 2500 events (for  $B_c \rightarrow J/\psi K$ ). The sample for Channel 2 does not contain Channel 1, and the sample for Channel 1 does not contain Channel 3. The associated production cross sections at 10 TeV centre-of-mass energy are  $\sigma(pp \rightarrow J/\psi X) = 17.0$  nb and  $\sigma(b\bar{b} \rightarrow J/\psi X) = 8.4$  nb relative to the fiducial cuts at

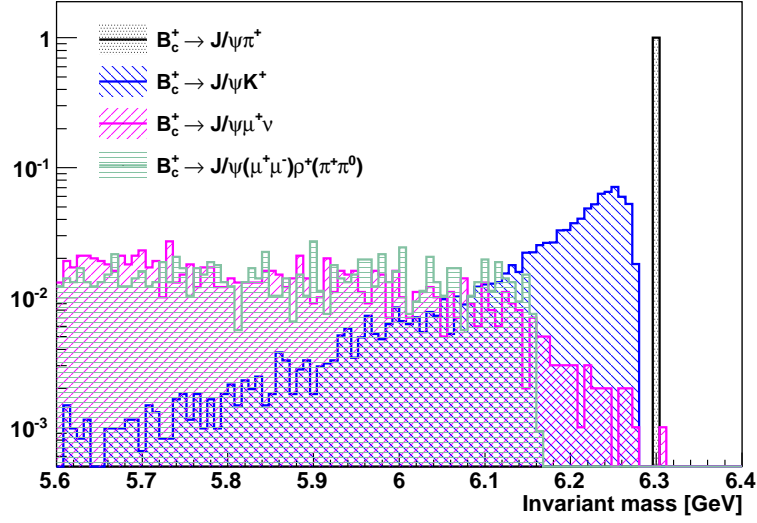


Figure 5.1: A comparison among signal ( $B_c^+ \rightarrow J/\psi \pi^+$ ) and background channels ( $B_c^+ \rightarrow J/\psi K^+$ ,  $B_c^+ \rightarrow J/\psi \rho^+$  and  $B_c^+ \rightarrow J/\psi \mu^+ \nu$ ) at the generator level. We combined the  $\mu^+ \mu^-$  with one other positive charged track as the  $\pi^+$  and reconstructed the invariant mass of this triplet for each  $B_c^+$  decay channel. Channels  $B_c^+ \rightarrow J/\psi \rho^+$  and  $B_c^+ \rightarrow J/\psi \mu^+ \nu$  are not considered to be dominant here due to their extremely small contributions in the mass range around  $M_{PDG}(B_c)$  ( $\sim 6276$  MeV).

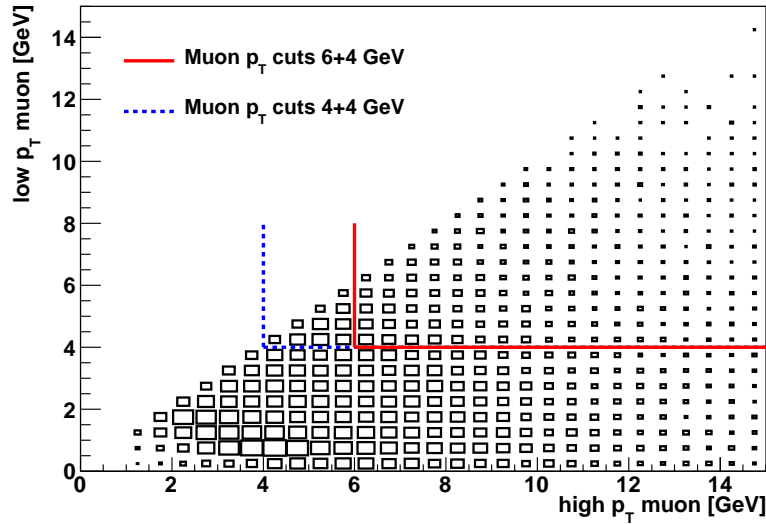


Figure 5.2: Distribution of  $B_c^+$  cross section as a function of the two muon transverse momenta without any cut applied during the event generation. The overlaid lines represent  $p_T$  thresholds for muons.



$p_T$ thresholds for muons [GeV]	Event Passed	Total Number	Acceptance[%]
$p_T^{\mu^{(1,2)}} > 6(4)$ GeV	3530	20571	17.2
$p_T^{\mu^{(1,2)}} > 4(4)$ GeV	4461	20571	21.7

Table 5.1: Acceptance of signal events corresponding to different  $p_T$  thresholds for dimuons.

the generator level on the two muons (of which one has  $p_T > 6$  GeV and the other has  $p_T > 4$  GeV, as mentioned above). The two muons are required both to be found in pseudorapidity region  $|\eta| < 2.5$ . These Monte Carlo samples correspond to  $30 \text{ pb}^{-1}$  in  $pp$ ,  $91 \text{ pb}^{-1}$  in  $b\bar{b}$ , and  $25 \text{ fb}^{-1}$  in  $B_c \rightarrow J/\psi K$ .

Simulation and reconstruction used the GEANT4-based model of the ATLAS nominal geometry. Event reconstruction was based on the standard ATLAS software framework. The ATLAS trigger menu was simulated, with selected events accepted by the Level 1 (L1) 2MU4 and High Level 2mu4 triggers [47]<sup>I</sup>. These triggers required that 2 RoI's at L1 passed the lowest  $p_T$  threshold with open coincidence windows. Both were further confirmed by high level algorithms which required  $p_T > 3$  GeV for candidates within  $|\eta| < 1.05$  and  $p_T > 2.5$  GeV for those in the  $|\eta|$  region between 1.05 and 2.5. The trigger efficiency is found to be 55% for the signal sample.

The detector reconstruction efficiency,  $\epsilon_{recon}$ , for reconstructing the combination of two muons and the pion in signal events before offline selection is found to be 78%.

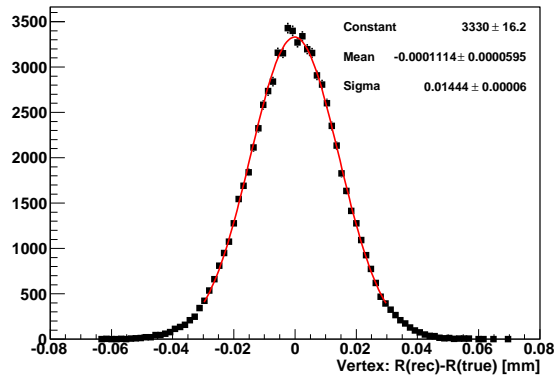
### 5.3 Event offline analysis

The primary vertices (PV, see Fig. 5.3(a)) were formed from tracks passing quality cuts and having  $p_T > 500$  MeV with impact parameter  $|d_0| < 1.0$  mm and axial distance  $|z_0| < 1000$  mm relative to the beam spot. In the case of more than one primary vertex reconstructed offline, we used the one with the largest number of tracks originating at the vertex as well as a non-zero covariance matrix determinant.

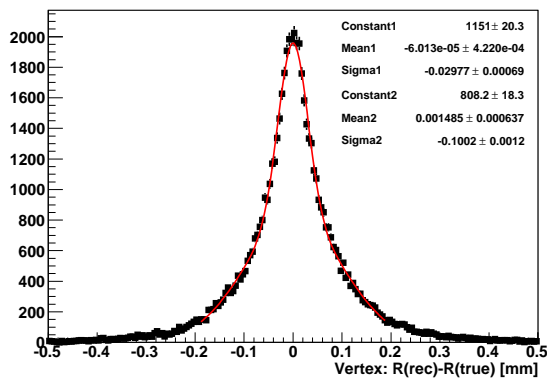
We required tracks to have at least one silicon hit in the Pixel or SCT detectors. Combined muons were retrieved and their inner detector track parameters were used for the event reconstruction. It began by forming the di-muon vertices (see Fig. 5.3(b)) and invariant masses for all pairs of oppositely signed muons with individual  $p_T > 6$  GeV and  $> 4$  GeV and pseudorapidity  $|\eta| < 2.5$ . Di-muon pairs for which the reconstruction of the vertex involved a singular covariance matrix or one with non-positive diagonal elements, those for which the vertex first approximation failed, and those for which the vertex fit did not converge within a specified number of steps were rejected. Those that were not rejected at this stage were classified (see, e.g., Table 5.2) as having a ‘‘Successful vertex fit.’’ Di-muon pairs for which the vertex  $\chi^2/ndof$ <sup>II</sup>  $< 6$  were retained as  $J/\psi$  candidates.

<sup>I</sup>The trigger menu is bound to the official ATLAS software release used for detector simulation. At the time we prepared the Monte Carlo samples, the trigger menu was still under development. Although the MU6MU4 trigger is better for this analysis according to our investigation, the trigger item was not included in the trigger menu at that time. Instead we chose 2MU4 trigger item.

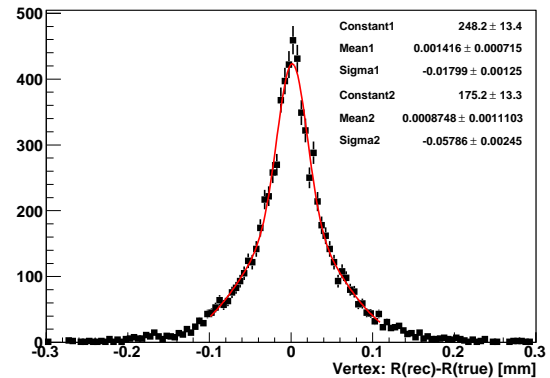
<sup>II</sup>ndof: number of degrees of freedom.



(a) The radial coordinate of the primary vertex.



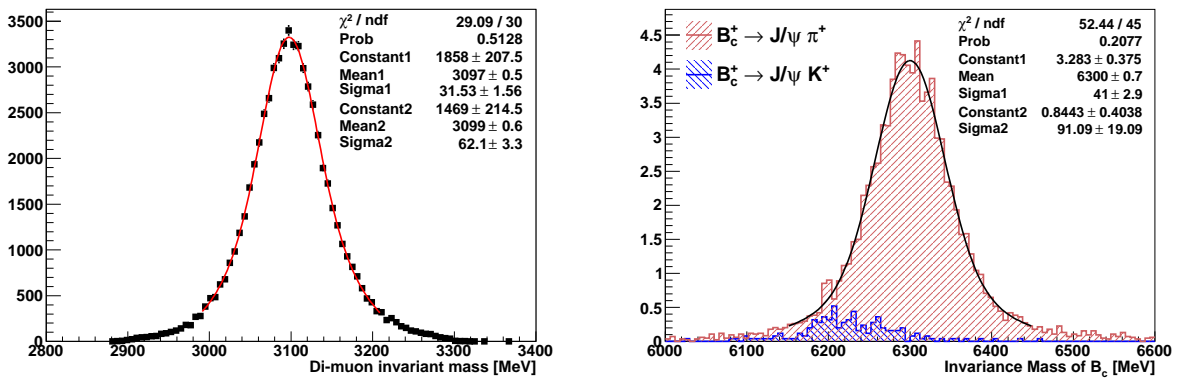
(b) The radial coordinate of the dimuon vertex.



(c) The radial coordinate of the secondary vertex.

Figure 5.3: Resolutions of the radial coordinate of the (a) primary, (b) di-muon, and (c) secondary vertices, for signal events only. Figure 5.3(a) is fitted with a single Gaussian while Figures 5.3(b) and 5.3(c) are approximated by double Gaussians.

A cut of  $\pm 4\sigma$  ( $\pm 200$  MeV) around the  $J/\psi$  mass was applied. The distribution of the  $J/\psi$  invariant mass from the signal sample is shown in Fig. 5.4(a) and the shape was modelled by a double Gaussian function. It is clear that one width from the fit is twice as high as the other one which is due to the different momentum resolutions measured in the detector barrel and end-cap regions. Looking into more details, we reconstructed the  $J/\psi$  masses from both muons in the barrel (Fig. 5.5(a)) or end-cap (Fig. 5.5(b)) region and the width of each single Gaussian function coincided with the one in the double Gaussian fit. The pseudorapidity variation of the track parameter resolutions was also seen in the tracking performance study [47] (previously shown in Fig. 4.3). For the selected  $J/\psi$  candidates,



(a) The reconstructed  $J/\psi$  mass in the full  $\eta$  region, for signal events only. Some of the  $J/\psi$ 's in this graph were subsequently rejected by other selection requirements.

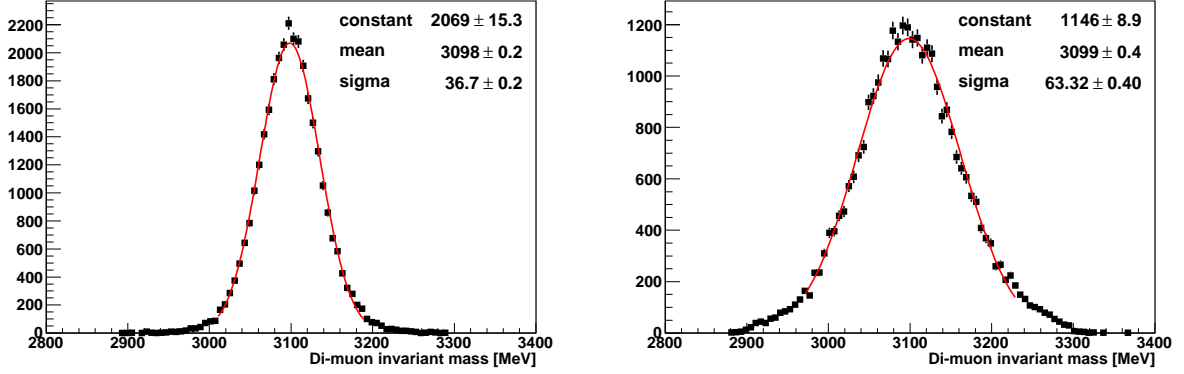
(b) The reconstructed  $B_c$  mass, for signal events and  $B_c^+ \rightarrow J/\psi K^+$  background only. Both distributions were scaled to the number expected for  $1 \text{ fb}^{-1}$  without trigger efficiency.

Figure 5.4: The reconstructed  $J/\psi$  and  $B_c$  masses, for signal events. A double Gaussian fit was applied in Fig. 5.4(a) to account for differing resolutions on tracks in the detector barrel and end-cap regions. In Fig. 5.4(b), the mass distribution of  $B_c^+ \rightarrow J/\psi \pi^+$  was modelled by a modified double Gaussian which has one common mean and two different sigmas. The object is to extract the particle mass and predict the dominant resolution on the  $\mu\mu\pi$  triplets.

the muon  $p_T$  values were revised to give the world average  $J/\psi$  mass ( $M_{J/\psi}^{PDG} = 3096.92$  MeV [2]). Excluding these muon pairs, all remaining tracks with charge  $> 0$ <sup>III</sup>, impact parameter significance  $|d_0|/\sigma(d_0) > 1.8$ ,  $|\eta| < 2.5$ , and  $p_T > 3$  GeV were considered to be pions. At least one charged pion in the event was required.

For events that passed the  $J/\psi$  and pion selection requirements, we formed the invariant masses of all candidate  $\mu\mu\pi$  combinations ( $M_{B_c}^{recon}$ ) and required  $|M_{B_c}^{recon} - M_{B_c}^{PDG}| < 500$  MeV. Each  $\mu\mu\pi$  triplet that passed this was fit to a common secondary vertex, SV (see Fig. 5.3(c)). The SV  $\chi^2/ndof$  was required to be less than 4. The contribution of the pion to that  $\chi^2$  must be less than 3.

<sup>III</sup>The requirement of positive charge was applied only in the analysis of the Monte Carlo sample  $B_c^+ \rightarrow J/\psi \pi^+$  events. With sufficient data we will include both charge species to reconstruct  $B_c^\pm$  mesons.



(a) The reconstructed  $J/\psi$  mass in the barrel regions, for signal events only.

(b) The reconstructed  $J/\psi$  mass in the end-cap regions, for signal events only.

Figure 5.5: The reconstructed  $J/\psi$  mass in the barrel (Fig. 5.5(a)) and end-cap regions (Fig. 5.5(b)).

The topology for the decay  $B_c \rightarrow J/\psi \pi$  is illustrated in Fig. 5.6. For each  $B_c$  candidate we computed the transverse decay length,  $L_{xy} = [(x_{SV} - x_{PV})p_x + (y_{SV} - y_{PV})p_y]/p_T$ , and the proper decay length,  $\lambda = L_{xy}M(B_c)/p_T(B_c)$ .  $L_{xy}$  is a signed variable which is negative if the  $B_c$  particle appears to decay before the secondary vertex of its production. We chose the proper decay length rather than the transverse decay length and proper time in order to minimise the dependence upon the  $p_T$  of the  $B_c$ . Figure 5.7 shows the proper decay length distribution of the events at this step. We required  $\lambda > 0.08$  mm. Lastly we applied a vertex-constrained fit to each  $B_c$  candidate, recomputed the momenta of the three tracks, and re-formed the invariant mass of this  $\mu\mu\pi$  trio (Figure 5.4(b)). That “refitted” mass must lie within 100 MeV of  $M_{B_c}^{PDG}$ . If an event retained more than one  $B_c$  candidate after this set of criteria, the one with the smallest  $\chi^2/n_{dof}$  of the secondary vertex fit was used. In practice the number of events for which this occurred was negligible.

Figures 5.8(a)-5.8(e) show the variation in the significance ( $S/\sqrt{S+B}$ ) of cuts on each of the above parameters over the relevant kinematic range, where  $S$  is the predicted number of signal events and  $B$  is the predicted number of background events. Although the cuts were optimised in sequence, they have also been varied individually and shown to be robust. The impact parameter in  $r - \phi$  of the  $B_c$  candidate with respect to the PV after the above cuts was also considered (Fig. 5.9) but ultimately excluded from the selection criteria. The opening angle  $\alpha$  between the  $J/\psi$  and the pion track (Fig. 5.10(a)), and the pointing angle  $\theta$  between the direction of the  $B_c$  momentum and the vector from the PV to the SV (Fig. 5.10(b)) were also examined and discarded. We have examined the effect of removing the dimuon from the primary vertex and refitting the vertex, but found it to be negligible.

Table 5.2 itemises the efficiency for each step in the selection of the  $\mu\mu\pi$  triplets that will be combined to reconstruct the  $B_c$ . We refer to this as the kinematic efficiency,  $\epsilon_{kin}$ . Tables 5.3, 5.4, and 5.5 show the efficiency for rejecting background with each step in the formation of the triplets. And Tables 5.6, 5.7, 5.8, and 5.9 summarise the contribution of

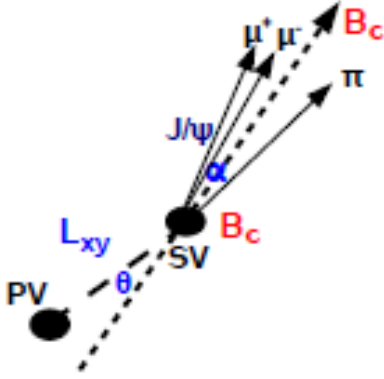


Figure 5.6: A diagram of the three-track decay topology for  $B_c \rightarrow J/\psi(\rightarrow \mu^+\mu^-)\pi$ .

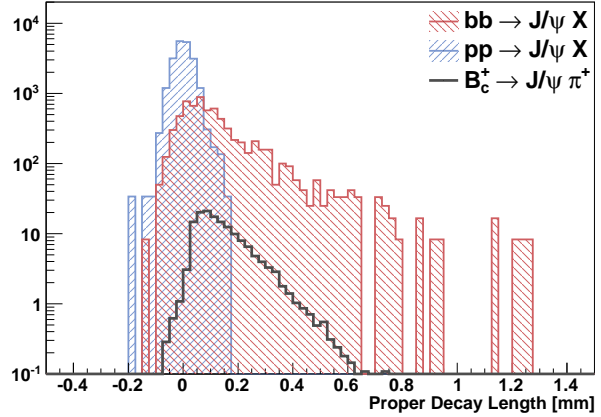


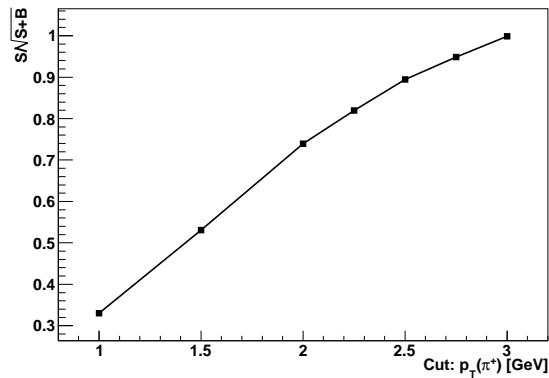
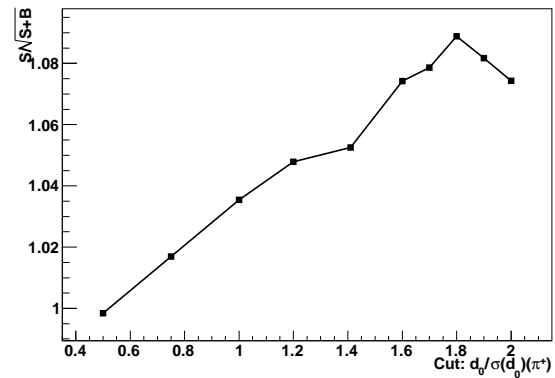
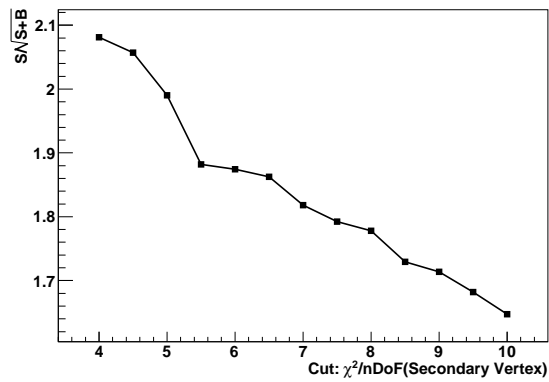
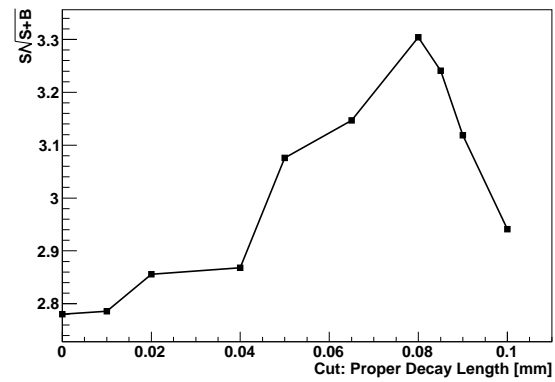
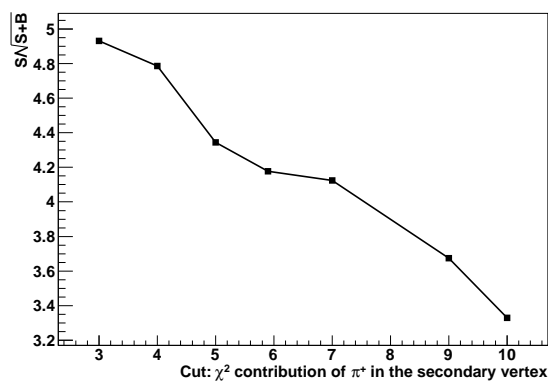
Figure 5.7: The proper decay length for reconstructed signal and background, scaled for an integrated luminosity of  $1 \text{ fb}^{-1}$ .

the selection requirements placed upon the  $\mu\mu\pi$  triplets to the total signal efficiency and background rejection factor.

Particle type	Requirement	Signal events passed	Eff. (%)
$J/\psi$	Initial sample	78109	-
	$p_T^{\mu_{1(2)}} > 6(4) \text{ GeV} \ \& \  \eta  < 2.5 \ \& \  M_{\mu\mu} - M_{J/\psi}^{PDG}  < 200 \text{ MeV}$	65010	83.23
	Successful vertex fit	64992	99.97
	Vtx $\chi^2/ndof < 6$	63208	97.26
$\pi^+$	$p_T > 3 \text{ GeV} \ \& \  \eta  < 2.5$	27850	44.06
	$ d_0 /\sigma(d_0) > 1.8$	13336	47.89
Triplet		13336	17.07

Table 5.2: Efficiencies for stages in the selection of the muons and pions produced in the decay of the  $B_c^+$ .

The probability for  $b\bar{b}$  events to pass the selection procedure was computed by dividing the number of events that survived the selection in Table 5.7 (4) by the number of events in the initial sample of Table 5.3 (767032); that  $b\bar{b}$  survival probability is  $(5.2 \pm 2.6) \times 10^{-6}$ . The analogous calculation for  $B_c \rightarrow J/\psi K$  gives survival probability  $0.046 \pm 0.004$ . The upper limit of the survival probability for  $pp$  background in the  $[6200 \text{ MeV}, 6400 \text{ MeV}]$  mass window is estimated to be  $(0.4 \pm 0.4) \times 10^{-6}$ .

(a) The significance of the cut on pion  $p_T$ .(b) The significance of the cut on pion  $|d_0|/\sigma(d_0)$ .(c) The significance of the cut on  $\chi^2/ndof$  of the  $\mu\mu\pi$  vertex.(d) The significance of the cut on proper decay length of the  $B_c$ .(e) The significance of the cut on the contribution of the pion to the total  $\chi^2$  of the  $\mu\mu\pi$  vertex.Figure 5.8: The significance,  $S/\sqrt{S+B}$ , versus parameters involved in signal selection.

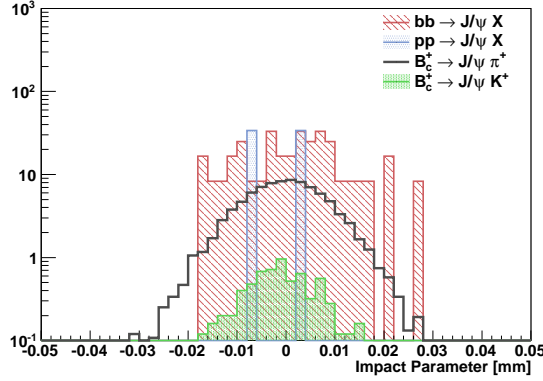


Figure 5.9: The impact parameter in  $r - \phi$  of the  $B_c$  candidate with respect to the PV for signal and background.

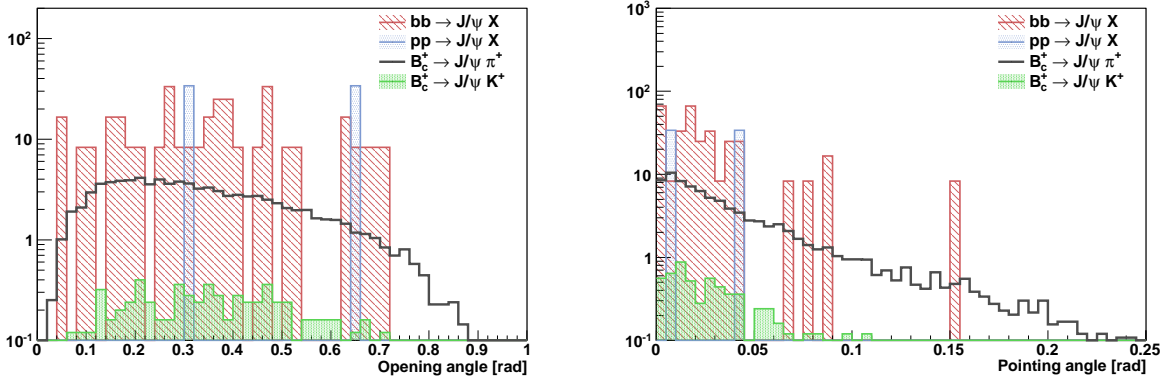


Figure 5.10: Distributions of the opening angle (left) and the pointing angle (right) after offline selection.

Particle type	Requirement	$b\bar{b}$ events passed	Cum. rej. eff.(%)
$J/\psi$	Initial sample	767032	-
	$p_T^{\mu^{1(2)}} > 6(4) \text{ GeV} \ \& \  \eta  < 2.5 \ \& \  M_{\mu\mu} - M_{J/\psi}^{PDG}  < 200 \text{ MeV}$	610138	20.45
	Successful vertex fit	610004	20.47
	Vtx $\chi^2/ndof < 6$	593216	22.66
$\pi^+$	$p_T > 3 \text{ GeV} \ \& \  \eta  < 2.5$	353193	53.95
	$ d_0 /\sigma(d_0) > 1.8$	180558	76.46
Triplet	-	180558	76.46

Table 5.3: Efficiencies, including cumulative, for rejection of  $b\bar{b}$  background events at stages in the selection of the  $\mu\mu\pi$  triplet.

Particle type	Requirement	$pp$ events passed	Cum. rej. eff.(%)
$J/\psi$	Initial sample	499998	-
	$p_T^{\mu^{1(2)}} > 6(4)$ GeV & $ \eta  < 2.5$ & $ M_{\mu\mu} - M_{J/\psi}^{PDG}  < 200$ MeV	450438	9.91
	Successful vertex fit	450335	9.93
	Vtx $\chi^2/ndof < 6$	437984	12.40
$\pi^+$	$p_T > 3$ GeV & $ \eta  < 2.5$	141681	71.66
	$ d_0 /\sigma(d_0) > 1.8$	43430	91.31
Triplet	-	43430	91.31

Table 5.4: Efficiencies, including cumulative, for rejection of  $pp$  background events at stages in the selection of the  $\mu\mu\pi$  triplet.

Particle type	Requirement	$B_c \rightarrow J/\psi K$ event passed	Cum. rej. eff.(%)
$J/\psi$	Initial sample	2500	-
	$p_T^{\mu^{1(2)}} > 6(4)$ GeV & $ \eta  < 2.5$ & $ M_{\mu\mu} - M_{J/\psi}^{PDG}  < 200$ MeV	2027	18.92
	Successful vertex fit	2026	18.96
	Vtx $\chi^2/ndof < 6$	1973	21.08
$\pi^+$	$p_T > 3$ GeV & $ \eta  < 2.5$	1068	57.28
	$ d_0 /\sigma(d_0) > 1.8$	614	75.44
Triplet	-	614	75.44

Table 5.5: Efficiencies, including cumulative, for rejection of  $B_c^+ \rightarrow J/\psi K^+$  background events at stages in the selection of the  $\mu\mu\pi$  triplet.

Selection requirement	Signal events passed	Eff. (%)
Initial sample	13336	-
$ M_{B_c}^{recon} - M_{B_c}^{PDG}  < 500$ MeV	13169	98.75
Successful $J/\psi - \pi$ vertex fit	13167	99.98
SV $\chi^2/ndof < 4$	12773	97.01
$\lambda > 0.08$ mm	9047	70.83
$\chi^2(\pi^+) < 3$	7613	84.15
$ M^{\text{refitted}} - M^{PDG}  < 100$ MeV	6606	86.77
Total	6606	49.54

Table 5.6: Signal retention efficiency for the selection requirements described.



Selection requirement	$b\bar{b}$ events passed	Cum. rej. eff. (%)
Initial sample	180558	-
$ M_{B_c}^{recon} - M_{B_c}^{PDG}  < 500\text{MeV}$	2145	98.81
Successful $J/\psi - \pi$ vertex fit	1769	99.02
SV $\chi^2/ndof < 4$	243	99.87
$\lambda > 0.08\text{mm}$	92	99.95
$\chi^2(\pi^+) < 3$	28	99.98
$ M^{\text{refitted}} - M^{PDG}  < 100 \text{ MeV}$	4	99.998
Total	4	99.998

Table 5.7: Efficiency for rejection of the background  $b\bar{b} \rightarrow J/\psi X$  using the selection requirements described.

Selection requirement	$pp$ events passed	Cum. rej. eff. (%)
Initial sample	43430	-
$ M_{B_c}^{recon} - M_{B_c}^{PDG}  < 500\text{MeV}$	689	98.41
Successful $J/\psi - \pi$ vertex fit	551	98.73
SV $\chi^2/ndof < 4$	244	99.44
$\lambda > 0.08\text{mm}$	9	99.98
$\chi^2(\pi^+) < 3$	2	100.00
$ M^{\text{refitted}} - M^{PDG}  < 100 \text{ MeV}$	0	100.00
Total	0	100.00

Table 5.8: Efficiency for rejection of the background  $pp \rightarrow J/\psi X$  using the selection requirements described.

Selection requirement	$B_c^+ \rightarrow J/\psi K^+$ events passed	Cum. rej. eff. (%)
Initial sample	614	-
$ M_{B_c}^{recon} - M_{B_c}^{PDG}  < 500\text{MeV}$	318	48.21
Successful $J/\psi - \pi$ vertex fit	314	48.86
SV $\chi^2/ndof < 4$	303	50.65
$\lambda > 0.08\text{mm}$	218	64.50
$\chi^2(\pi^+) < 3$	173	71.82
$ M^{\text{refitted}} - M^{PDG}  < 100 \text{ MeV}$	116	81.11
Total	116	81.11

Table 5.9: Efficiency for rejection of the background  $B_c^+ \rightarrow J/\psi K^+$  using the selection requirements described.

## 5.4 Comparison with the channel $B^+ \rightarrow J/\psi K^+$

The kinematics of  $B_c^+ \rightarrow J/\psi\pi^+$  and  $B^+ \rightarrow J/\psi K^+$  are similar, apart from the mass, lifetime, impact parameter and momentum of the meson track. We applied the analysis to the Monte Carlo sample  $B^+ \rightarrow J/\psi K^+$  in order to cross-check the reconstructed mass resolution of the  $B_c$  signal and to check for any unexpected response to the selection requirements. We have applied the same analysis cuts as for the  $B_c \rightarrow J/\psi\pi$  selection described in Sec. 5.3 to a sample of 51704  $B^+ \rightarrow J/\psi K^+$  events and graphed the mass of the reconstructed  $B$  candidates in Fig. 5.11. Fitting with a double Gaussian with common mean value and different sigmas, we recovered the mass 5280 MeV and an average resolution of 34 MeV. The result from the same fit to the distribution of selected  $B_c^+$  events recovered the  $B_c$  mass of 6300 MeV with core resolution 41 MeV (Fig. 5.4(b)). Both reconstructed masses are consistent with their input values from Monte Carlo generation, 5279 MeV for  $B^+$  and 6300 MeV for  $B_c^+$ . The resolution of the  $B_c^+$  can be predicted from the reconstructed  $B^+$  resolution scaled by the ratio of the two particles' masses,  $M(B_c)/M(B^+) = 6286/5279$  [2], and this is in agreement with the reconstructed value. Table 5.10 summarises the efficiency of each selection requirement for retaining the  $B^+$  signal. As we expected, individual cut efficiencies have values similar to those for  $B_c$  signal retention in Table 5.6.

We expect to implement the same procedure on real data when sufficient statistics are available. The  $B^+$  signal will be extracted from the data under the same selection requirements but with the third track assumed to be a kaon.

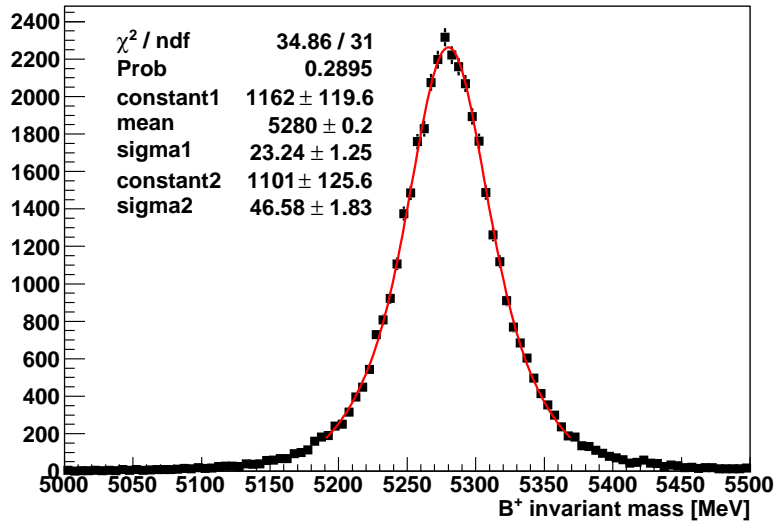


Figure 5.11: The invariant mass distribution of  $B^+$  mesons reconstructed through their decay to  $J/\psi K^+$ .

Selection requirement	Signal events passed	Eff (%)
Initial sample	51704	-
$ M_{B^+}^{recon} - M_{B^+}^{PDG}  < 500\text{MeV}$	51535	99.67
Successful $J/\psi - K$ vertex fit	51528	99.99
SV $\chi^2/ndof < 4$	50697	98.39
$\lambda > 0.08\text{mm}$	48154	94.98
$\chi^2(\pi^+) < 3$	40697	84.51
$ M^{\text{refitted}} - M^{PDG}  < 100\text{ MeV}$	38571	94.78
Total	38571	74.60

Table 5.10:  $B^+ \rightarrow J/\psi K^+$  signal retention efficiency for the selection requirements described.

## 5.5 Results

Following the offline selection, we scaled the distributions of the invariant mass reconstructed from  $B_c^+ \rightarrow J/\psi \pi^+$ ,  $b\bar{b} \rightarrow J/\psi X$  and  $B_c^+ \rightarrow J/\psi K^+$  to  $1\text{ fb}^{-1}$ , including the trigger efficiency and estimated the sensitivities of observing the  $B_c \rightarrow J/\psi \pi$  decay and reconstructing the  $B_c$  meson mass.

### Event yield

For the signal event yield, we estimate the number of signal events using the cross sections obtained from Pythia and the efficiencies from our study. The Pythia production cross section for  $B_c^\pm \rightarrow J/\psi(\rightarrow \mu_{p_T>6\text{GeV}}\mu_{p_T>4\text{GeV}})\pi^\pm$  is 1.2 pb. This includes the branching ratios  $\text{BR}(B_c \rightarrow J/\psi\pi) = 1.3 \times 10^{-3}$  [37] and  $\text{BR}(J/\psi \rightarrow \mu^+\mu^-) = (5.93 \pm 0.6)\%$  [2]. It also includes a factor of two to cover both charge species. The combined trigger efficiency  $\epsilon_{trig}$  is estimated to be 0.55. The reconstruction efficiency  $\epsilon_{recon}$  is 0.78. The kinematic efficiency  $\epsilon_{kin}$  is 0.17. The selection efficiency  $\epsilon_{sel}$  for events in which a triplet has been found is 0.50. Combining these we estimate the number of observed  $B_c^\pm \rightarrow J/\psi\pi^\pm$  decays,  $S$ , to be

$$S = \sigma(B_c^\pm \rightarrow J/\psi(\rightarrow \mu_{p_T>6\text{GeV}}\mu_{p_T>4\text{GeV}})\pi^\pm) \cdot \epsilon_{recon} \cdot \epsilon_{kin} \cdot \epsilon_{trig} \cdot \epsilon_{sel} \cdot \int \mathcal{L} dt . \quad (5.1)$$

This predicts  $44 \pm 0.6$  fully reconstructed  $B_c^\pm$  events in  $1\text{ fb}^{-1}$ .

To estimate the number  $B$  of background events, we combine the Pythia cross sections at  $\sqrt{s} = 10\text{ TeV}$  for  $pp \rightarrow b\bar{b} \rightarrow J/\psi(\rightarrow \mu_{p_T>6\text{GeV}}\mu_{p_T>4\text{GeV}})X$ ,  $pp \rightarrow J/\psi(\rightarrow \mu_{p_T>6\text{GeV}}\mu_{p_T>4\text{GeV}})X$ , and  $pp \rightarrow B_c \rightarrow J/\psi K$  (8.4 nb, 17.0 nb, and 100 fb, respectively) with the survival probability for each of these backgrounds,  $(5.6 \pm 2.6) \times 10^{-6}$  for  $b\bar{b}$  and  $0.046 \pm 0.004$  for  $B_c \rightarrow J/\psi K$ , and the upper limit  $(0.4 \pm 0.4) \times 10^{-6}$  for  $pp$ , and the trigger efficiency ( $\epsilon_{trig} = 0.55$ ), to predict

$$B = [\sigma(pp \rightarrow J/\psi X) \cdot \epsilon_{pp} + \sigma(b\bar{b} \rightarrow J/\psi X) \cdot \epsilon_{b\bar{b}} + \sigma(pp \rightarrow B_c(\rightarrow J/\psi K)X) \cdot \epsilon_{J/\psi K}] \cdot \epsilon_{trig} \cdot \int \mathcal{L} dt . \quad (5.2)$$

This predicts  $30 \pm 12$  background events in  $1 \text{ fb}^{-1}$ . The expected number of events from the signal and background channels are shown in Table 5.11.

	Event type	Event yield expected for $1 \text{ fb}^{-1}$	B/S
Signal	$B_c \rightarrow J/\psi \pi$	$44 \pm 0.6$	
Background	$b\bar{b} \rightarrow J/\psi X$	$24 \pm 12$	$0.5 \pm 0.3$
	$B_c \rightarrow J/\psi K$	$2.6 \pm 0.2$	$0.06 \pm 0.005$
	$pp \rightarrow J/\psi X$	$3.7 \pm 3.7$	$0.08 \pm 0.08$

Table 5.11: Expected number of events from the signal and background channels for  $1 \text{ fb}^{-1}$  including trigger efficiency in the mass region  $[6200 \text{ MeV}, 6400 \text{ MeV}]$  and the ratio of background to signal events.

In total, the procedure predicts the number of events in the  $[6200 \text{ MeV}, 6400 \text{ MeV}]$  mass window from the background samples,  $B$ , to be  $30 \pm 12$  and the one from the signal contribution,  $S$ , to be  $44 \pm 0.6$ . Assuming the expected number of background events is  $B = 42$ , the probability that these background events will fluctuate to a total number of events greater than or equal to  $S + B = 86$  is given by the Poisson probability,

$$\begin{aligned}
 P(n \geq n_0) &= \sum_{n \geq n_0} \frac{e^{-\mu} \mu^n}{n!} \quad (\mu = 42, n_0 = 86) \\
 &\sim 1.8 \times 10^{-9}
 \end{aligned} \tag{5.3}$$

which is equivalent to a  $5.9\sigma$  fluctuation of a Gaussian distribution. Thus, the peak's significance is  $5.9\sigma$ . (If we take  $B = 30$ , the significance corresponds to  $6.7\sigma$ )

We have also performed a ratio-of-likelihood test to cross-check our estimate of the signal excess. We compare two hypotheses for the mass distribution of the background and signal events over the regime  $[6200 \text{ MeV}, 6400 \text{ MeV}]$ . First, we apply an unbinned likelihood fit to the selected events. The combined mass shape is modelled with a Gaussian function for the signal and a first order polynomial function for the background. The likelihood obtained from the fit is denoted as  $L_1$ . Then we apply another unbinned fit of a first order polynomial to the same events with the assumption that no signal is present. The likelihood for this null hypothesis is  $L_0$ . The ratio of likelihoods,  $L_0/L_1$ , yields a probability for the null hypothesis that is less than the one given by the Poisson probability. The hypothesis test is in agreement with the Poisson probability test, confirming that the significance of the observation of  $B_c^\pm \rightarrow J/\psi \pi^\pm$  exceeds 5.9 standard deviations.

### Sensitivity of mass reconstruction

We produced a binned distribution in the interval  $[6050 \text{ MeV}, 6750 \text{ MeV}]$  and smoothed <sup>IV</sup> the scaled backgrounds to extract the shape as precisely as possible with a linear function.

<sup>IV</sup>A numerical method to reduce the statistical fluctuations in histograms. It is implemented in ROOT based on the so-called ‘‘353QH twice’’ algorithm presented by J. Friedman in Proc.of the 1974 CERN School of Computing, Norway, 11-24 August, 1974.

We then scaled the signal distribution to  $1 \text{ fb}^{-1}$  and applied the same binning. Lastly we applied a combined fit to the mass distribution of the signal and background events over the regime  $[6050 \text{ MeV}, 6750 \text{ MeV}]$ . The combined mass shape is modelled with a Gaussian for the signal and a first order polynomial function for the background. The result shows the mass of  $6291 \pm 10 \text{ MeV}$  with resolution ( $\sigma$ )  $61 \pm 13 \text{ MeV}$ . The mass distribution of the reconstructed  $B_c$  mesons and the principal sources of background, for  $1 \text{ fb}^{-1}$  of data, is shown in Fig. 5.12. A smaller-binned fit of the signal and Cabibbo-suppressed background alone is shown in Fig. 5.4(b).

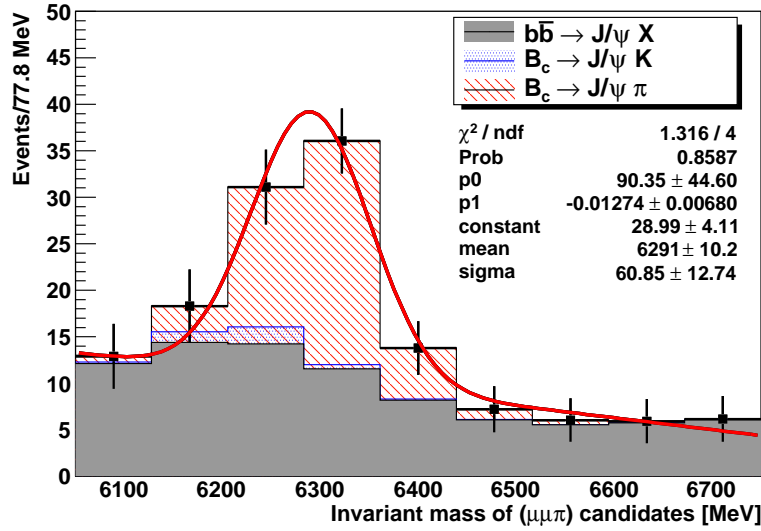


Figure 5.12: The invariant mass distribution of the reconstructed  $B_c$  signal and background after all the cuts apart from the final mass cut, with trigger efficiency included, for integrated luminosity  $1 \text{ fb}^{-1}$ . The contribution of  $pp$  background, which is negligible, is not shown.

The combined mass distribution shown in Fig. 5.12 is limited by the statistics of Monte Carlo background samples  $b\bar{b} \rightarrow J/\psi X$  and  $pp \rightarrow J/\psi X$ . The problem will be reduced when we analyse the data. In this study, to compensate for that, we also generated a toy Monte Carlo background sample with the statistics 10 times as large as our background samples. The probability density function used in the generation was defined by a first order polynomial function where the parameters were extracted from the background events that passed our offline selections. An unbinned maximum likelihood fit was then applied to the combined mass distribution of the signal and toy Monte Carlo events over  $[6050$

MeV, 6750 MeV]. The likelihood function was defined by:

$$L = \prod_{i=1}^n [f_{\text{sig}} S(m, \mu, \sigma) + (1 - f_{\text{sig}}) B(m, b)]$$

$$S(m, \mu, \sigma) = \frac{1}{\sqrt{2\pi}\sigma} e^{-\frac{(m-\mu)^2}{2\sigma^2}}$$

$$B(m, b) = 1 + bm \tag{5.4}$$

$$\tag{5.5}$$

where  $S(m, \mu, \sigma)$  was the probability density function for the signal modelled by a Gaussian function, and  $B(m, b)$  is for the toy Monte Carlo background which was parameterised by a first order polynomial. The result is shown in Fig. 5.13 which is consistent with the one in Fig. 5.12 within the statistical errors .

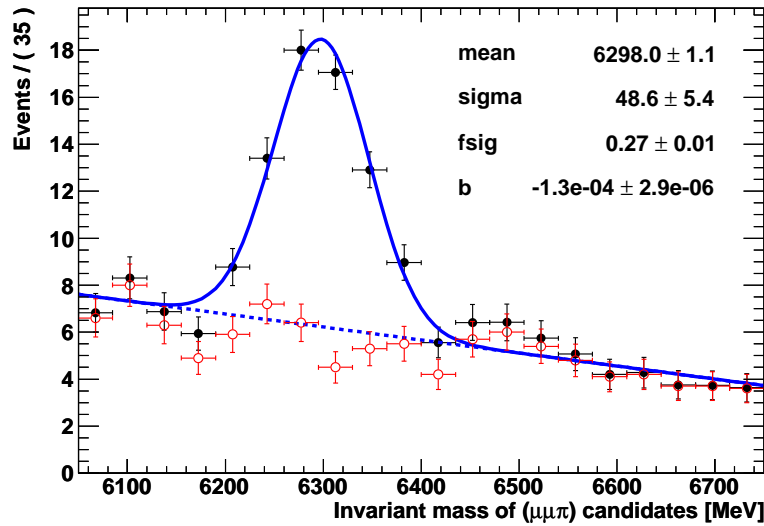


Figure 5.13: The invariant mass distribution of the reconstructed  $B_c$  signal and the toy Monte Carlo background ( $b\bar{b} \rightarrow J/\psi X$  and  $B_c \rightarrow J/\psi K$ , plotted with open circles). An unbinned maximum likelihood fit (solid line) was used to extract the reconstructed  $B_c$  mass and width. The dashed line is the projection for the background component of the same fit.

## 5.6 Statistical and systematic uncertainties

The uncertainty on the theoretical calculation of the  $b$ -production cross section at LHC energies is estimated to be a factor of two [37]. This uncertainty affects the signal and main backgrounds equally. According to the Poisson probability calculation, varying the

predicted signal and background values by a factor of 2 predicts a significance not less than  $4.1\sigma$ . The theoretical uncertainties on the branching ratios for  $B_c^\pm \rightarrow J/\psi\pi^\pm$  and  $B_c^\pm \rightarrow J/\psi K^\pm$  are both about 25% [37]. The Monte Carlo sample of the dominant background,  $b\bar{b} \rightarrow J/\psi X$ , includes 770,000 events. The statistical uncertainty due to the finite size of this sample is approximately 18%. This effect is estimated by propagating the statistical error from the available background statistics after all cuts have been applied up to  $1 \text{ fb}^{-1}$  of integrated luminosity. (Signal statistics are scaled accordingly.) We assume the statistical error will vary as  $\sqrt{B}$ , where  $B$  is the number of background events.

We have considered the following systematic uncertainties which are relevant to our study.

- Momentum scale

The momentum scale uncertainty will be calibrated with collision data on well-established particles, including  $J/\psi$ ,  $\psi'$ ,  $\Upsilon$ , and  $B^+$ . These masses span the scale over a wide kinematic region. As shown in Fig. 5.4(a) and Fig. 5.11, the  $J/\psi$  and  $B^+$  reconstructed from our simulated samples are identical with the PDG values within the statistical errors. The data projected for this analysis,  $1 \text{ fb}^{-1}$ , will include approximately 7 million  $J/\psi \rightarrow \mu^+\mu^-$  events from  $B$  decays. These will be sufficient statistics for ATLAS to calibrate the energy scale at the  $J/\psi$  mass. This will ensure that the uncertainty on the momentum scale will not dominate this measurement above  $1 \text{ fb}^{-1}$ .

- Misalignment

The measurement of the low- $p_T$  tracks in  $B_c$  events is determined by the inner detector (ID). The effect of misalignment in that subsystem upon  $B$ -physics events has been investigated for the decay  $B_d \rightarrow J/\psi K^{0*}$  [61]. The study was performed with the Day-100 random misalignment which represents the expected impact on tracking performance of the ID alignment on the 100th day of data taking. The study has shown that such misalignment will degrade mass resolution by 6% with no systematic shift in central value. We separately reconstructed  $J/\psi$  and  $B^+$  masses in the  $b\bar{b} \rightarrow J/\psi X$  sample using our selection requirements and the Day-100 alignment and found the results to be negligibly different from those reported in [61]. The  $J/\psi$  selection efficiency decreases by  $<1\%$  in the Day-100 alignment of the  $b\bar{b} \rightarrow J/\psi X$  sample.

- Charge asymmetric bias

We have compared reconstruction efficiencies for  $\pi^+$  and  $\pi^-$  tracks in the  $B_d \rightarrow J/\psi K^{0*}$  sample, with ideal alignment and Day-100 alignment. We find that there is no charge dependent bias on pion tracks associated with random misalignment, shown in Fig. 5.14.

Systematic uncertainties on trigger, reconstruction efficiencies, and acceptance are under study through the high statistics reference channel  $B \rightarrow J/\psi K$  and are expected to be a few percent [47]. The uncertainty on the LHC luminosity at  $1 \text{ fb}^{-1}$  of collected data will be evaluated during data collection.

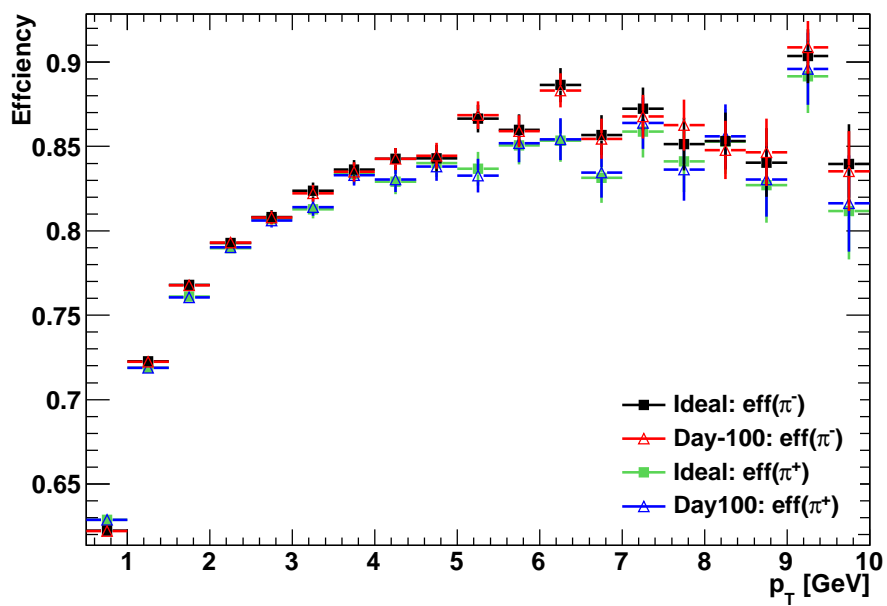


Figure 5.14: Reconstruction efficiencies of  $\pi^+$  and  $\pi^-$  in  $B_d \rightarrow J/\psi K^{0*}$  samples reconstructed with the ID ideal alignment and Day-100 random misalignment. Comparisons show that there is no charge dependent bias on the reconstruction efficiency in the Day-100 misalignment.



## 5.7 Summary and outlook

With  $1 \text{ fb}^{-1}$  of collected data and centre-of-mass energy 10 TeV, ATLAS expects to observe the  $B_c$  meson with a significance above 5.9 standard deviations. The cross section will increase as the energy rises to 14 TeV, so this is a worst case estimate. On the basis of the uncertainties and significance predicted here, we expect to surpass the current Tevatron sensitivity [55] with  $1.9 \text{ fb}^{-1}$  of data at the LHC.

Precision reconstruction of  $B_c$  excited states is our next target. The mass differences between the  $B_c$  ground and excited states can be used to constrain the shape of the strong potential. Theoretical predictions of the mass spectrum (Fig. 2.10 and Table 2.4) show that the mass difference between  $2S$  and  $1S$  states is  $\sim 600 \text{ MeV}$  which is above the detector resolution. It is therefore possible for ATLAS to observe this state and we foresee the possible channels are:

- $B_c(2^1S_0) \rightarrow B_c(1^1S_0)\pi^+\pi^-$
- $B_c(2^1S_1) \rightarrow B_c(1^1S_1)\pi^+\pi^-$ ,  $B_c(1^1S_1) \rightarrow B_c(1^1S_0) + \gamma$

where the  $B_c(1^1S_0)$  will be reconstructed through the hadronic decay  $B_c \rightarrow J/\psi \pi$  presented in this study.

Furthermore, the lifetime of  $B_c$  has been measured successfully from semileptonic decays in Tevatron but measurements from hadronic decays are still challenging due to the low branching ratios and large backgrounds. In ATLAS, we will also pursue the lifetime measurement through both decay modes. In particular, we expect to achieve the measurement through the  $B_c \rightarrow J/\psi \pi$  decay because of the high  $b$  quark production rate and the high luminosity of the LHC.

# Chapter 6

## Impact of the ID alignment on tracking and physics

### 6.1 Alignment of the ATLAS inner detector

The precision of the ATLAS tracking system is essential for many physics measurements, such as B physics where the low- $p_T$  muon tracking is particularly driven by the inner detector (ID) system. Systematic uncertainties from the ID alignment need to be considered in measurements of B masses and lifetimes. Therefore a lot of effort has gone into understanding the impact of the ID alignment on physics and is described in my document No.3 listed on Pg. ii. The methodology is about to be applied to data once sufficient statistics are achieved.

As described in Sec. 4.1, the ATLAS inner detector consists of two silicon subsystems, the pixel detector with 1744 silicon modules and the semiconductor tracker (SCT) with 4088 modules, complemented by the transition radiation tracker (TRT) which is made of straw drift tubes arranged in 176 modules. The accuracy of the inner detector tracking is limited by how precisely the positions and orientations of the ID sensor modules and wires are known. After the assembly of the inner detector, the position of the individual modules is known with an accuracy much worse than their intrinsic resolution. Therefore a track-based alignment procedure has to be applied to determine the absolute position of the devices. The requirement on the alignment quality is that the resolution of track parameters is to be degraded by no more than 20% regarding the intrinsic resolution [62]. This translates into a requirement on the position precision of the silicon pixel and strip modules to be respectively  $7 \mu\text{m}$  and  $12 \mu\text{m}$  in the sensitive  $R - \phi$  direction. In the  $z$  direction of silicon modules in the barrel, in the  $R$  direction in the end-cap regions, and for the TRT, the alignment precision is required to be of several tens of micrometers. In addition, the alignment should minimise the systematic effects which could bias the track-parameter determination.

Information on the alignment of the ID comes from: the metrology of individual modules at the time of reconstruction, the system tests of modules, surveys of the completed barrels and wheels (in particular from the X-ray survey) and the Frequency Scan Interferometry (FSI) [63] which measures a network of lengths *in situ* on the SCT. This information

will be used to provide a starting point for the offline track-based alignment.

### 6.1.1 Track-based alignment of the inner detector

The alignment is specified by a set of constants corresponding to 6 alignment degrees-of-freedom (DoF) for each individual module or assembly structure (barrel layer, end-cap disk, etc.): 3 translations  $T_x$ ,  $T_y$  and  $T_z$  of the centre of the module with respect to the nominal position, and 3 rotations  $R_x$ ,  $R_y$ ,  $R_z$  around the Cartesian axis with respect to the nominal axis orientation. This means that the silicon (SCT and Pixel) modules of the ID system have about 35000 DoF, thus posing a significant challenge for the alignment algorithms. Several track-based alignment algorithms have been implemented in the ATLAS software framework which determine alignment constants by minimising the track residuals, i.e., the distance between the hit position measured in the given detector module and the intersection of the extrapolated track with that module, as illustrated in Fig. 6.1. The

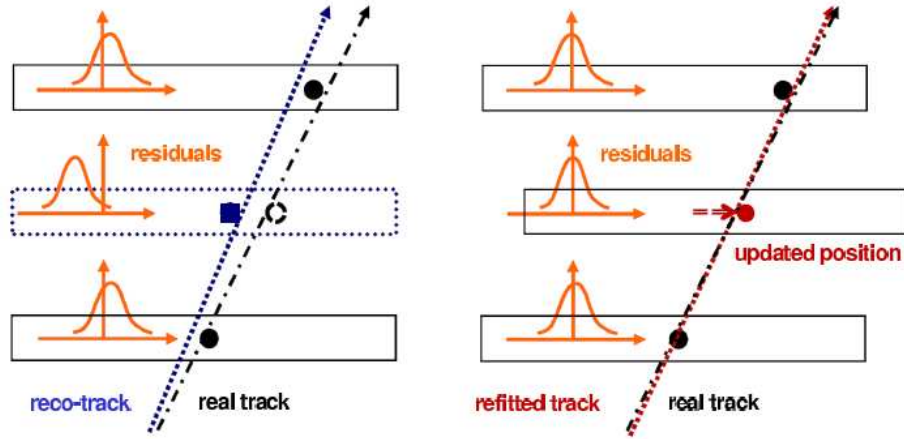


Figure 6.1: An example of the track fit with three silicon hits [64]. Assume the actual displacement of one module is unknown (left), the hit is reconstructed in a wrong place and the track fit is pulled. Consequently the residual distributions for all the modules are shifted from 0. The alignment procedure can iteratively adjust the position of the module until the residuals are minimised, thus improve the fit quality of the measured track.

procedure can be formulated as a  $\chi^2$  minimisation problem, with  $\chi^2$  defined as:

$$\chi^2 = \sum_{\text{tracks}} \mathbf{r}^T V^{-1} \mathbf{r} \quad (6.1)$$

where  $\mathbf{r}(\mathbf{a}, \tau)$  is a vector of the track-hit residuals for a given track depending on both the alignment constants,

$$\mathbf{a} = (T_x, T_y, T_z, R_x, R_y, R_z), \quad (6.2)$$

and the track perigee parameters of those modules with hits contributing to the track fit.

$$\tau = (d_0, z_0, \phi_0, \theta, q/p), \quad (6.3)$$

The matrix  $V$  represents the covariance matrix of the hit measurements composed of hit and tracking uncertainties, including the contribution from multiple Coulomb scattering. The minimisation is done simultaneously with respect to  $\tau$  and  $\mathbf{a}$  using the Global  $\chi^2$  algorithm [65]. The results can be cross-checked using two alternative algorithms: in the Local  $\chi^2$  algorithm [66, 67], the minimisation is accomplished only with respect to  $\mathbf{a}$ ; in the Robust algorithm [68] used only for silicon detectors, the alignment corrections are calculated directly from the size of the residual bias. In all cases, an iterative procedure is used. The alignment constants are then used in the track reconstruction to correct for misalignments.

The alignment procedure is done on several different levels of granularity. First, the largest structures are aligned, for which largest misalignments are expected and meanwhile the smallest statistics are needed. Afterwards, the alignment degrees-of-freedom are added depending on expected misalignments given by the construction, and the corresponding procedure is further broken down into several levels, as detailed for the silicon structures and the TRT structures in Tables 6.1 and 6.2. In general the reference frame for the alignment DoF ( $T_x, T_y, T_z, R_x, R_y, R_z$ ) at each alignment level is the local reference frame of the alignable structure, where  $T_x$  and  $T_y$  are in the plane of the structure and  $T_z$  is in the direction perpendicular to the plane. However, in the barrel structures  $T_x$  and  $T_y$  are in the plane transverse to the beampipe and  $T_z$  is parallel to the beampipe.

Level	Brief description	Structures	DoF
1	Whole Pixel detector (barrel and end-caps)	1	6
	SCT barrel and 2 end-caps	3	18
	Total:	4	24
2	Pixel barrel layers split into upper and lower halves	6	36
	Pixel end-caps disks ( $T_x, T_y$ and $R_z$ )	$2 \times 3$	18
	SCT barrel split into layers	4	24
	SCT end-caps split into disks ( $T_x, T_y$ and $R_z$ )	$2 \times 9$	54
	Total:	34	132
2.5	Pixel barrel layers split into staves	112	672
	Pixel end-cap disks ( $T_x, T_y$ and $R_z$ )	$2 \times 3$	18
	SCT barrel layers split into rows	176	1056
	SCT end-cap disks split into rings ( $T_x, T_y$ and $R_z$ )	$2 \times 22$	132
	Total:	338	1878
3	Pixel modules ( $T_x, T_y, T_z$ and $R_z$ )	1744	6976
	SCT modules ( $T_x, T_y, T_z$ and $R_z$ )	4088	16352
	Total:	5832	23328

Table 6.1: Alignment levels used with the combined alignment of cosmic-ray and collision data for the silicon sub-systems. Naming, brief description, number of structures and the total number of degrees-of-freedom (DoF) to be aligned at each level are given. The 6 DoF per structure are used, unless otherwise indicated [69].

Level	Brief description	Structures	DoF
1	TRT barrel (except $T_z$ ) and 2 end-caps	3	17
2	TRT barrel modules (except $T_z$ )	96	480
	TRT end-cap wheels (only $T_x$ , $T_y$ and $R_z$ )	$2 \times 40$	240
Total:		176	720

Table 6.2: Alignment levels used with the combined alignment of cosmic-ray and collision data for the TRT subsystem. Naming, brief description, number of structures and the total number of degrees-of-freedom (DoF) to be aligned at each level are given. The 6 DoF per structure are used, unless otherwise indicated [69].

### 6.1.2 Systematic misalignment

Despite the success of the alignment algorithms in minimising track residuals, residual misalignments can remain due to the statistical precision of the alignment constants and the systematic effects. The random misalignment can be resolved with large statistics and over a number of iterations in the alignment procedure. However, systematic misalignments of larger scale structure, such as rotations or translations of entire barrel layers or end-cap disks, have the potential to introduce systematic biases on the reconstructed track parameters. There exist a number of global systematic deformations that leave the tracking residuals and hence the fitted track's  $\chi^2/\text{DOF}$  unchanged. Such deformations are hard to be detected and removed by the Global  $\chi^2$  minimisation, and are therefore known as “weak modes”. Weak mode misalignments that remain in the ID clearly present a threat to the physics potential of the ID.

The parameterisation of the weak mode deformations were first proposed by the BaBar Collaboration [70] which were considered to be transformations of module global  $R$  (radius),  $\phi$  or  $Z$  coordinates ( $\Delta R$ ,  $\Delta\phi$ ,  $\Delta Z$ ) as a function of module  $R$ ,  $\phi$  or  $Z$ . Figure. 6.2 shows a  $3 \times 3$  grid to illustrate some potential weak mode deformations of the ID, and their potential impact on physics.

- $R\Delta R$  is an expansion or shrinking of module  $R$  coordinates, and similarly  $Z\Delta Z$  stretches modules along the beam pipe. Both deformations affect the absolute length measurement.
- $\phi\Delta R$  shapes the cross sections of modules elliptically, which influences an invariant mass measurement of particles coming from a common vertex.
- $\phi\Delta Z$  and  $Z\Delta R$  both mimic a change in the centre-of-mass energy.
- $R\Delta Z$  simulates a boost along the beam pipe.
- $R\Delta\phi$  is a radius dependent rotation of modules around the beam pipe which will produce a charge-dependent curvature bias and leads to charge-asymmetric biases in the momentum spectrum.
- $\phi\Delta\phi$  can create vertex displacements and fake secondary vertices.




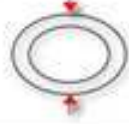


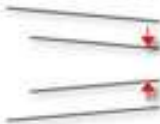
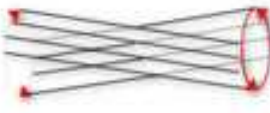
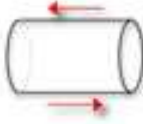
	$\Delta R$	$\Delta\phi$	$\Delta Z$
R	<b>Radial Expansion</b> (distance scale) 	<b>Curl</b> (Charge asymmetry) 	<b>Telescope</b> (COM boost) 
$\phi$	<b>Elliptical</b> (vertex mass) 	<b>Clamshell</b> (vertex displacement) 	<b>Skew</b> (COM energy) 
Z	<b>Bowing</b> (COM energy) 	<b>Twist</b> (CP violation) 	<b>Z expansion</b> (distance scale) 

Figure 6.2: Potential weak mode deformations of the inner detector [71].

- $Z\Delta\phi$  is a  $Z$ -dependent rotation of modules, thus can simulate a CP violation.

Unfortunately we can not know a priori to which weak modes we are susceptible or how large the deformation will be when running the alignment algorithm on actual ID geometry. However, in order to understand which weak modes have large impact on tracking and how to tackle and remove them, several weak mode misalignments have been created “by hand” and are considered to be most likely and dangerous: Curl ( $R\Delta\phi$ ), Twist ( $Z\Delta\phi$ ), Telescope ( $R\Delta Z$ ) and Elliptical ( $\phi\Delta Z$ ) [71]. Each deformation is simulated in two geometries differing in the magnitude of the misalignment; one geometry where the misalignments are very likely larger than in reality (labelled “XXXX-Large”), and another geometry of a size that is expected to remain as residual misalignment (labelled “XXXX-Residual”). These four deformations are parameterised to retain helical trajectories for particles coming from the interaction point as expected for a weak mode deformation and the actual terms introduced to distort the inner detector are specified below.

### Curl( $R\Delta\phi$ )

$$\Delta\phi = c_1 R + \frac{c_2}{R} \quad (6.4)$$

Two terms are introduced: one term proportional to the radial coordinate of the detector element, leading to a charge asymmetric bias in curvature and thus the reconstructed track momentum; one reciprocal term causing a  $\phi$  dependent shift of the reconstructed perigee positions and thus a possible performance loss in reconstructing primary and secondary vertices. To produce the Curl-Large geometry,  $c_1$  is chosen to be  $7.6 \times 10^{-4} \frac{\text{mrad}}{\text{mm}}$  such that modules in the outermost SCT barrel layer move by approximately  $200 \mu\text{m}$ , and  $c_2$  is  $50.0 \text{ mrad}\cdot\text{mm}$  such that pixel modules in the innermost barrel layer move by approximately  $50 \mu\text{m}$ . TRT barrel modules have a considerable length in the radial direction and therefore an additional rotation around a module’s centre is introduced to better simulate a true curling of the detector. The angle of the additional rotation is of the same magnitude as  $\Delta\phi$ .

### Twist( $R\Delta\phi$ )

$$\Delta\phi = cZ \quad (6.5)$$

The twist deformation is produced by rotating slices of the detector proportional to their  $Z$ -coordinate, thus changing curvature differently with respect to the track pseudorapidity. For the Twist-Large geometry, the value  $c = 2.5 \times 10^{-4} \frac{\text{mrad}}{\text{mm}}$  is chosen so that SCT barrel modules in the outermost  $\eta$  rings move by approximately  $200 \mu\text{m}$ . The TRT barrel modules do not have slices in  $R - \phi$ , so they are rotated by an angle  $\alpha$  around an axis in the  $R - \phi$  plane pointing radially outwards from the interaction point through the centre of the module.  $\alpha$  can be calculated as:

$$\alpha \approx -\frac{\phi_{\max}}{l/2} R \quad (6.6)$$

where  $\phi_{\max}$  is the  $\Delta\phi$  in the outermost SCT barrel  $\eta$  rings and  $l$  is the total length of the SCT barrel.

**Telescope**( $R\Delta\phi$ )

$$\Delta Z = cR \quad (6.7)$$

The telescope mode moves layers of modules along the beamline proportional to the radial coordinate. This creates an additional boost effect along  $z$  on the track parameters and therefore an  $\eta$  asymmetry. For the Telescope-Large geometry the value  $c = 5.8 \times 10^{-3}$  is chosen such that SCT modules in the outermost barrel layer move by approximately 3 mm. For the Telescope-Residual geometry the value  $c = 9.7 \times 10^{-4}$  is chosen so that SCT modules in the outermost barrel layer move by approximately 500  $\mu\text{m}$ .

**Elliptical**( $\phi\Delta R$ )

$$\Delta R = \frac{1}{2}c \cos(2\phi)R \quad (6.8)$$

This mode moves modules at the same distance from the beam line radially inwards and outwards as a circular wave which produces a  $\phi$  dependent change in the distance scales and should affect reconstructed vertex masses since angles between pairs of tracks are stretched or shrunk. The Elliptical-Large geometry is produced by applying  $c = 3.9 \times 10^{-3} \text{ mm}^{-1}$  so that SCT barrel modules on the outermost layer move outwards and inwards by up to 1 mm. For the Elliptical-Residual geometry the value  $c = 9.8 \times 10^{-4} \text{ mm}^{-1}$  is chosen such that SCT barrel modules on the outermost layer move outwards and inwards by up to 250  $\mu\text{m}$ . The TRT end-cap disks do not produce elliptical distortions due to the actual structure of the disks.

For the Curl and Twist deformations the alignment procedure was run on the Curl-Large and Twist-Large geometries described above to produce Curl-Residual and Twist-Residual geometries. Validation and the impact of these deformations have been stressed by both ATLAS alignment and physics groups [61, 71]. Studies of the impact of these deformations on resonances are presented in Sec. 6.2.

## 6.2 Impact of the ID alignment on resonances

Misalignments of the inner detector modules lead to biases in the measured track parameters and the vertex reconstruction, and consequently influence physics analyses at ATLAS. Various well-known resonances are good handles to evaluate the performance of the ID tracking in terms of alignment, material budget, magnetic field, etc. In ATLAS, we use decays of resonances,  $K_s^0 \rightarrow \pi^+\pi^-$ ,  $J/\psi \rightarrow \mu^+\mu^-$ ,  $\Upsilon \rightarrow \mu^+\mu^-$ ,  $Z^0 \rightarrow \mu^+\mu^-$ , and  $Z^0 \rightarrow e^+e^-$ , to assess the ID alignment and the overall tracking performance for physics. Masses and widths of these resonances reconstructed from the ID tracks are seen to be sensitive to the misalignment, particularly the systematic effect from weak modes. This section is focused on the impact of the ID alignment on these resonances. Studies have been done initially with simulated Monte Carlo samples, and the procedures have also been implemented in the ATLAS offline Data Quality Monitoring Framework (DQMF) [72] for assessing the ID alignment constants and track reconstruction (document No.3 from Pg. ii).



### 6.2.1 Resonances in the ATLAS offline data quality monitoring

The ATLAS Data Quality Monitoring Framework provides functionality for automated analyses of monitoring data (predominantly in the form of histograms) through user-defined algorithms. Offline monitoring applications from sub-systems are run during the prompt data processing at Tier-0 computer farm. A well-defined subset of the monitoring histograms, referred to as shift histograms, is displayed to the shifter together with the test results of the DQMF algorithms. The results are converted to a DQ status flag that can be either green (all is OK), yellow (expert intervention is needed) or red (data is seriously compromised and can not be used for physics analyses). Results from online and offline monitoring, and the detector control system are then combined to propose an overall DQ status. The shifter will decide the final DQ result and update the data quality database. The framework of the detector and data quality monitoring in the ATLAS experiment is shown in Fig. 6.3 in which our work contributes to the offline histograms and offline DQMF.

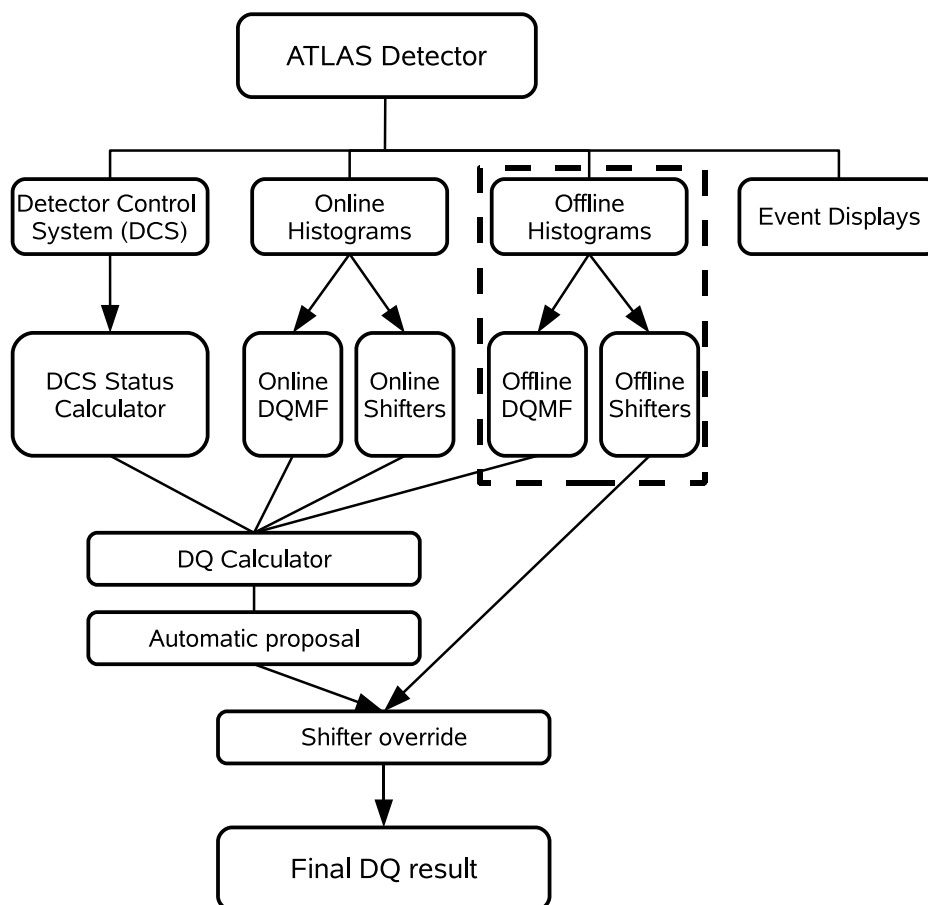


Figure 6.3: A flowchart illustrates the ATLAS data quality framework.

For the ID system, the `InDetAlignmentMonitoring` and `InDetPerformanceMonitoring` applications are implemented in the offline data processing to produce histograms of properties and residuals of individual tracks, the beam spot, as well as the resonances  $K_s^0 \rightarrow \pi^+\pi^-$ ,  $J/\psi \rightarrow \mu^+\mu^-$ ,  $\Upsilon \rightarrow \mu^+\mu^-$ ,  $Z^0 \rightarrow \mu^+\mu^-$ , and  $Z^0 \rightarrow e^+e^-$  (document No.3 from Pg. ii). The aim is to validate the alignment constants and evaluate the tracking performance. The `InDetPerformanceMonitoring` debuted at the Full Dress Rehearsal phase-2 (FDR-2, 2a, 2b, 2c) [73] in June 2008 when the full ATLAS data processing chain from the trigger subfarm output nodes (SFO's) to the physics analysis of the taken data was exercised. The data samples were simulated roughly equivalent to one day of data taking with a luminosity of  $10^{32} \text{ cm}^{-2}\text{s}^{-1}$  or  $10^{33} \text{ cm}^{-2}\text{s}^{-1}$ . A misaligned ID geometry [74] was used in the FDR-2 samples which was designed to be as close as possible to the real as-built experiment. The alignment production chain ran with the 24h loop of the ATLAS calibration chain and various alignment strategies were applied in the FDR-2 exercise in order to produce alignment constants for the event reconstruction within 24 hours after data taking [75]. The alignment constants, referred to as ‘‘FDR-alignments’’ were passed to the monitoring for validation and then applied to the final reconstruction of events. Meanwhile, the alignment constants that were produced in the CSC (Computing System Commissioning [47]) exercise, known as ‘‘CSC first-pass alignment’’ [74], were also applied to the FDR-2 misaligned samples to compare with the FDR-2 alignments. The performance of the FDR-2 alignments on resonances is shown in the following subsections.

### $J/\psi \rightarrow \mu^+\mu^-$ and $\Upsilon \rightarrow \mu^+\mu^-$

The heavy quarkonium production rate is expected to be so large that we can investigate the ID performance with sufficient statistics in the low  $p_T$  regime using the di-muon decays of  $J/\psi$  and  $\Upsilon$ . The cross sections of both decays before trigger efficiency are estimated to be tens of nanobarn in ATLAS. Since the natural widths of the mass peaks are small, the observed mass resolutions can reflect the degradation due to the tracking effect.

A few criteria were used to select  $J/\psi$  or  $\Upsilon$  candidates:

- Combined muons were retrieved and their associated inner detector tracks were taken as monitoring objects.
- All possible  $\mu^+\mu^-$  pairs passing the cut  $p_{T_{1,2}}(\mu) > 4 \text{ GeV}$  were formed.
- Di-muon pairs for which the invariant masses fell within a window of 2 GeV around the nominal  $J/\psi$  or  $\Upsilon$  mass were retained.

Some of the monitoring histograms from the FDR-2 and FDR-2c exercises are shown below. The  $J/\psi$  invariant mass distributions from different Express Stream<sup>I</sup> processings are presented in Fig. 6.4. The distribution from the stream aligned with the CSC first-pass constants is presented in Fig. 6.4(a) and the width of  $J/\psi$  was as good as expected. Meanwhile, several sets of alignment constants were derived containing different levels (already

---

<sup>I</sup>a data stream that contains about 10% of all events passing prescaled triggers. This is to ensure that the detector and reconstruction software perform as expected before the full dataset is processed.

described in Sec. 6.1). The alignment effects without L3 could be seen in Fig. 6.4(b) where the variation of width was much larger. After including L3 alignment the mass distribution was improved, seen in Fig.6.4(c), although still not comparable to the one from the CSC first-pass alignment. The degradation was due to a bug in the FDR-2 alignment which was already visible in the  $J/\psi$  mass shape. Figure 6.4(d) was produced later in FDR-2c with the alignment bug fixed so the width appeared to be recovered. The total number of observed signal events in each run was estimated according to the fit of the mass distribution. For one run of Express Stream at an integrated luminosity of  $36 \text{ nb}^{-1}$ , the monitoring module selected approximately 1000  $J/\psi \rightarrow \mu^+\mu^-$  events and the width of  $J/\psi$  mass peak has been seen sensitive to alignment changes.

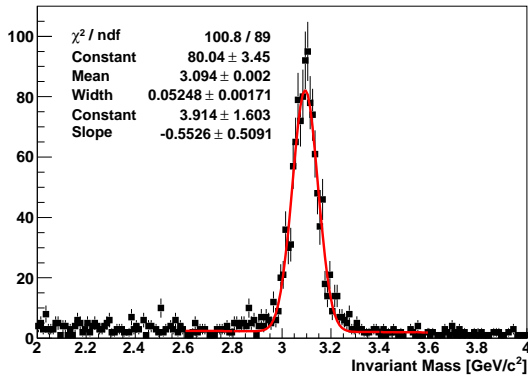
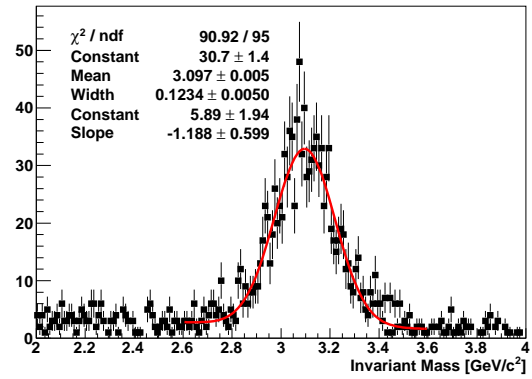
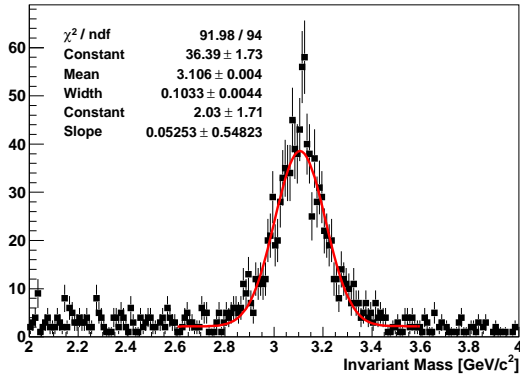
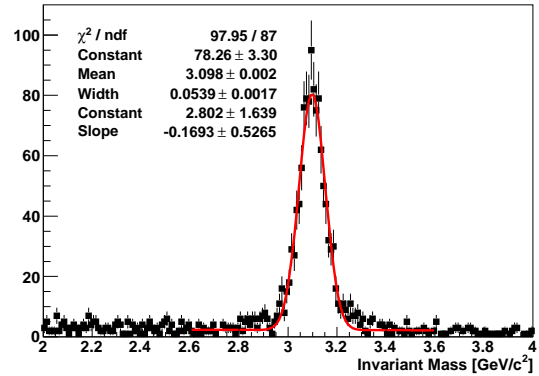
(a) CSC first-pass alignment,  $N(J/\psi)=1053$ (b) FDR-2 alignment without L3,  $N(J/\psi)=949$ (c) FDR-2 alignment including L3,  $N(J/\psi)=942$ (d) FDR-2c alignment,  $N(J/\psi)=1057$ 

Figure 6.4: Invariant mass distribution of di-muon (ID) tracks in different aligned Express Stream events during FDR-2 and FDR-2c, fit with a function of single gaussian combined with a first-order polynomial to separate the signal and the background. The total number of signal events,  $N(J/\psi)$ , is obtained by integrating the gaussian function over 2.6 GeV to 3.6 GeV.

$$K_s^0 \rightarrow \pi^+\pi^-$$

$K_s^0$  is a long-lived particle with the decay time around 90 ps. This translates into an average decay length of roughly 30 cm for a 5 GeV  $K_s^0$ , allowing radial tracking studies. In addition,  $K_s^0$  are copiously produced in most triggered physics processes, and have a much larger momentum transfer than other long-lived particles (such as  $\Lambda$ ) with a correspondingly larger sensitivity to reconstruction imperfection. The following selection criteria were used to select  $K_s^0 \rightarrow \pi^+\pi^-$  events:

- Tracks were required to have at least 3 SCT hits.
- Two oppositely signed tracks were fit to a common vertex with the vertex probability  $\geq 0.001\%$
- $400 \text{ MeV} < M_{\pi^+\pi^-} < 600 \text{ MeV}$
- Transverse decay length,  $L_{xy} > 12\text{mm}$
- Proper decay time,  $\tau > 4\text{ps}$
- Two-dimensional pointing angle between the decay-vertex vector with respect to the origin and  $K_s^0$  momentum vector,  $\cos\theta > 0.998$

Preliminary studies using the Monte Carlo minimum bias sample has shown that the mean and resolution of the invariant mass peak are sensitive to imperfections in the material parameterisation and alignment of the ID tracking. Figure. 6.5 shows the resolution of the peak versus  $\phi$  for several alignment algorithms used in the FDR-2 exercise. Figure. 6.6 shows the variation of the peak position versus decay radius, which is roughly correlated to extra material included in the simulation that was not included in the reconstruction. It is worth noting that the  $K_s^0$  decay products are in the low  $p_T$  region where the material effect is expected to be dominant. This can be a challenge to extract the alignment effect in the  $K_s^0$  events.

$$Z^0 \rightarrow \mu^+\mu^-$$

The  $Z^0 \rightarrow \mu^+\mu^-$  resonance is one of the standard handles in investigating the high  $p_T$  tracking capabilities of the ATLAS detector. A pure sample can be tagged independently of the ATLAS inner tracking system, with a reasonable efficiency. Given that  $Z^0 \rightarrow \mu^+\mu^-$  events are produced at a rate of 600 per  $\text{pb}^{-1}$  at 14 TeV, this provides a statistically powerful tool for checking the alignment of high  $p_T$  tracks. Since the results of the track fit procedure are strongly correlated with misalignments of the inner detector, kinematic biases will often result from any residual misalignments.

The  $Z^0 \rightarrow \mu^+\mu^-$  events were tagged in simulation using standard  $p_T$  and muon isolation cuts. These are detailed below:

- Two high- $p_T$  muon spectrometer tracks with:  
at least 12 MDT ( muon drift tube ) hits are required;

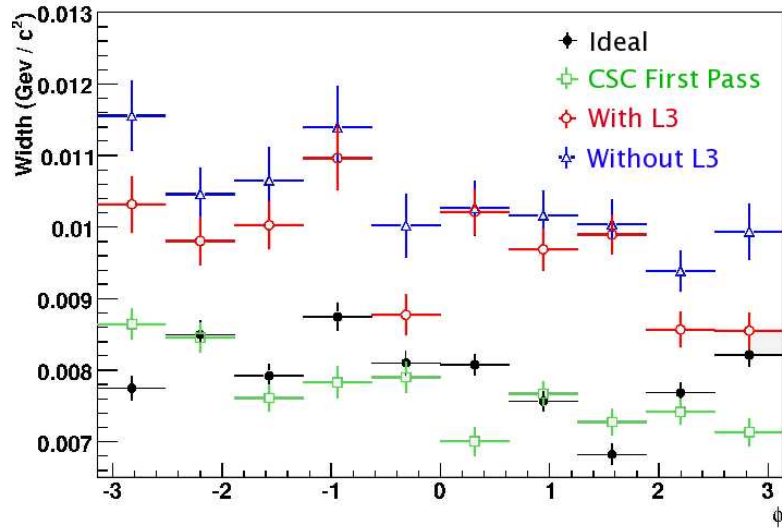


Figure 6.5: Width of the  $\pi^+\pi^-$  invariant mass peak versus  $\phi$  in simulated FDR-2 events for “ideal” (black filled circles), “CSC first-pass” (green open squares), FDR-2 “without L3” (blue open triangles), and FDR-2 “with L3” (red open circles) sets of alignment used in the ID reconstruction algorithm.

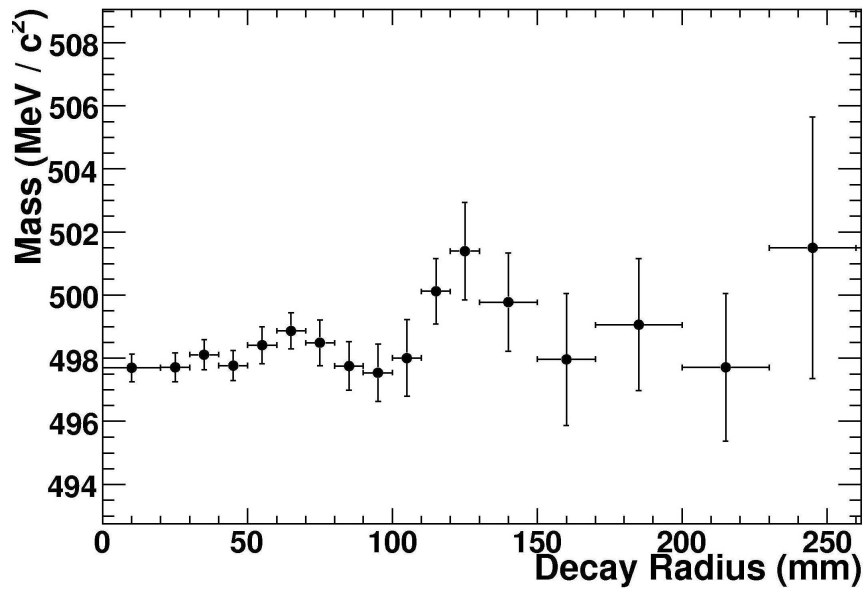


Figure 6.6: Position of the  $\pi^+\pi^-$  invariant mass peak versus decay radius in 20,000 simulated Monte Carlo events with ideal alignment applied. The sample used had extra material inserted in simulation, but not in reconstruction, at several radial positions.

spectrometer  $p_T > 20 \text{ GeV}/c$ , after calorimeter energy loss corrections applied; deposited transverse energy in a cone of  $\Delta R = 0.2$  around the muon candidate was less than 1 GeV.

- Required the invariant mass of the tracks to fall in the region 50 to 130 GeV/ $c^2$

These cuts gave an overall event tag efficiency of 32.5% for a well aligned sample (not including any efficiency loss due to event triggering).

Several graphs were identified as being particularly sensitive to misalignments and were considered as test cases for the ATLAS beam commissioning period. These graphs are detailed here:

- The invariant mass shift using inner detector tracks, which is plotted versus momentum difference,  $\eta(Z^0)$  and  $\phi(Z^0)$ .
- Momentum charge asymmetries plotted against momentum,  $\phi$  and track rapidities.
- Track matching efficiencies, between the inner detector and muon system, are plotted for both the full re-tracking and loose match case ( defined as the angular distance within  $\Delta R = 0.5$ ).
- The impact parameters for the inner detector tracks plotted against track  $\phi$  and  $\eta$  and  $p_T$ , done independently for positively and negatively charged tracks.

### Electrons from $Z^0 \rightarrow e^+e^-$ decays

A powerful quantity to reveal  $p_T$  biases is the  $E/p$  for electrons, since the measurement of the energy  $E$  in the calorimeter is insensitive to inner detector misalignments. To be less sensitive to the calorimeter calibration one can study the difference between the  $E/p$  for electrons and positrons.

The electron was selected as a calorimeter cluster matched to an inner detector track. The calorimeter clusters were required to pass all non-track based cuts included in the standard tight electron definition. The track matching algorithm required a track to be within 0.1 in  $\Delta\phi$  and within 0.05 in  $\Delta\eta$ . If there were multiple tracks present after the cuts, the track with the smallest  $\Delta R$  to the cluster will be chosen. There was no  $E/p$  cut imposed on the track matched to the cluster as this would bias the  $E/p$  distribution.

$Z^0 \rightarrow e^+e^-$  events were selected by requiring two electrons, passing the requirements listed above, and with calorimeter cluster  $p_T > 20 \text{ GeV}$ . In addition, the invariant mass of the two calorimeter clusters must be between 70 and 110 GeV. There was no cut imposed on the invariant mass of the two tracks. The overall efficiency of the  $Z^0 \rightarrow e^+e^-$  selection criteria was approximately 40%. Figure 6.7 shows the  $E/p$  distribution in simulated  $Z^0 \rightarrow e^+e^-$  events at different levels of alignment. The shape of the  $E/p$  distribution depends on several effects. The high tail is dominated by bremsstrahlung, which will lead to a lower measured track momentum. The size of this tail is very sensitive to the amount of material in the inner detector. Low  $E/p$  can either come from the measured track momentum being too large or the measured calorimeter energy being too low (or a combination of

the two). In the case of severe misalignments, the  $E/p$  distribution gets considerably wider, and the low  $E/p$  region is especially affected. Even for small misalignments, the  $E/p$  distribution is somewhat broader, which can be seen by the increase of electrons with  $E/p < 1$ . The ratio between the number of electrons with  $E/p$  between 0.7 and 1.0 and the number of electrons with  $E/p$  between 1.0 and 1.3 is therefore a powerful variable to reveal misalignments. Figure 6.8 shows this ratio as a function of the calorimeter cluster  $\eta$ . For the misaligned geometry the ratio is very large, due to many electrons having  $E/p < 1$ . The ratio for the aligned geometry is rather consistent with that for the ideal geometry except at small  $\eta$ , indicating that one of the two end-caps is not perfectly aligned.

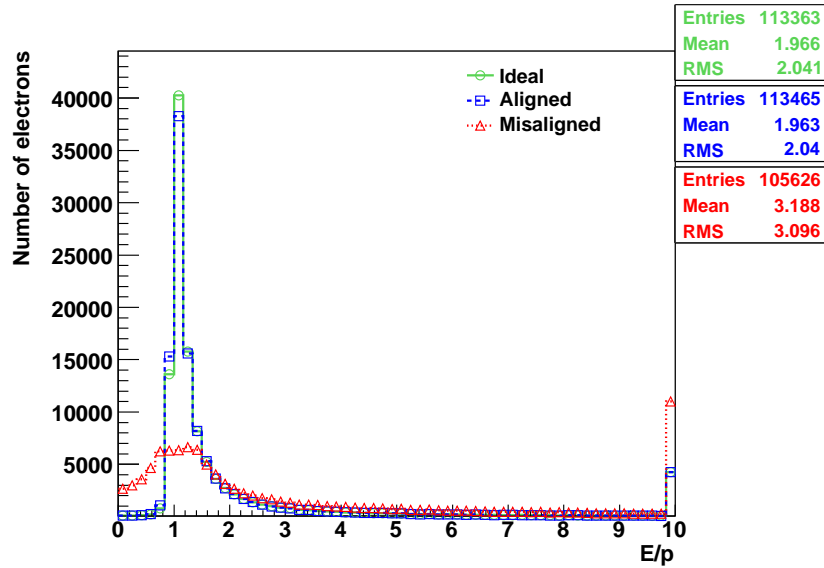


Figure 6.7: The  $E/p$  distribution for electrons in simulated  $Z^0 \rightarrow e^+e^-$  events, for ideal alignment (open circles), CSC misalignment (open triangles) and after running the alignment algorithms on the CSC misaligned geometry (open squares). In the presence of misalignments, there are more electrons with  $E/p < 1$ . The MC statistics used corresponds to approximately  $70 \text{ pb}^{-1}$  of  $Z^0 \rightarrow e^+e^-$  data.

The  $E/p$  distribution itself not only depends on the alignment of the inner detector, but also on the calibration of the calorimeter. In addition, it is not straightforward to derive from first principles what the  $E/p$  distribution should look like even for a perfectly aligned case. To be less sensitive to these effects, one can instead study the difference between the  $E/p$  distributions for electrons and positrons, since misalignments will often affect negatively and positively charged tracks differently. Figure 6.9 shows the difference between the average  $E/p$  for positrons and electrons as a function of the curvature of the track. The average of the  $E/p$  for positrons and electrons is only derived for electrons with  $E/p$  between 0.7 and 1.3. With ideal alignment the  $E/p$  is not dependent on the charge and the difference is zero. In both the misaligned and aligned case the difference is non-zero, indicating the presence of misalignments.

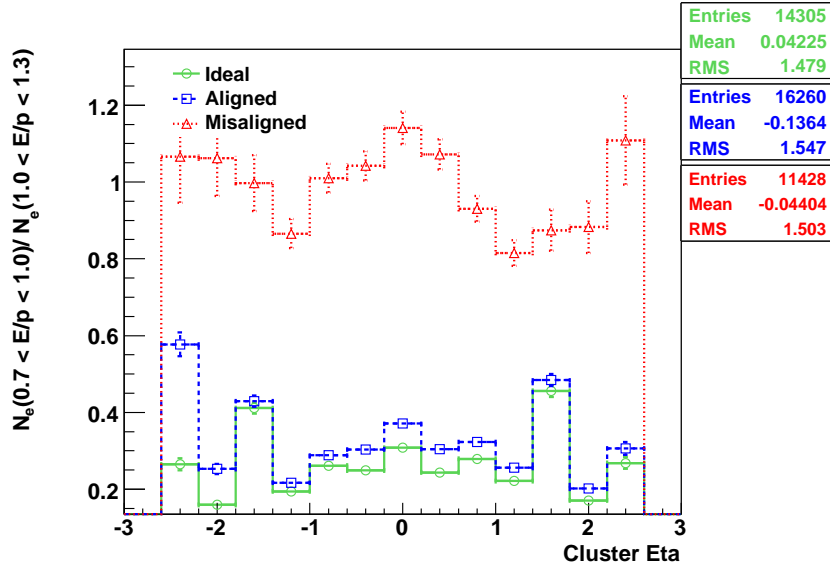


Figure 6.8: The ratio of the number of electrons with  $E/p$  between 0.7 and 1.0 and the number of electrons with  $E/p$  between 1.0 and 1.3, as a function of the calorimeter cluster  $\eta$ . The distribution is shown for ideal alignment (open circles), CSC misalignment (open triangles) and after running the alignment algorithms on the CSC misaligned geometry (open squares). The MC statistics used corresponds to approximately  $70 \text{ pb}^{-1}$  of  $Z^0 \rightarrow e^+e^-$  data.

## 6.2.2 Impact of weak mode misalignments on resonances

Sec. 6.1.2 has introduced four of the weak mode geometries in the inner detector that were created deliberately and considered to be most likely. We have investigated their impact on resonances using simulated Monte Carlo samples including:

- prompt  $J/\psi \rightarrow \mu^+\mu^-$  and  $\Upsilon \rightarrow \mu^+\mu^-$  events with Curl, Twist, and Elliptical deformations in the ID.
- $Z^0 \rightarrow \mu^+\mu^-$  events with Curl misaligned ID condition.
- $B_d^0 \rightarrow J/\psi K^{0*}$  with Telescope distortion in the ID and only the decay product  $J/\psi$  was used for our study.

Event selections were the same as described in the previous section, and the masses of the resonances were reconstructed from the ID track segments of the decay products. We have compared the peak positions of the resonances' mass distributions between two geometries for each deformation “XXXX-Large”<sup>II</sup> and “XXXX-Residual”, and also with results from the ideal alignment. The results show sensitivities to the weak mode deformations and the method will be applied to collision data to assist the detection and eventually elimination

<sup>II</sup>where XXXX stands for Curl, Twist, Elliptical or Telescope



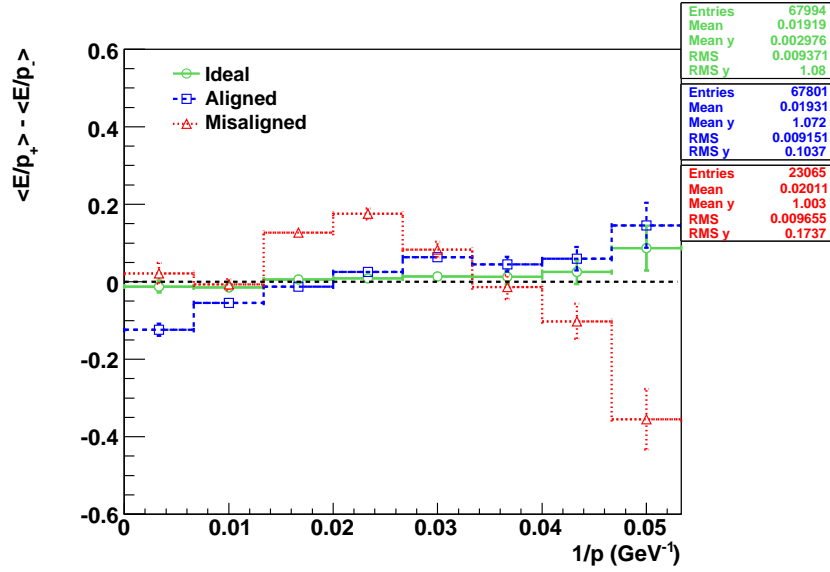


Figure 6.9: The difference between the average  $E/p$  for positrons and electrons as a function of the curvature of the track. The average  $E/p$  is only calculated for electrons and positrons with  $E/p$  between 0.7 and 1.3. The distribution is shown for ideal alignment (open circles), CSC misalignment (open triangles) and after running the alignment algorithms on the CSC misaligned geometry (open squares). The statistics used corresponds to approximately  $70 \text{ pb}^{-1}$  of  $Z^0 \rightarrow e^+e^-$  data.

of the systematic misalignments in the ID system. Studies of quantifying the systematic effect from the ID misalignment are ongoing.

### Curl

The Curl distortion mimics a rotation of the tracking module in the transverse plane causing a charge-dependent curvature bias (denoted as  $\delta$  with  $Q$  being the charge):

$$\frac{1}{p_T} \rightarrow \frac{1}{p_T} + Q \cdot \delta \quad (6.9)$$

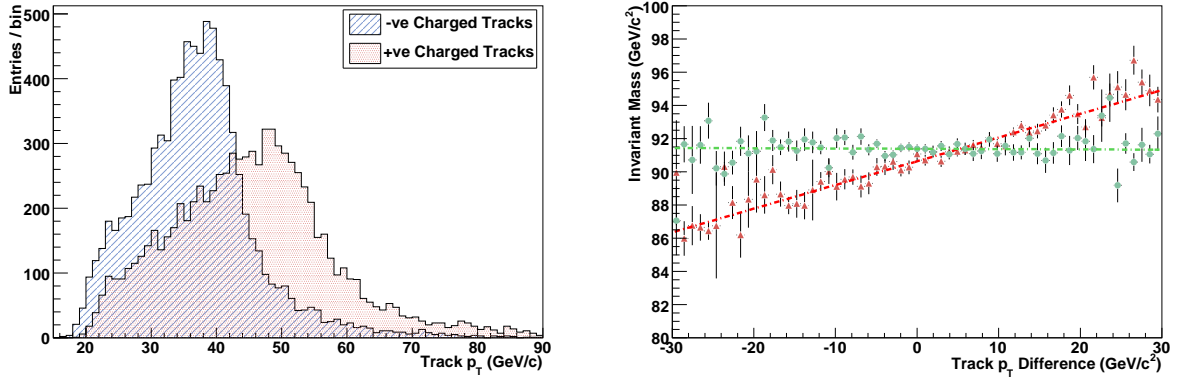
The track curvature bias produced by the Curl-Large misalignment can be seen in the  $Z^0$ ,  $J/\psi$  and  $\Upsilon$  events as shown in Figs. 6.10(a), 6.11(a) and 6.12(a). We see that the Curl-Large misalignment produces a bias in the curvature of  $\delta \sim -0.002 \text{ GeV}^{-1}$ . Using a linear approximation, the bias results in a change in the transverse momentum:

$$p_T \rightarrow p_T - Q \cdot \delta \cdot p_T^2 \quad (6.10)$$

For a resonance that decays into an oppositely charged track pair, the curvature bias can be translated to a variation of the invariant mass:

$$\begin{aligned}\Delta M &= \frac{1}{M} \left[ \frac{E_+}{E_-} p_{T-} \Delta(p_{T-}) + \frac{E_-}{E_+} p_{T+} \Delta(p_{T+}) - \cos(\phi_+ - \phi_-) \Delta(p_{T+} p_{T-}) \right] \\ &= \frac{\delta}{M} \left[ \frac{E_+}{E_-} p_{T-}^3 - \frac{E_-}{E_+} p_{T+}^3 - \cos(\phi_+ - \phi_-) p_{T+} p_{T-} (p_{T-} - p_{T+}) \right]\end{aligned}\quad (6.11)$$

The magnitude of the bias in mass depends on the momentum (or curvature) difference between the daughter tracks, clearly reflected in Figs. 6.10(b), Fig. 6.11(b) and Fig. 6.12(b).



(a) The  $p_T$  distributions for positive and negative inner detector tracks in the Curl-Large deformation.

(b) The mass of the  $Z^0$  resonance as a function of the difference between the momenta of the two tracks in the Curl-Large deformation.

Figure 6.10:  $Z^0 \rightarrow \mu^+ \mu^-$  events in the Curl-Large deformation.

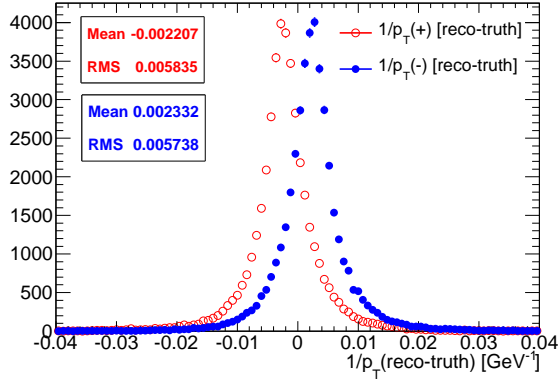
In addition, the curvature bias can lead to a charge asymmetry of the  $p_T$  distribution for the decay products, formulated as

$$\begin{aligned}f\left(\frac{1}{p_T}\right) &\rightarrow f\left(\frac{1}{p_T} + Q\delta\right) \simeq f\left(\frac{1}{p_T}\right) + f'\left(\frac{1}{p_T}\right)Q\delta \\ \text{Asym}\left(\frac{1}{p_T}\right) &= \frac{N_- - N_+}{N_- + N_+} = \frac{f(1/p_{T-} - \delta) - f(1/p_{T+} + \delta)}{f(1/p_{T-} - \delta) + f(1/p_{T+} + \delta)} = -\frac{f'}{f}\delta\end{aligned}\quad (6.12)$$

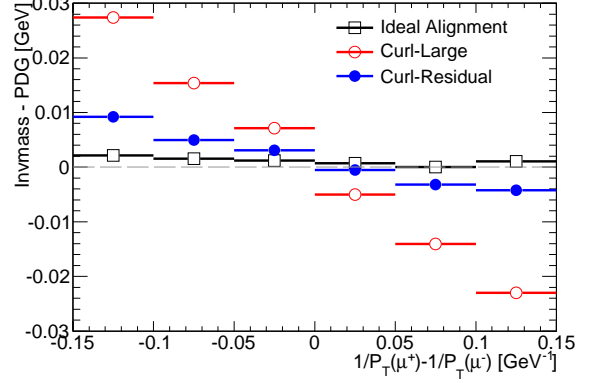
The distortion is shown in Fig. 6.13 for  $Z^0$  and  $J/\psi$  decays.

## Twist

The Twist weak mode rotates the detector proportional to the  $z$ -coordinate so it introduces an  $\eta$  dependent curvature bias. Like the Curl deformation (Eq. (6.10)), the Twist

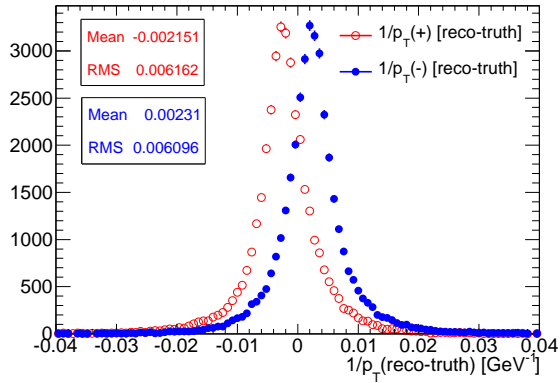


(a) The variation of the track curvature in the Curl-Large deformation with respect to the true value from the Monte Carlo sample. The mean values of the biases for positively and negatively charged tracks indicate that  $\delta \sim -0.002 \text{ GeV}^{-1}$ .

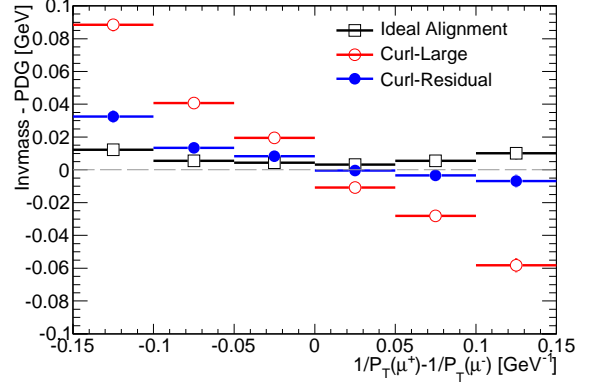


(b) Mass shift (w.r.t. the PDG value) of  $J/\psi$  as a function of the curvature difference between the two tracks in the Curl deformations.

Figure 6.11:  $J/\psi \rightarrow \mu^+ \mu^-$  events in the Curl mode.



(a) The variation of the track curvature in the Curl-Large deformation with respect to the true value from the Monte Carlo sample. The mean values indicate that  $\delta \sim -0.002 \text{ GeV}^{-1}$ , which is consistent with the result from  $J/\psi$  sample with the Curl-Large misalignment.



(b) Mass shift (w.r.t. the PDG value) of  $\Upsilon$  as a function of the curvature difference between the two tracks in the Curl deformations.

Figure 6.12:  $\Upsilon \rightarrow \mu^+ \mu^-$  events in the Curl mode.

deformation can be formulated as:

$$\begin{aligned}
 \frac{1}{p_T} &\rightarrow \frac{1}{p_T} + Q \cdot \delta \cot(\theta) \\
 &\rightarrow \frac{1}{p_T} + Q \cdot \delta \sinh(\eta) \\
 p_T &\rightarrow p_T - Q \cdot [\delta \cot(\theta)] \cdot p_T^2
 \end{aligned} \tag{6.13}$$

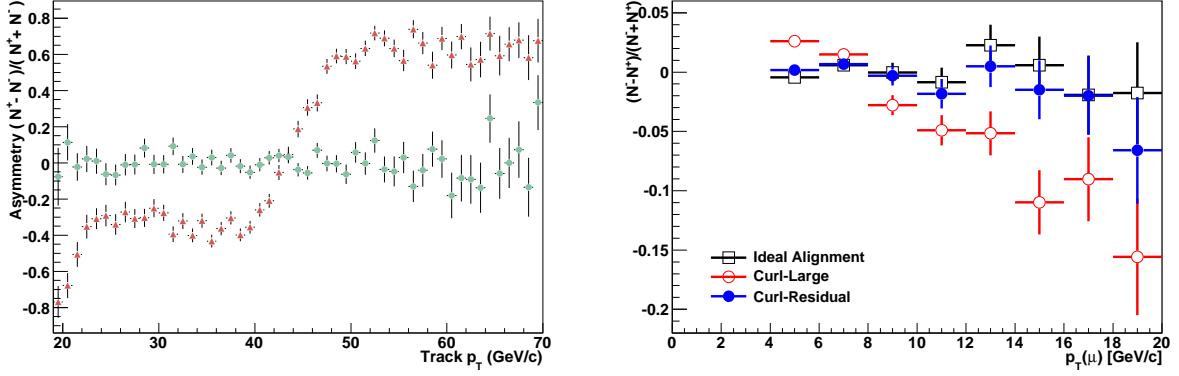


Figure 6.13: The charge asymmetry as a function of the track  $p_T$  in the  $Z^0 \rightarrow \mu^+\mu^-$  sample (left) between Curl-Large (triangles) and ideal alignment (filled circles); and in the  $J/\psi \rightarrow \mu^+\mu^-$  sample (right) where Curl-Large is compared to Curl-Residual and ideal alignment.

The bias in the transverse momentum produced by the Twist-Large misalignment is seen in Figs. 6.14(a) and 6.15(a). Accordingly, the change in the mass of resonance is foreseen to be correlated with the pseudorapidity difference (or  $\theta$  difference) between the daughter tracks,

$$\begin{aligned}
 \Delta M &= \frac{1}{M} \left[ \frac{E_+}{E_-} p_{T-} \Delta(p_{T-}) + \frac{E_-}{E_+} p_{T+} \Delta(p_{T+}) - \cos(\phi_+ - \phi_-) \Delta(p_{T+} p_{T-}) \right] \\
 &= \frac{\delta}{M} \left[ \frac{E_+}{E_-} p_{T-}^3 \cot(\theta_-) - \frac{E_-}{E_+} p_{T+}^3 \cot(\theta_+) \right] \\
 &\quad - \frac{\delta}{M} \left\{ \cos(\phi_+ - \phi_-) p_{T+} p_{T-} [p_{T-} \cot(\theta_-) - p_{T+} \cot(\theta_+)] \right\}
 \end{aligned} \tag{6.14}$$

which was seen in both  $J/\psi$  and  $\Upsilon$  decays, as shown in Figs. 6.14(b) and 6.15(b).

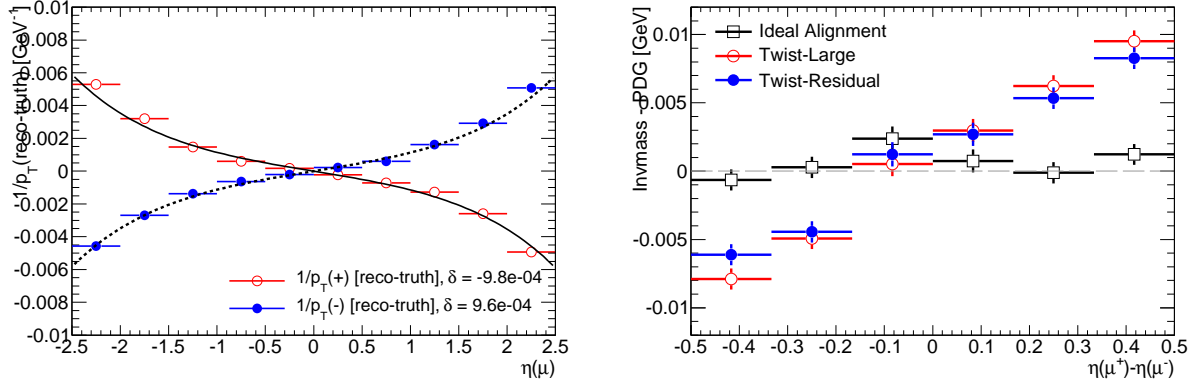
### Telescope

The Telescope mode causes a boost effect in the  $z$  direction that is equivalent to a bias in  $\theta$ , as shown in Fig. 6.16(a).

$$\begin{aligned}
 \cot(\theta) &\rightarrow \cot(\theta) + \delta \\
 p_z = p_T \cot(\theta) &\rightarrow p_z + p_T \cdot \delta
 \end{aligned} \tag{6.15}$$

so that

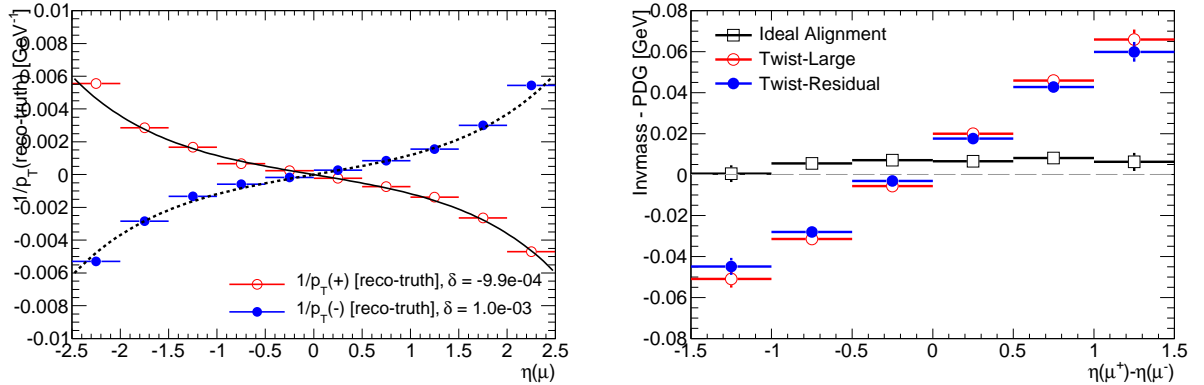
$$\begin{aligned}
 \Delta M &= \frac{1}{M} \left[ \frac{E_+}{E_-} p_{z-} \Delta(p_{z-}) + \frac{E_-}{E_+} p_{z+} \Delta(p_{z+}) - \Delta(p_{z+} p_{z-}) \right] \\
 &= \frac{\delta}{M} \left[ \frac{E_+}{E_-} p_{T-}^2 \cot(\theta_-) + \frac{E_-}{E_+} p_{T+}^2 \cot(\theta_+) - p_{T+} p_{T-} (\cot(\theta_+) + \cot(\theta_-)) \right]
 \end{aligned} \tag{6.16}$$



(a) The variation of track curvature (w.r.t the Monte Carlo truth) as a function of  $\eta$  in the Twist-Large mode. The curves for positively and negatively charged tracks were modelled by a hyperbolic sine function, show that  $\delta \sim -0.001 \text{ GeV}^{-1}$ .

(b) The variation of the resonance mass w.r.t. the PDG value as a function of  $\eta$  difference of the tracks in the Twist misaligned  $J/\psi \rightarrow \mu^+ \mu^-$  samples.

Figure 6.14:  $J/\psi \rightarrow \mu^+ \mu^-$  events in the Twist mode.



(a) The variation of track curvature (w.r.t the Monte Carlo truth) as a function of  $\eta$  in the Twist-Large mode. The curves for positively and negatively charged tracks were modelled by a hyperbolic sine function, show that  $\delta \sim -0.001 \text{ GeV}^{-1}$ , which is consistent with the one  $J/\psi$  events.

(b) The variation of the resonance mass w.r.t. the PDG value as a function of  $\eta$  difference of the tracks in the Twist misaligned  $\Upsilon \rightarrow \mu^+ \mu^-$  samples.

Figure 6.15:  $\Upsilon \rightarrow \mu^+ \mu^-$  events in the Twist mode.

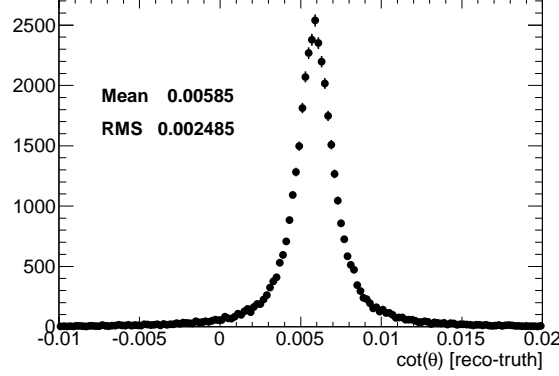
The expression can be simplified if we assume

$$\frac{E_+}{E_-} = \frac{p_+}{p_-} = \frac{p_{T+} \sin(\theta_-)}{p_{T-} \sin(\theta_+)} \quad (6.17)$$

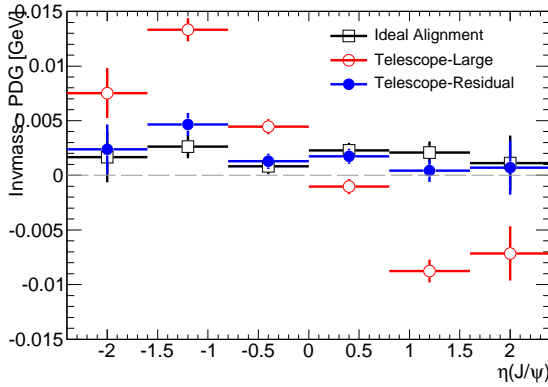
so that

$$\Delta M = -\frac{2\delta}{M} p_+ p_- \sin^2 \left( \frac{\theta_+ - \theta_-}{2} \right) \sin(\theta_+ + \theta_-) \quad (6.18)$$

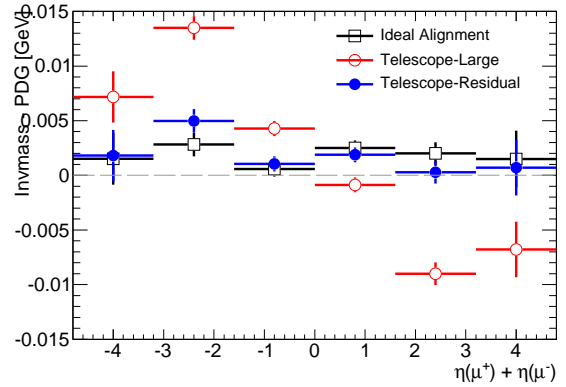
The characteristic distortion can be spotted by the variation of the resonance's mass on its pseudorapidity or the sum of the pseudorapidities of the decay products (Fig. 6.16).



(a)  $\cot(\theta)$  bias w.r.t the Monte Carlo truth in the Telescope-Large misalignment.



(b) The mass shift of  $J/\psi$  (w.r.t. the PDG value) as a function of its  $\eta$ .



(c) The mass shift of  $J/\psi$  (w.r.t. the PDG value) as a function of the sum of the  $\eta$ 's of the  $\mu$  tracks.

Figure 6.16:  $J/\psi \rightarrow \mu^+ \mu^-$  events in the Telescope mode.

## Elliptical

The modelling of the Elliptical deformation in the prompt  $J/\psi \rightarrow \mu^+ \mu^-$  samples is given by Eq. (6.8). This weak mode moves modules radially as a function of  $\cos(2\phi)$ , giving a bias in the track momentum, shown in Fig. 6.17(a)

$$\begin{aligned} R &\rightarrow R + R \cdot \delta \cdot \cos(2\phi) \\ p_T &\rightarrow p_T + p_T \cdot \delta \cdot \cos(2\phi) \end{aligned} \quad (6.19)$$

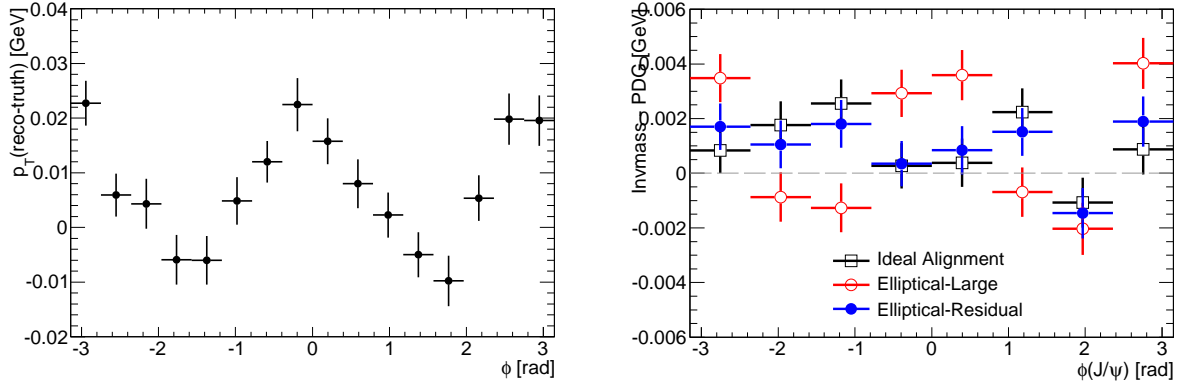
and affects the reconstructed mass, such as

$$\begin{aligned}\Delta M &= \frac{\delta}{M} \left[ \frac{E_+}{E_-} p_{T-} \Delta(p_{T-}) + \frac{E_-}{E_+} p_{T+} \Delta(p_{T+}) - \cos(\phi_+ - \phi_-) \Delta(p_{T+} p_{T-}) \right] \\ &= \frac{\delta}{M} \left[ \frac{E_+}{E_-} p_{T-}^2 \cos(2\phi_-) + \frac{E_-}{E_+} p_{T+}^2 \cos(2\phi_+) - 2p_{T+} p_{T-} \cos^2(\phi_+ - \phi_-) \cos(\phi_+ + \phi_-) \right]\end{aligned}\quad (6.20)$$

Using the same approximation as in Eq. (6.17), the bias in the mass can be simplified as

$$\Delta M \sim \frac{2\delta}{M} p_{T+} p_{T-} \cos(\phi_+ + \phi_-) \cos(\phi_+ - \phi_-) [1 - \cos(\phi_+ - \phi_-)] \quad (6.21)$$

The  $\cos(2\phi)$  dependence is reflected in Fig. 6.17(b). However, the magnitude of the bias in the mass caused by this weak mode is so small that it is hard to tackle in reality for this particular assumption of the Elliptical mode. More studies will be needed for a better understanding of this deformation.



(a) The variation of  $p_T$  (w.r.t the Monte Carlo truth) as a function of track  $\phi$  in the Elliptical-Large misalignment.

(b) The mass shift of  $J/\psi$  (w.r.t. the PDG value) as a function of its  $\eta$ .

Figure 6.17:  $J/\psi \rightarrow \mu^+ \mu^-$  events in the Elliptical mode.

## 6.3 Alignment performance in 7 TeV $pp$ collisions at the LHC

Before the start up of the LHC in October 2009, the preliminary ID alignment was determined using the cosmic-ray data collected during 2008 [76]. The data sample consisted of 420,000 tracks crossing the three ID sub-detectors (Pixel, SCT and TRT) recorded in two main configurations: with and without the solenoid field. Because cosmic rays only come from above the ATLAS detector, more hits were recorded in silicon modules in the top and bottom quadrants of the barrel than the side quadrants or the end-caps. In addition, the large incidence angles in the side and end-cap modules lead to poor resolution due to large or fragmented clusters. This limits the precision to which these regions of the Pixel and SCT detectors can be aligned. Due to the structure and larger acceptance, the TRT is less sensitive to this anisotropy and its alignment precision was more uniform. The set of alignment constants obtained with the cosmic-ray data is referred to as *Pre-Collisions Alignment*.

The *Pre-Collisions Alignment* was used to reconstruct the first LHC collisions in December 2009. With increasing collision data statistics, the alignment of the end-caps of the ID needed to be improved, as expected due to the poor illumination of the end-caps with cosmic rays. The alignment with the December 2009 900 GeV collision data followed the same scheme of alignment levels as the cosmic-ray data alignment. The alignment was done using both 2009 cosmic-ray data and the collision data simultaneously in order to maximise the hit-on-track statistics and also take advantage of two track topologies to reduce the sensitivity to weak modes. The 2009 cosmic-ray data sample consisted of 460,000 tracks crossing the three sub-detectors. For the collision data, runs with the three sub-detectors fully operational were used, equivalent to 360,000 events. The alignment constants produced is used for the current track reconstruction for 7 TeV collisions, labelled as *Post-Collisions Alignment*.

### 6.3.1 Alignment performance on tracks in 7 TeV $pp$ collisions

The quality and performance of the ID *Pre-Collisions Alignment* and *Post-Collisions Alignment* have been demonstrated using tracks reconstructed in proton-proton collisions at  $\sqrt{s} = 7$  TeV collected by ATLAS in 2010 [69]. The data sample analysed comprises 1 million events collected using the ATLAS minimum bias trigger from a single run taken on April 23rd, reconstructed using the *Pre-Collisions Alignment*, and later re-processed with the *Post-Collisions Alignment* in May. The different alignment constants applied to the same data sample were compared in order to illustrate the improvement in the understanding of the ID alignment. The  $\sqrt{s} = 7$  TeV collision results were compared to a minimum bias non-diffractive Monte Carlo sample generated using PYTHIA [57]. These Monte Carlo events have been simulated with a perfectly aligned ID module configuration and reconstructed in a setup identical to the one used for data. Below, the Monte Carlo distributions are normalised to the number of entries in the data distributions and the tracks are required to pass the following selection criteria:



- Track  $p_T > 2$  GeV
- Number of (SCT + Pixel) hits  $\geq 6$

The residuals obtained for modules in the Pixel, SCT and TRT detector were calculated by re-fitting the track with the hit-on-track under study removed and are shown in Figs 6.18, 6.19, 6.20 and 6.21. Figure 6.18 shows the local  $x$  residual distribution integrated over all hits-on-tracks in Pixel barrel modules and end-cap modules, and Fig. 6.19 shows the local  $y$  residual distributions for Pixel barrel and end-cap modules. Figure 6.20 is the local  $x$  residual distribution for SCT barrel and end-cap modules. Figure 6.21 shows the residual distributions for TRT barrel and end-caps. In each figure, the full width at half maximum (FWHM) of each distribution, divided by a factor of 2.35 is shown, which is equivalent to the width  $\sigma$  in a Gaussian distribution ( $\sigma = \text{FWHM}/2.35$ ). In general the width of the residual distributions is reduced using *Post-Collisions Alignment* compared with *Pre-Collisions Alignment* which demonstrates a significant improvement in the ID alignment after collision tracks have been used. In particular, a dramatic improvement in the width is observed for the SCT end-cap residual distribution (Fig. 6.20) which is likely due to the enhanced illumination of end-cap modules by collision tracks. The widths of the *Post-Collisions Alignment* residual distributions are approaching the widths observed in perfectly aligned Monte Carlo sample, indicating that the alignment is already of reasonable quality. If we assume that the existing difference of the residual width between data and Monte Carlo is caused by the effect of residual random misalignments of the ID modules, then we can estimate the size of the residual misalignments to be  $\sim 17 \mu\text{m}$  in the Pixel barrel and  $\sim 25 \mu\text{m}$  in the SCT barrel. The excellent agreement between the data and Monte Carlo residual distributions in the TRT barrel indicates that remaining residual misalignments are negligible compared to the intrinsic resolution.

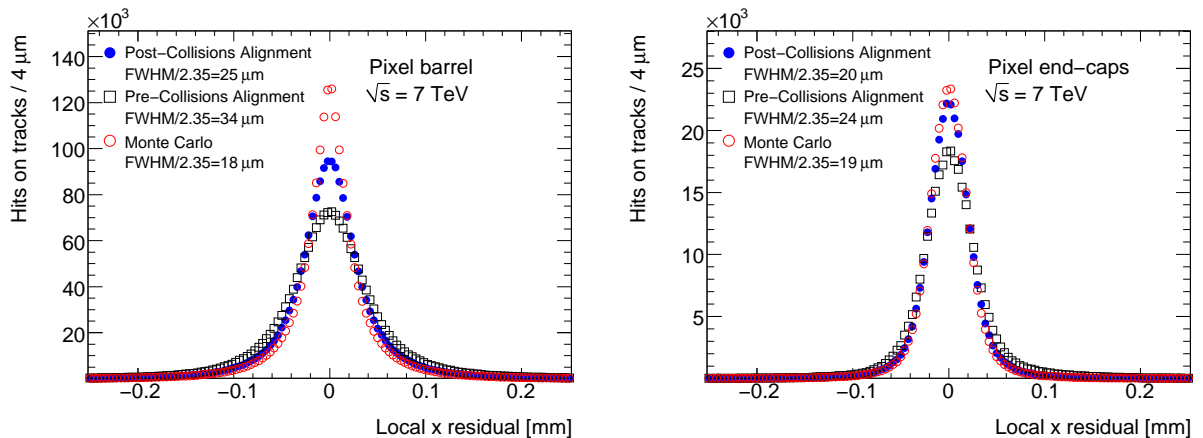


Figure 6.18: Pixel local  $x$  residual distributions integrated over all hits-on-tracks in barrel modules (left) and end-cap modules (right).

Figure 6.22 shows the quality of the impact parameter ( $d_0$ ) reconstruction using the *Post-* and *Pre-* *Collisions Alignment*. Shown is the mean transverse impact parameter, relative to the determined beamspot position for the run, as a function of track azimuthal

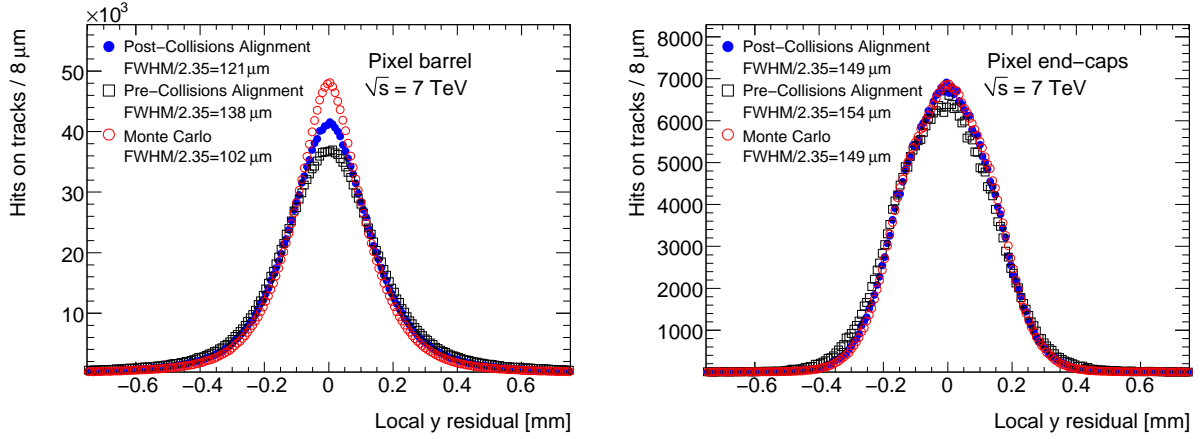


Figure 6.19: Pixel local  $y$  residual distributions integrated over all hits-on-tracks in barrel modules (left) and end-cap modules (right).

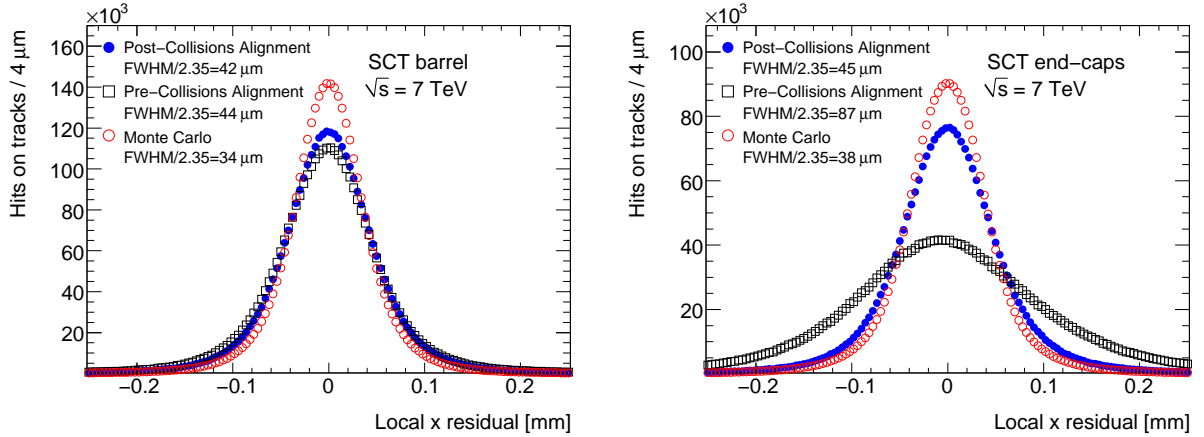


Figure 6.20: SCT local  $x$  residual distributions integrated over all hits-on-tracks in barrel modules (left) and end-cap modules (right).

angle  $\phi$  and track pseudo-rapidity  $\eta$ . Deviations of  $\sim 10 \mu\text{m}$  can still be seen in one of the end-cap regions at large negative  $\eta$ . The Monte Carlo distributions shows for a perfectly aligned detector the mean  $d_0$  is expected to be close to zero as a function of track  $\eta$  and  $\phi$ . The *Post-Collisions Alignment* again shows considerable improvement over the *Pre-Collisions Alignment*, with much reduced bias in the impact parameter observed.

In summary, the alignment constants obtained with the cosmic-ray data served to reconstruct the first period of LHC collision data in ATLAS. Later the use of 900 GeV collision data improved the ID alignment, especially in the end-cap regions. The results with the 7 TeV data collected during 2010 show that the current alignment precision is about  $17 \mu\text{m}$  for the Pixel barrel and  $25 \mu\text{m}$  for the SCT barrel modules. In the near future, the alignment of the ATLAS inner detector with the 7 TeV data will be performed, and the increased number of high momentum tracks should ensure a further improvement of the alignment.

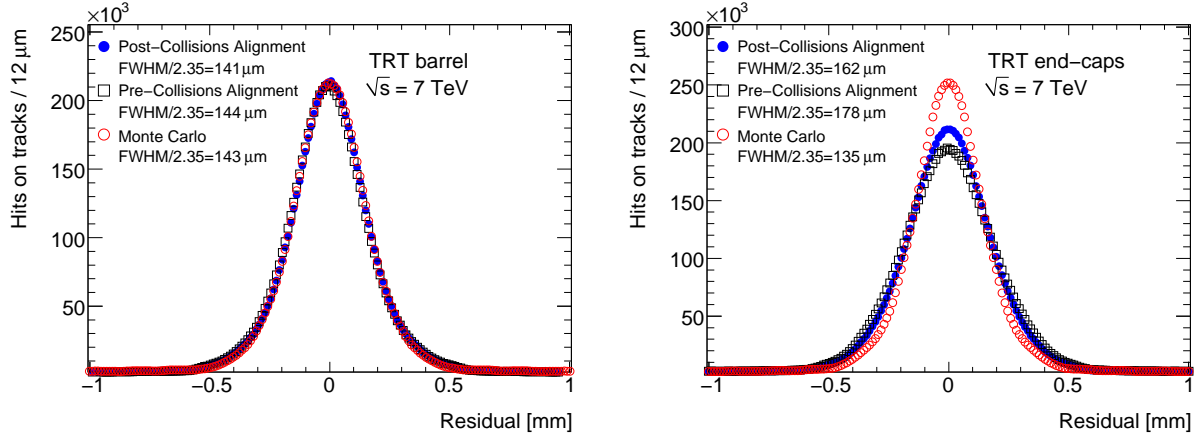


Figure 6.21: TRT residual distributions integrated over all hits-on-tracks in barrel modules (left) and end-cap modules (right).

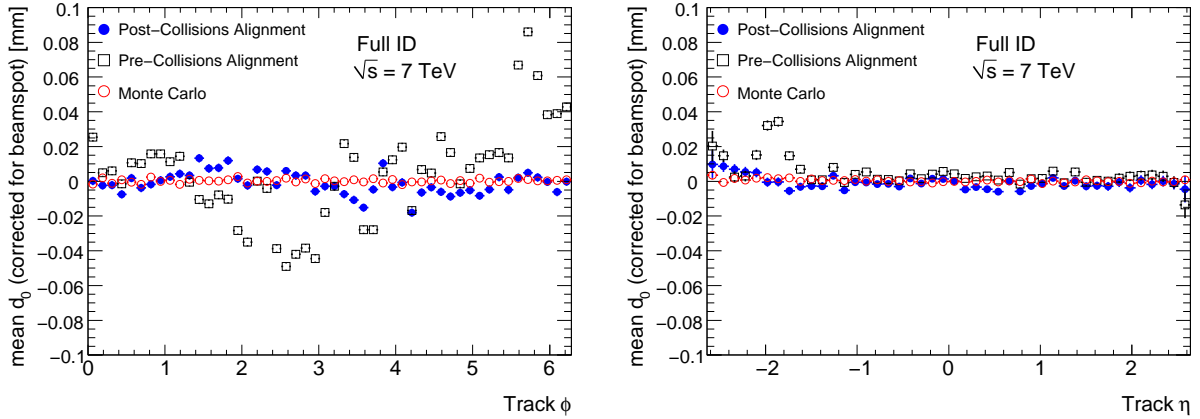


Figure 6.22: Mean transverse impact parameter (beam-spot corrected) as a function of track  $\phi$  (left) and track  $\eta$  (right).

### 6.3.2 Alignment performance in $K_s^0 \rightarrow \pi^+\pi^-$ events at 7 TeV

As shown, the *Post-Collisions alignment* obtained with 900 GeV data and cosmic-ray data simultaneously has improved the ID track residuals, particularly in the end-cap regions. Meanwhile, the performance of the two different alignments has also been investigated, using  $K_s^0 \rightarrow \pi^+\pi^-$  events, due to its large statistics available in collision data. This part will concentrate on such  $K_s^0$  decays reconstructed with *Pre-Collisions alignment* and *Post-Collisions alignment*. However, since the momenta of the decay products are low, material interaction is expected to dominate the measurement [77]. The impact of alignment will become more significant on  $J/\psi$ ,  $\Upsilon$ , and  $Z^0$  when the statistics allow for detailed studies. Eventually we will be able to understand the systematic effects in different momentum regions from these resonances.

In connection with the results of alignment performance based on tracks, we investigate

the  $K_s^0$  performance using the same data sample collected by the ATLAS minimum bias trigger, corresponding to  $666 \mu\text{b}^{-1}$  of integrated luminosity. The same minimum bias Monte Carlo sample is also used here for comparisons. The offline selection criteria follow the  $K_s^0$  analysis study in Ref. [78] but some of the selection cuts are adjusted in order to adapt the alignment requirement, given as follows:

- Two oppositely charged inner detector tracks with  $p_T > 500$  MeV and at least 6 silicon (Pixel + SCT) hits are allowed to form pairs.
- Tracks are fitted to a common vertex and the  $\chi^2$  of the vertex fit is required to be less than 15.
- The transverse flight distance between the primary vertex and the secondary vertex ( $K_s^0$  decay point), defined as  $L_{xy} = [(x_{SV} - x_{PV})p_x + (y_{SV} - y_{PV})p_y]/p_T$ , is required to be at least 4 mm.
- The pointing angle, defined by the angle in the transverse plane between the  $K_s^0$  momentum vector and the vector from the primary vertex to the decay vertex, is required to be as small as  $\cos(\theta) > 0.999$ .

Given the long decay length of  $K_s^0$ , after the event selections the tracks originated from  $K_s^0$  decays are refitted with respect to the decay vertices. This is to provide precise track parameters since the original measurements are derived from the primary vertices.

The distributions of the invariant mass of  $K_s^0$  candidates reconstructed with the *Pre-Collisions Alignment* and *Post-Collisions Alignment* in data, and the distribution from the ideally aligned Monte Carlo simulation are shown in Fig. 6.23. The distribution of truth matched signal and background candidates in the simulated sample have been normalised separately to match the different signal-to-background ratio in data. The fit overlaid on each histogram is modelled by the sum of two Gaussians for the signal and a third-order polynomial for the combinatorial background. The mean of the two Gaussian components are constrained to be the same in the fit, and the width is quoted as  $\sigma = \text{FWHM}/2.35$ . The mean values and the widths of the mass peaks in the data are stable despite the different alignment constants and both are in agreement with the result from the Monte Carlo sample, as shown in Table 6.3.

$K_s^0$ Data	Mean [MeV]	Width [MeV]
<i>Pre-Collisions Alignment</i>	$497.80 \pm 0.01$	6.20
<i>Post-Collisions Alignment</i>	$497.93 \pm 0.01$	6.18
Monte Carlo	$497.90 \pm 0.01$	5.74

Table 6.3: The results of the mean and the full width at half maximum divided by 2.35 of the signal peak from the fit to the data and the Monte Carlo sample. Uncertainties shown here are statistical only.

Figure 6.24 shows the deviation of  $K_s^0$  mass from its nominal position (the PDG value  $497.648$  MeV [2]) with respect to the difference of the curvatures ( $1/p_T$ ) between the

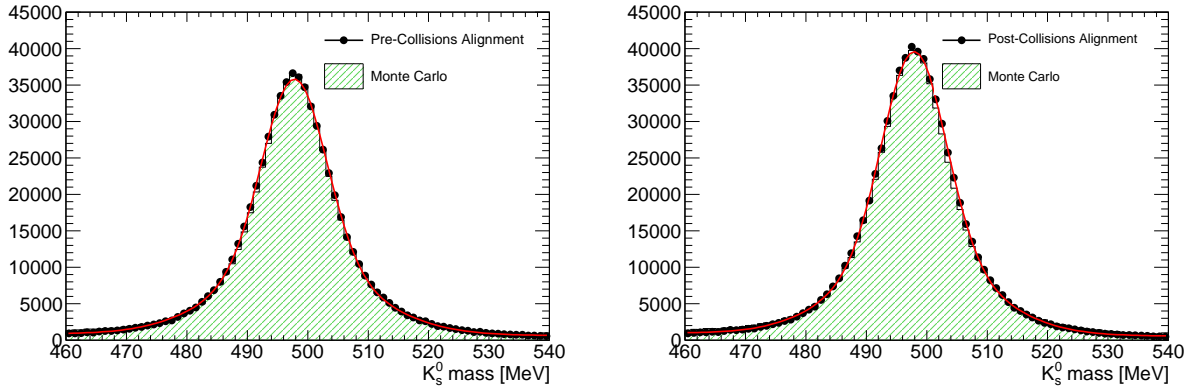


Figure 6.23: Invariant mass of  $K_s^0$  from the ATLAS minimum bias stream reconstructed with *Pre-Collisions alignment* (left), *Post-Collisions alignment* (right) and compared with the non-diffractive minimum bias Monte Carlo sample.

daughter tracks ( $\pi^+$  and  $\pi^-$ ) in various  $\eta$  regions corresponding to the full ID coverage (Fig. 6.24(a),  $|\eta| < 2.5$ ), the barrel region (Fig. 6.24(b),  $|\eta| < 1$ ), the end-cap A (Fig. 6.24(c),  $1 < \eta < 2.5$ ) and the end-cap C (Fig. 6.24(d),  $-2.5 < \eta < -1$ ). The curve from the *Pre-Collisions Alignment* indicates a curl-like distortion, in particular in the end-cap C region as spotted in Fig. 6.24(d). The result from the *Post-Collisions Alignment* has shown a dramatic improvement in the end-cap C region (filled circles in Fig. 6.24(d)) which is also seen in the track residual distributions, Figs. 6.18 - 6.21. For a rough estimate of the magnitude of the bias in the  $K_s^0$  mass with a curl misaligned geometry, we have overlaid the data distributions on top of the results from the Monte Carlo samples reconstructed with Curl-Large and Curl-Residual deformations, shown in Fig. 6.25. The current observed shift of the  $K_s^0$  mass in collision data is much smaller than we expect in the Curl-Residual misalignment, which implies that the current alignment does not contain a significant systematic effect as the Curl weak mode. All the weak mode effects will be checked with data in the future when more statistics are available.

The momentum resolution is not uniform in pseudorapidity at ATLAS due to the amount of material, thus the mass resolution of particles is expected to vary depending on the  $\eta$  position of the decay products. In addition, low  $p_T$  tracks tend to traverse the inner detector in the forward region, so the bias in the momentum scale for low- $p_T$  tracks is more visible in the forward region which is significant in  $K_s^0$  reconstruction as was studied in Ref. [79]. As the opening angle between the  $K_s^0$  decay products is small due to a boost by the  $p_T$  selection, the pseudorapidity of  $K_s^0$  is also a good measure of the pseudorapidity dependence. Figure. 6.26 shows the variation of the reconstructed  $K_s^0$  mass (left) and the mass resolution (right) as a function of the pseudorapidity of  $K_s^0$  and Fig. 6.27 is the variation of mass (left) and the mass resolution (right) as a function of the pseudorapidity from the most forward track. These two figures agree with each other, showing that the mass resolution is degraded in the end-cap regions that is dominated by the most forward track. In the detector central region, the mass resolution reconstructed from data is consistent with the expected, while in the end-cap regions discrepancies between data and

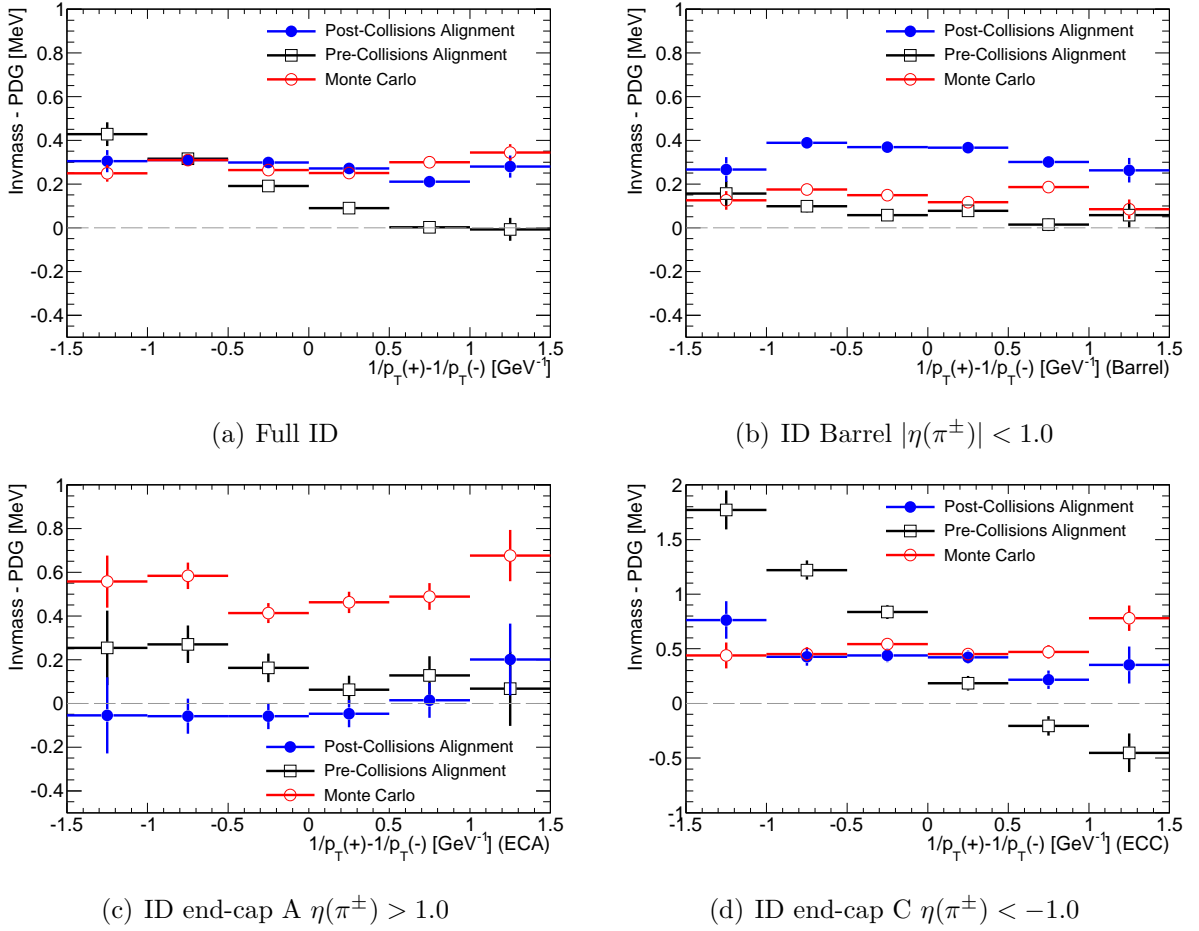


Figure 6.24: Invariant mass shift of  $K_s^0$  (w.r.t the PDG value) as a function of curvature difference between the daughter tracks in the whole ID coverage (6.24(a)), barrel (6.24(b)), end-cap A (6.24(c)) and end-cap C (6.24(d)). The improvement of May alignment is clearly seen in the end-cap C region (Fig. 6.24(d)).

the Monte Carlo sample are observed. Studies from Ref. [77] shows that the momentum scale is understood with a precision better than 0.1%. Meanwhile, variations of mass in the barrel and end-cap A region requires more efforts to improve the alignment in these regions.

Figure 6.28 shows the  $\phi$  dependence of the mass and the width of  $K_s^0$ . After the *Post-Collisions Alignment*, it becomes isotropic. Figure 6.29 shows the variation of the  $K_s^0$  mass and width with respect to the transverse momentum of  $K_s^0$ . The large mass shift in the low  $p_T$  region is caused by the imperfect low  $p_T$  tracking and material interactions. The large discrepancy between *Post-Collisions Alignment* and the Monte-Carlo is likely due to the low  $p_T$  reconstruction algorithm being skipped on purpose in the data processing from May. As the momentum increases, the absolute value of momentum uncertainty becomes large which is reflected by the increasing mass resolution in  $K_s^0$  as seen in Figure 6.29.

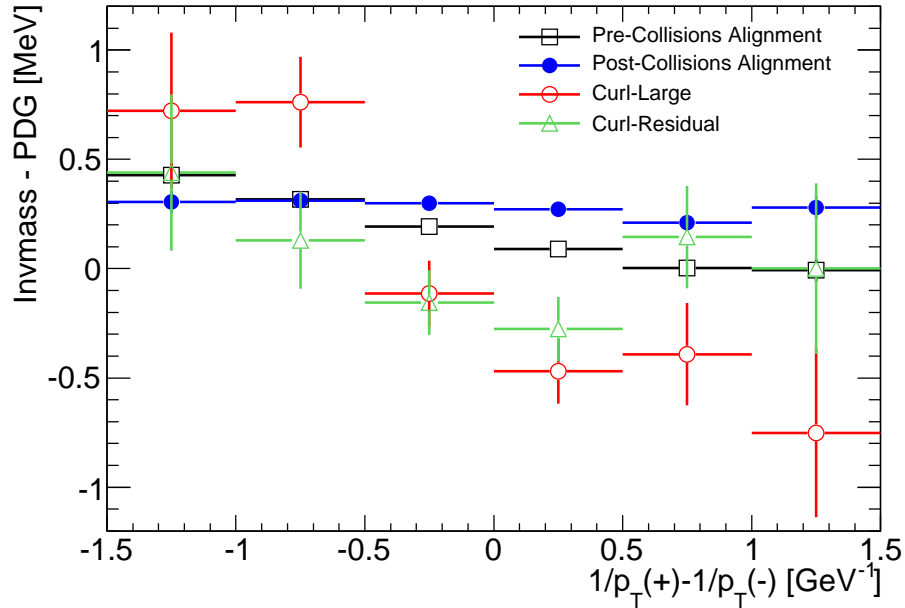


Figure 6.25: Invariant mass of  $K_s^0$  as a function of the curvature difference between the daughter tracks in the whole ID coverage from four alignment sets: Curl-Large, Curl-Residual, *Pre-Collisions Alignment* and *Post-Collisions Alignment*.

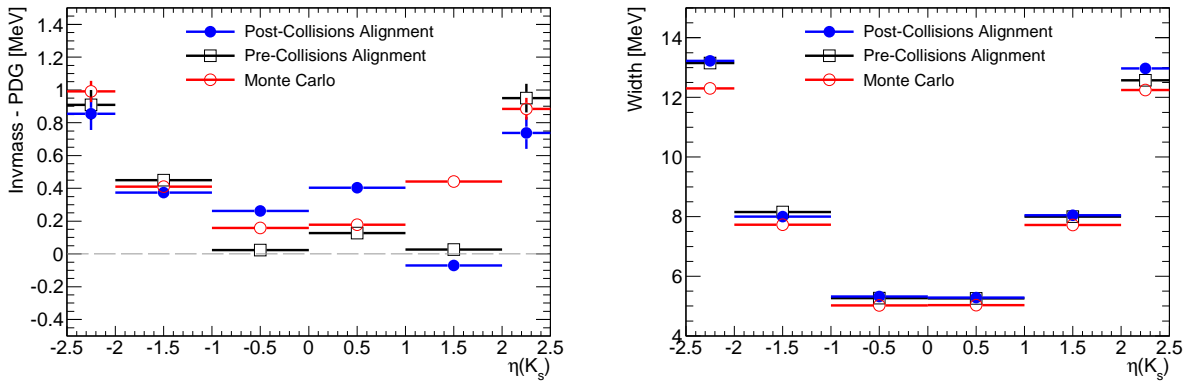


Figure 6.26: Invariant mass and width of  $K_s^0$  as a function of its  $\eta$  from the ATLAS minimum bias stream reconstructed with *Pre-Collisions alignment*, *Post-Collisions alignment* and compared with the non-diffractive minimum bias Monte Carlo sample.

### 6.3.3 Early $J/\psi$ performance of the inner detector

As the LHC is operating with proton-proton collisions with increasing luminosity, in addition to a large amount of  $K_s^0$  events, more and more  $J/\psi$  events are recorded by the ATLAS detector. The first result of studying the performance of low  $p_T$  tracking in ATLAS using  $J/\psi \rightarrow \mu^+\mu^-$  events from a dataset with an integrated luminosity of 78 nb is addressed

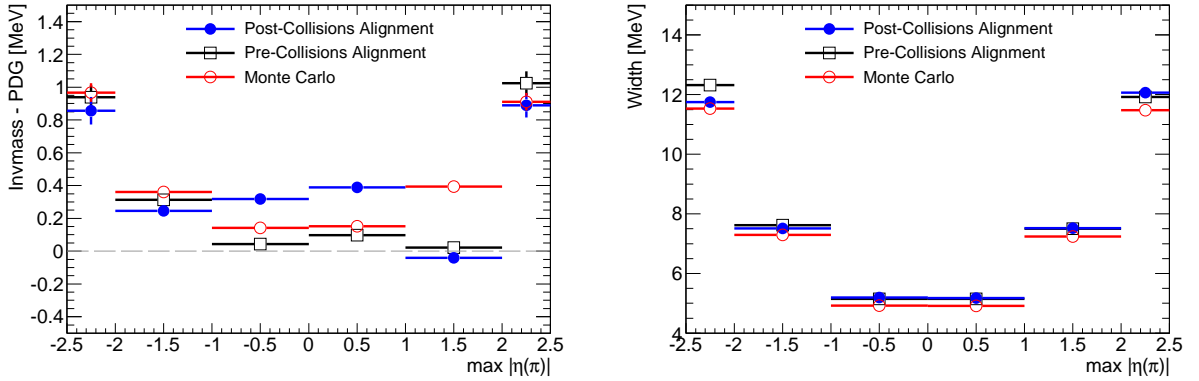


Figure 6.27: Invariant mass and width of  $K_s^0$  as a function of the  $\eta$  of the most forward track from the ATLAS minimum bias stream reconstructed with *Pre-Collisions alignment*, *Post-Collisions alignment* and compared with the non-diffractive minimum bias Monte Carlo sample.

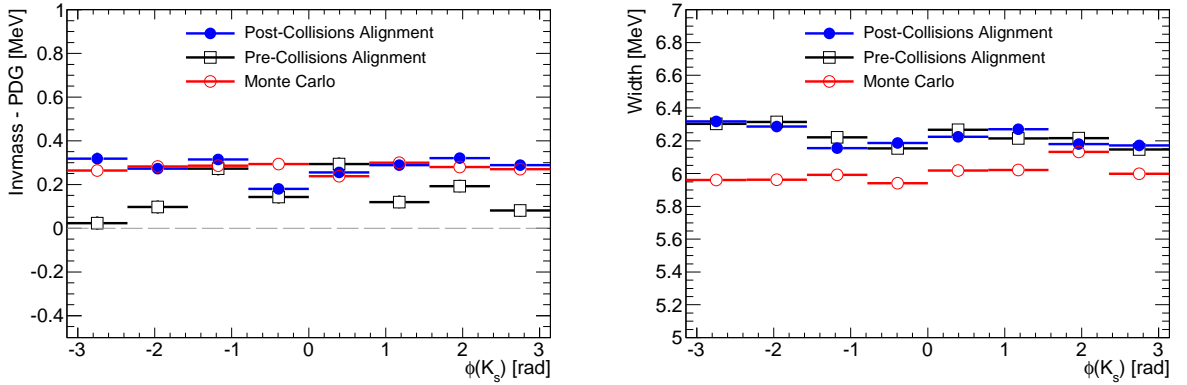


Figure 6.28: Invariant mass and width of  $K_s^0$  as a function of its  $\phi$  from the ATLAS minimum bias stream reconstructed with *Pre-Collisions alignment*, *Post-Collisions alignment* and compared with the non-diffractive minimum bias Monte Carlo sample.

in document No.4 listed on Pg. ii. Events are accepted in the analysis if they fulfil the following criteria:

- Events pass either a L1 minimum bias trigger with an identified muon at EF level, or a muon-based L1 trigger.
- Each event is required to contain at least one primary vertex reconstructed from at least three tracks.
- Muons are accepted if they are associated with ID tracks and contain at least one hit in the pixel detector and at least six hits in the SCT detector. Consequently the tracks should pass the baseline momentum cuts for the muon identification in



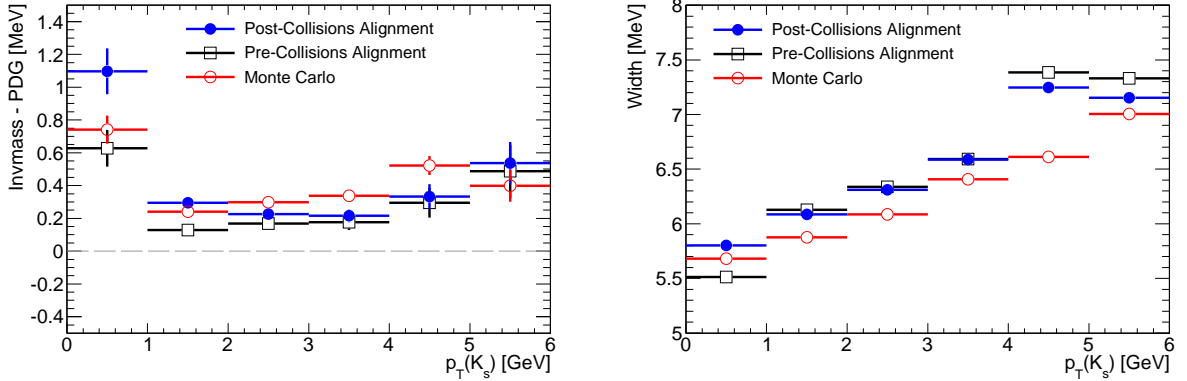
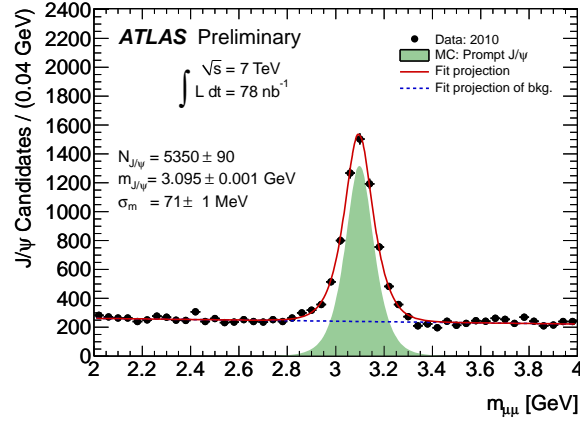


Figure 6.29: Invariant mass and width of  $K_s^0$  as a function of its  $p_T$  from the ATLAS minimum bias stream reconstructed with *Pre-Collisions alignment*, *Post-Collisions alignment* and compared with the non-diffractive minimum bias Monte Carlo sample.

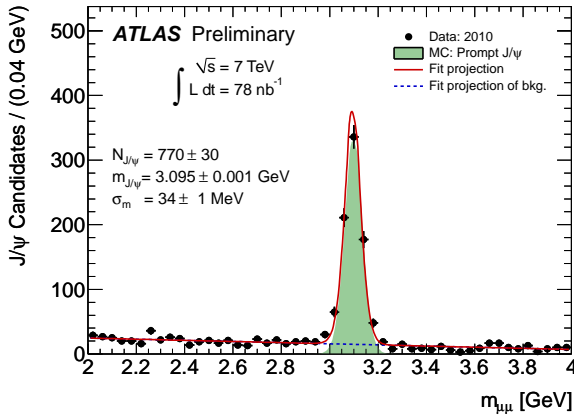
the Muon Spectrometer ( $p > 3$  GeV) and the ID tracking reconstruction ( $p_T > 0.1$  GeV).

- The ID tracks of each oppositely charged  $\mu^+\mu^-$  pair are fitted to a common vertex using the ATLAS offline vertexing tools and only a very loose cut on the  $\chi^2$  of the vertex fit is applied ( $\chi^2 < 200$ ).

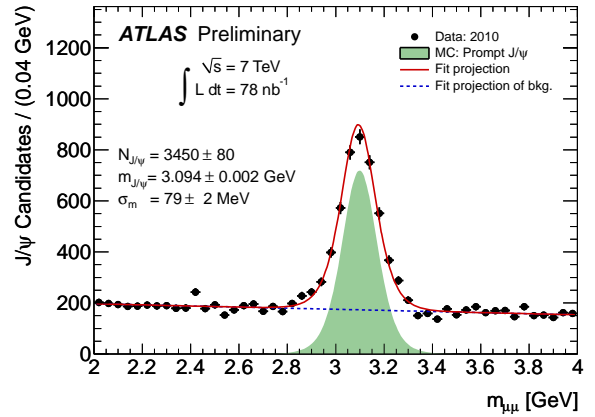
The invariant masses of the  $J/\psi$  candidates are calculated using the ID track parameters of the selected muons. An unbinned maximum likelihood fit is used to extract the mass and the resolution of  $J/\psi$  from data where the signal distribution was modelled with a Gaussian distribution taking into account the per-candidate mass error obtained from the vertex fit, and the background is parameterised by a first order polynomial. The prompt  $J/\psi$  Monte Carlo sample for comparisons was produced based on the NRQCD Colour Octet Mechanism, generated with Pythia [57], tuned with the ATLAS MC09 turn [80] and MRST LO\* [81], and fully reconstructed with the same software as was used in the data processing. The invariant mass distribution of all the selected muon pairs is shown in Fig. 6.30(a) where the Monte Carlo distribution is normalised to the number of signal events extract from the fit to the data. The  $J/\psi$  mass returned by the fit is  $3.095 \pm 0.001$  GeV, which is consistent with the PDG value of  $3.096916 \pm 0.000011$  GeV [2]. The number of observed  $J/\psi \rightarrow \mu^+\mu^-$  candidates is  $5351 \pm 93$  in the mass range 2-4 GeV and the mass resolution is  $71 \pm 1$  MeV. As addressed previously in the  $K_s^0$  events, the invariant mass resolution depends on the pseudorapidity of the daughter tracks due to the momentum resolution. To illustrate this effect on  $J/\psi$  decays, the accepted  $J/\psi$  candidates with both muons in the barrel ( $|\eta(\mu^\pm)| < 1.05$ ), or in the end-cap region ( $1.05 < |\eta(\mu^\pm)| < 2.5$ ), were separated from the data, and their invariant mass distributions are shown in Fig. 6.30(b) and Fig. 6.30(c) respectively. The fit results show that the  $J/\psi$  mass resolution with both muons in the end-cap region is about 2.5 times as large as the one with both muons in the barrel. The degradation in the forward region is caused by the imperfect description of the material and the low  $p_T$  tracking in that region. More detailed studies of the ID



(a) The invariant mass distribution of reconstructed  $J/\psi \rightarrow \mu^+\mu^-$  candidates (points), along with the prompt  $J/\psi$  Monte Carlo prediction (filled area) normalised to the number of signal events extracted from the fit to data.



(b) Invariant mass distribution of  $J/\psi \rightarrow \mu^+\mu^-$  candidates with both muons in the ID barrel region ( $|\eta(\mu^\pm)| < 1.05$ ).



(c) Invariant mass distribution of  $J/\psi \rightarrow \mu^+\mu^-$  candidates with both muons in the ID end-cap region ( $1.05 < |\eta(\mu^\pm)| < 2.5$ ).

Figure 6.30: Invariant mass distributions of  $J/\psi \rightarrow \mu^+\mu^-$  candidates in data in the whole ID coverage (6.30(a)), barrel (6.30(b)), end-cap (6.30(c)) regions.

performance will be feasible when sufficient statistics of  $J/\psi$  samples are achieved. The results are expected to provide us with a better understanding of the ID tracking system, which will also be needed to support the measurements of B hadron properties in the near future.



# Chapter 7

## Summary and outlook

The Standard Model has provided a successful description on the interactions of the fundamental particles, particularly the Higgs mechanism proposed to answer the electroweak symmetry breaking and the origin of particle masses. Moreover, many other models have been derived to extend the Standard Model. All these theoretical predictions suggest a large physics potential to the ongoing and future experiments at energy frontiers in particle physics. At present, the LHC is running with proton-proton collisions at an unprecedented centre-of-mass energy, 7 TeV, with increasing luminosities, and is expected to reach 14 TeV in the future. The high energy and luminosity of the LHC enable great opportunities for a large range of physics measurements, such as precision measurements of the properties of the known particles, and possible discoveries of the Higgs boson and physics beyond the Standard Model. The ATLAS detector is one of the general-purpose detectors at the LHC which has been optimised to fully exploit the LHC physics potential.

The rate of B-hadron production at the LHC is expected to be tremendous, thanks to the large hadronic  $b$ -quark production and the high luminosity. Precision measurements of the B hadron properties and the CP violation are expected to test the Standard Model predictions, constrain the elements of the CKM matrix, and reveal new physics beyond the Standard Model. Although the main focus of the ATLAS physics program is the direct searches for new particles, indirect constraints from B decays will provide complementary information on the unknown parameters of new physics models that couple to  $b$  quarks. In the B hadron family, the  $B_c$  meson is a unique species because of its  $b\bar{c}$  flavour with two different heavy quarks,  $b$  and  $c$ . Theoretically, the  $b\bar{c}$  system can be considered as quarkonium, like the  $c\bar{c}$  and  $b\bar{b}$  systems, thereby can be described in the framework of the non-relativistic potential models. In addition, other theoretical models, such as perturbative QCD and lattice QCD, have attempted to predict the properties of the  $B_c$  meson. Measurements of the  $B_c$  meson will serve as complementary tests of the models for quarkonium, and ultimately the mass difference between the ground state and excited states will allow to extract the shape of the strong potential. Until now, the mass of the  $B_c$  ground state has been measured subsequently in the Tevatron experiments through semileptonic and hadronic decays, whilst the lifetime measurement is only completed through the semileptonic mode. In this thesis, one of the main topics is about the

ATLAS sensitivity of observing the  $B_c \rightarrow J/\psi \pi$  decay at 10 TeV with integrated luminosity of  $1 \text{ fb}^{-1}$  which is also applicable for the current 7 TeV scenario. We choose this channel for the first  $B_c$  search in ATLAS in order to minimise the dependence upon the calorimeter absolute calibration during the early data taking era. Shown in Fig. 7.1, as of July 19th 2010, the LHC has delivered more than  $300 \text{ nb}^{-1}$  of proton-proton collisions to ATLAS. It is planned that the total integrated luminosity will reach  $1 \text{ fb}^{-1}$  at the end of 2011. With this integrated luminosity, we will be able to observe this channel and perform the first measurement of the  $B_c$  mass. Our next target is the reconstruction of  $B_c$  excited states through their radiative transitions to the ground state with emissions of photons and pions. The theoretical calculation of the mass difference between  $B_c(2S)$  and  $B_c(1S)$  is around 600 MeV which is above our detector resolution, therefore we expect to observe the 2S state in the ATLAS experiment. Meanwhile, we will also pursue the  $B_c$  lifetime measurement from both hadronic and semileptonic decays. We are especially keen to achieve this measurement from the challenging  $B_c \rightarrow J/\psi \pi$  decay due to its low branching ratio, which is expected to be compensated for by the high B-hadron production rate and the high luminosity of the LHC.

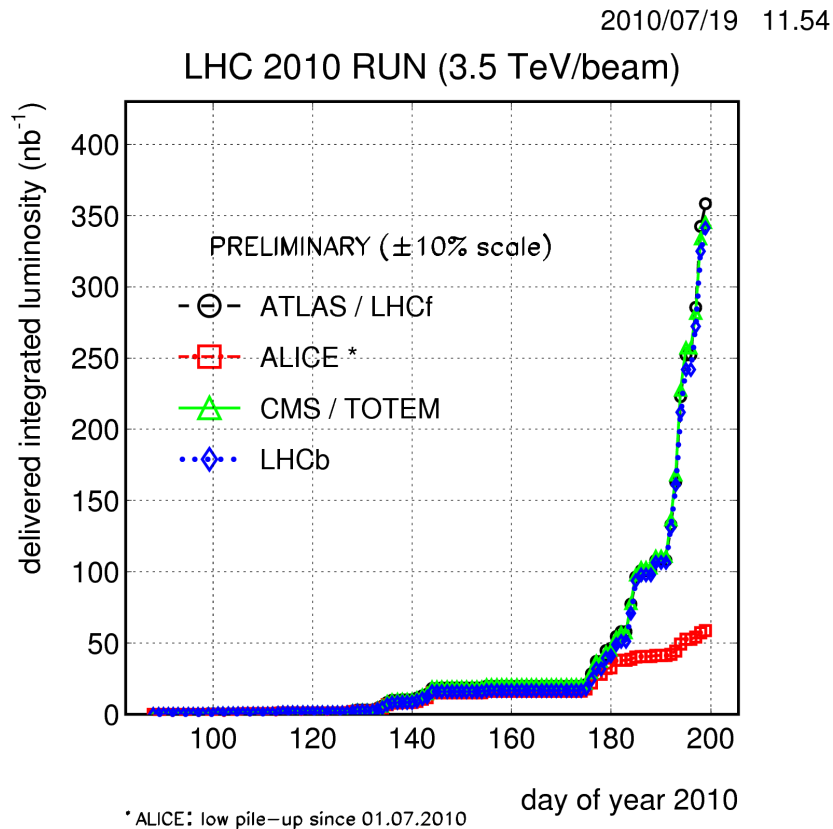


Figure 7.1: The LHC delivered integrated luminosity by the 200th day of 2010 (from S. Myers' talk in ICHEP 2010).

During the initial period of data taking, the performance of the ATLAS detector needs

---

to be studied carefully and understood. As most of the B physics analyses in ATLAS prefer di-muon final states owing to the efficient muon triggers, measurements in the inner detector are essential for low momentum tracks. To achieve the expected accuracy of the ID tracking, the alignment applies track-based algorithms aiming at precisely describing the positions of ID sensor modules in the offline event reconstruction. The alignment procedure determines alignment constants by minimising the track-hit residuals on different levels of granularity. Meanwhile, special cares of systematic misalignments of large scale structures in the ID should be taken, which we refer to as “weak modes” because the tracking residuals are unchanged. The weak mode deformations are hard to detect in the standard alignment procedure, and are therefore the potential alignment systematics for physics measurements. Before the start up of the LHC we investigated the impact of the possible ID misalignments on physics using Monte Carlo samples of well known resonances,  $K_s^0$ ,  $J/\psi$ ,  $\Upsilon$ , and  $Z^0$  decays, with particular emphasis on their sensitivities to the expected systematic misalignments. Our experience from these studies has also been implemented in the ATLAS offline Data Quality Framework which is now being used to assess the quality of the ID alignment and tracking during the data taking. The first set of alignment constants applied in the collisions was determined during the detector commissioning period with cosmic ray data. Later on new alignment constants were produced by using 2009 cosmic ray data and the 900 GeV collision data simultaneously. The performance of the ID alignment has been demonstrated with generic tracks in 7 TeV collisions recorded by the ATLAS minimum bias trigger, showing a large improvement in the new alignment, particularly in the end-cap regions. In addition, I have also demonstrated the tracking performance on the  $K_s^0$  mass reconstruction from  $K_s^0 \rightarrow \pi^+\pi^-$  decays using the same data. The alignment improvement is also seen in  $K_s^0$  decays, and no weak mode deformation is found in the new alignment. Furthermore, the tracking performance on early  $J/\psi$  candidates is also shown in this thesis. As the statistics increase, the alignment is being improved by the standard algorithms in terms of track-hit residuals, however, our understandings of systematic misalignments are still limited. The studies of alignment performance on resonances are ongoing. Results from the  $K_s^0$  events have already shown the sensitivity to the alignment changes although it is not easy to separate the alignment effect from the material effect for such low  $p_T$  tracks at this stage. Soon, the investigation will be extended to larger  $p_T$  regions, taking advantages of the increasing statistics of the  $J/\psi$ ,  $\Upsilon$  and  $Z^0$  resonances. The focus will be to detect and eliminate the systematic misalignments that we have considered, and the unexpected complex misalignments, and eventually, to provide high quality estimates of the tracking systematics associated with the alignment.



# Acknowledgement

The past four years mean a lot to me. I owe my gratitude to many people that have always been generous to help me.

First of all, I am heartily thankful to my supervisor, Else Lytken, for her continuous support and guidance, in particular her encouragement and help whenever I encountered problems with my work. This thesis would not have been possible without her.

Thanks also must go to my previous supervisor, Paula Eerola, for her supervision during the early time of my Ph.D and for leading me to the fascinating world of beauty physics.

I am indebted to my deputy supervisors, Torsten Åkesson for his support all the way along, and Torbjörn Sjöstrand for his readings and comments on this thesis as well as all the discussions about QCD and Monte Carlo generators. Thanks also to Evert Stenlund who spent the precious summer time correcting my thesis.

I owe a big thank to Maria Smizanska, for her invaluable advice and support, from whom I have learned so much about B physics analysis. I would also like to thank my collaborators, Sally Seidel and Konstantin Toms, for their large contributions to the  $B_c$  analysis work. And I really appreciate the comments and suggestions we received during the note approval, which enabled us to vastly improve our analysis. Thanks to the people who reviewed our analysis note.

My sincere gratitude also goes to Tobias Golling, for guiding me through the ID performance study and the monitoring task. He has provided me with lots of insights into tracking and physics. It is pleasant experience to work with him and the other alignment monitors during the past two and a half years. I really enjoy all the discussions and effort that we made for solving various physics and software problems, as well as those countless exciting Savannah reports. Thank all of you for teaching me so much about analysis and programming. Besides, I want to thank Pawel Brückman de Renstrom, for sharing his expertise and encouraging my analytical thinking during the study of weak modes.

Furthermore, I would like to thank the support from the ATLAS B physics group, the inner detector alignment group, the tracking experts, the data quality experts, and all the others who have been so patient to my endless questions and requests. The work would not have been possible without the entire ATLAS Collaboration, so I thank everyone that has devoted time to detector and service work.

Moreover, I would like to thank all my colleagues at Lund, for making me feel like home here. Many friends have brought me a lot of joys since I moved to Europe. For those who are based at CERN, thank you for making each of my short-stays enjoyable. For the Lund gang, listing all your names would be really hard, so please allow me to summarise with a



big “Thank you!”. You are all on the list, and I hope you will enjoy my defence day :)

Finally, my deepest thanks to my parents, for their continuing support from thousands of kilometres away, to whom this thesis is dedicated.

# Bibliography

- [1] G. L. Kane, *Modern Elementary Particle Physics*, Addison Wesley, Advanced Book Program, Redwood City, Calif.
- [2] C. Amsler *et al.*, *Phys. Lett. B* **667** 1-5 (2008) and <http://pdg.lbl.gov>.
- [3] S. L. Glashow, *Nucl. Phys.* **22**, 579 (1961);  
A. Salam and J. C. Ward, *Phys. Lett.* **13** (1964) 168;  
S. Weinberg, *Phys. Rev. Lett.* **19**, 1264 (1967).
- [4] R. K. Ellis, W. J. Stirling, B. R. Webber, *QCD and Collider Physics*, Cambridge University Press, 1996.
- [5] The ATLAS collaboration, *ATLAS Detector and Physics Performance Technical Design Report* (CERN/LHCC/2003-022) *Phys. Rev. D* **34**, 1547 (1986).
- [6] P. Nason, S. Dawson and R. K. Ellis, *Nucl. Phys. B* **327** (1990) 49; *ibid.* **B335** (1990) 260(erratum)
- [7] S. Frixione *et al.*, *Nucl. Phys. B* **431** (1994) 453.
- [8] CDF collaboration, F. Abe *et al.*, *Phys. Rev. Lett.* **68** (1992) 3403; *ibid.* **71** (1993) 500; *ibid.* **71** (1993) 2396; *ibid.* **71** (1993) 2537; *Phys. Rev. D* **45** (1994) 4252.
- [9] D0 collaboration, S. Abachi *et al.*, *Phys. Rev. Lett.* **74** (1995) 3548.
- [10] J. J. Aubert *et al.*, *Phys. Rev. Lett.* **33** (1974) 1404;  
J. E. Augustin *et al.*, *Phys. Rev. Lett.* **33** (1974) 1406;
- [11] F. Abe *et al.*, *Phys. Rev. Lett.* **81**, 2432 (1998).
- [12] B. Aubert *et al.* BABAR Collaboration *Phys. Rev. Lett.* **101**, 071801 (2008); Erratum-  
*ibid.* **102**:029901, 2009
- [13] E. Eichten, K. Gottfried, T. Kinoshita, K. Lane, T.-M. Yan *Phys. Rev. D* **21** 203 (1980).
- [14] C. Quigg, J. L. Rosner, *Phys. Lett. B* **71**, 153 (1977).
- [15] A. Martin, *Phys. Lett. B* **93**, 338 (1980).

- [16] J. L. Richardson *Phys. Lett. B* **82** 272 (1979).
- [17] W. Buchmüller and S-H. H. Tye, *Phys. Rev. D* **24** (1981) 132.
- [18] B. Z. Kopeliovich and J. Raufeisen, *Lect. Notes Phys.* **647** (2004) 305 [arXiv:hep-ph/0305094].
- [19] M. B. Voloshin, *Charmonium* [arXiv:hep-ph/0711.4556].
- [20] P. Hasenfratz, P. (1987) *Nonperturbative methods in quantum field theory* in *Proceedings of the XXIII International Conference on High Energy Physics*, ed. S.C. Loken (World Scientific, Singapore)
- [21] Fukugita, M. (1987). *Present status of numerical quantum chromodynamics in Lattice Gauge Theory using parallel processors*, ed. Li, X., Qiu, Z. and Ren, H. (Gordon and Breach, New York).
- [22] J. F. Donoghue, E. Golowich, B. R. Holstein, *Dynamics of the Standard Model*, Cambridge University Press, 1992.
- [23] See e.g. V. G. Kartvelishvili, A. K. Likhoded, S. R. Slabospitsky, *Sov. J. Nucl. Phys.* **28** (1978) 280;  
M. Gluck, J. F. Owens and E. Reya, *Phys. Rev. D* **17** (1978) 2324;  
E. L. Berger and D. L. Jones, *Phys. Rev. D* **23** (1981) 1521;  
V. G. Kartvelishvili, A. K. Likhoded, *Sov. J. Nucl. Phys.* **39** (1984) 298;  
B. Humpert, *Phys. Lett. B* **184** (1987) 105.
- [24] G. Schuler, preprint CERN-TH-7170-94 (1994).  
R. Gavai *et al.* *Intl. J. Mod. Phys A* **10** (1995) 3043.
- [25] M. Kramer, *Prog. Part. Nucl. Phys.* **47** (2001) 141 [arXiv:hep-ph/0106120].
- [26] E. Braaten, T. C. Yuan, *Phys. Rev. Lett.* **71** (1993) 1673 [arXiv:hep-ph/9303205].
- [27] G. T. Bodwin, E. Braaten, G. P. Lepage, *Phys. Rev. D* **51** (1995) 1125 [arXiv:hep-ph/9407339], erratum-*ibid.* **D55** (1997) 5853.
- [28] N. Brambilla *et al.* [Quarkonium Working Group], *Heavy quarkonium physics*, [arXiv:hep-ph/0412158].
- [29] S.S. Gershtein *et al.*, *Uspekhi Fiz. Nauk* **165**, 3 (1995).
- [30] Hikasa K, *et al.*, *Phys. Rev. D* **45**(II) S1 (1992).
- [31] Novikov V A *et al.* *Phys. Rep. C* **41** 1 (1978);  
Eichten E, Godfried K *Phys. Lett. B* **66** 286 (1977)
- [32] Gottfried K *Phys. Rev. Lett.* **40** 598 (1978);  
Voloshin M B *Nucl. Phys. B* **154** 365 (1979);  
Peskin M *Nucl. Phys. B* **156** 365 (1979).

- [33] Bagan E *et al.*, Preprint CERN-TH.7141/94 (1994).
- [34] Colangelo P, Nardulli G, Paver, N *Z. Phys. C* **57** 43 (1993).
- [35] Jenkins E *et al.* *Nucl. Phys. B* **390** 463 (1993).
- [36] Shifman M A, Vainshtein A I, Zakharov V I *Nucl. Phys. B* **147** 345, 448 (1979);  
Reinders L J, Rubinshtein H, Yazaki S *Phys. Rep.* **127** 1 (1983);  
Narison S *Phys. Lett. B* **198** 104 (1987);  
Dominguez C A, Paver N *Phys. Lett. B* **197** 423 (1987), **199** 596 (1987).
- [37] V. V. Kiselev, [arXiv:hep-ph/0308214] (2003).
- [38] I. Bigi, *Phys. Lett. B* **371**, 105 (1996);  
M. Beneke, G. Buchalla, *Phys. Rev. D* **53**, 4991 (1996);  
A.I. Onishchenko, [arXiv:hep-ph/9912424];  
Ch.-H. Chang, Sh.-L. Chen, T.-F. Feng, X.-Q. Li, *Commun. Theor. Phys.* **35**, 51 (2001), *Phys. Rev. D* **64**, 014003 (2001).
- [39] V.V.Kiselev, A.K.Likhoded, A.E.Kovalsky, *Nucl. Phys.* **B585**, 353 (2000), [arxiv:hep-ph/0006104 (2000)].
- [40] I. P. Gouz, V. V. Kiselev, A. K. Likhoded, V. I. Romanovsky, O. P. Yushchenko, [arXiv:hep-ph/0211432].
- [41] E. Braaten, K. Cheung and T.C. Yuan, *Phys. Rev. D* **48**, 5049 (1993);  
K. Cheung, *Phys. Rev. Letter B* **71**, 3413 (1993).
- [42] A.V. Berezhnoy, A.K. Likhoded, M.V. Shevlyagin, *Yad. Fiz.* **58**, 730 (1995);  
A.V. Berezhnoy, A.K. Likhoded, O.P. Yuschenko, *Yad. Fiz.* **59**, 742 (1996);  
C.-H.Chang *et al.*, *Phys. Lett. B* **364**, 78 (1995);  
K. Kolodziej, A.Leike, R.Rückl, *Phys. Lett. B* **355**, 337 (1995);  
A.V.Berezhnoy, V.V.Kiselev, A.K.Likhoded, *Z. Phys. A* **356**, 79 (1996).
- [43] C-H Chang, X-G Wu, *Eur. Phys. J.* **C38** (2004) 267-276, [arxiv:hep-ph/0309121].
- [44] *The LHC Design Report*, CERN-2004-003.
- [45] The ATLAS Collaboration, *The ATLAS Experiment at the CERN Large Hadron Collider*, 2008 *JINST* **3** S08003.
- [46] The ATLAS collaboration, *Detector and Physics Performance Technical Design Report*, LHCC 99-14/15.
- [47] The ATLAS Collaboration, *Expected Performance of the ATLAS Experiment*, CERN-OPEN-2008-020.
- [48] V. Kartvelishvili, *Nucl. Phys. B (Proc. Suppl.)* **172** (2007) 208211.

- 
- [49] R. Frühwirth, *Comp. Phys. Comm.* **100** (1997) 1.
- [50] R. Frühwirth, A. Strandlie, *Comp. Phys. Comm.* **120** (1999) 197214..
- [51] S. Hassini, *et al.*, *NIM A* **572** (2007) 77-79.
- [52] TH. Lagouri, *et al.*, *IEEE Trans. Nucl. Sci.* **51** (2004) 3030-3033.
- [53] F. Abe *et al.*, *Phys. Rev. D* **58**, 112004 (1998).
- [54] The CDF Collaboration, *Phys. Rev. Lett.* **96**, 082002 (2006).
- [55] The CDF Collaboration, *Phys. Rev. Lett.* **100**,182002 (2008).
- [56] The D0 Collaboration, *Phys. Rev. Lett.* **101**, 012001 (2008).
- [57] T. Sjöstrand, S. Mrenna and P. Skands, *JHEP* **05** (2006) 026, LU TP 06-13, FERMILAB-PUB-06-052-CD, [arxiv:hep-ph/0603175].
- [58] A.V. Berezhnoy, V.V. Kiselev, A.K. Likhoded, [arXiv:hep-ph/9507242], [arXiv:hep-ph/9602347], [arXiv:hep-ph/9604421] A.V. Berezhnoy, [arXiv:hep-ph/0407315]
- [59] J. Pumplin *et al.*, [arXiv:hep-ph/0201195].
- [60] D. Lange, *Nucl. Inst. and Meth. A* **462** (2001) 152.
- [61] The ATLAS Collaboration, *Impact of Inner Detector Misalignments on Selected Physics*, ATL-PHYS-PUB-2009-080.
- [62] The ATLAS Collaboration, *Alignment requirements, in ATLAS Inner Detector Technical Design Report, vol I*, p. 215. CERN-LHCC-1997-016, CERN, Geneva, 1997.
- [63] S. Gibson *et al.*, *Coordinate measurement in 2-D and 3-D geometries using frequency scanning interferometry*, *Opt. Laser Eng.* **44** (2007) 79-95.
- [64] K. Störig, T. Göttfert, J. Grosse-Knetter, K. Kröninger, A. quadt, *Alignment Studies of the ATLAS Silicon Trackers with Overlap Residuals*, ATL-INDET-INT-2009-001.
- [65] P. Brückman, A. Hicheur and S. J. Haywood, *Global  $\chi^2$  approach to the Alignment of the ATLAS silicon Tracking Detector*, ATL-INDET-PUB-2005-002.
- [66] R. Härtel, *Iterative local  $\chi^2$  alignment approach for the ATLAS SCT detector*, Master's thesis, MPI, Munich, 2005.
- [67] T. Göttfert, *Iterative local  $\chi^2$  alignment algorithm for the ATLAS Pixel detector*, Master's thesis, Universität Würzburg and MPI Munich, 2006.
- [68] F. Heinemann, *Track based Alignment of the ATLAS Silicon Detectors with the Robust Alignment Algorithm*, ATLAS Note ATL-INDET-PUB-2007-011.

- 
- [69] The ATLAS Collaboration, *Alignment Performance of the ATLAS Inner Detector Tracking System in 7 TeV proton-proton collisions at the LHC*, ATLAS-CONF-2010-067.
- [70] D. N. Brown, A. V. Gritsan, Z. J. Guo and D. Roberts, *Local Alignment of the BABAR Silicon Vertex Tracking Detector*, [arXiv:0809.3823].
- [71] J. Alison, B. Cooper, T. Göttfert, *Production of Systematically Misaligned Geometries for the ATLAS Inner Detector*, ATL-INDET-INT-2009-003.
- [72] Corso-Radu, A; Kolos, S; Hadavand, H; Kehoe, R; Hauschild, M, *Data Quality Monitoring Framework for the ATLAS Experiment at the LHC*, ATL-DAQ-CONF-2008-006.
- [73] Full Dress Rehearsal, ATLAS twiki page:  
<https://twiki.cern.ch/twiki/bin/view/Atlas/FinalDressRehearsal?topic=FullDressRehearsal>
- [74] J. Alison, *et al.*, *Alignment of the Inner Detector using misaligned CSC data*, ATL-COM-INDET-2008-014, (2008).
- [75] J. Alison, *et al.*, *Inner Detector Alignment within the ATLAS Full Dress Rehearsal*, ATL-COM-INDET-2009-033.
- [76] The ATLAS Collaboration, *The ATLAS Inner Detector commissioning and calibration*, [arXiv:1004.5293] (Submitted to Eur. Phys. J. C).
- [77] The ATLAS Collaboration, *Study of the Material Budget in the ATLAS Inner Detector with  $K_s^0$  decays in collision data at  $\sqrt{s} = 900$  GeV*, ATLAS-CONF-2010-019.
- [78] The ATLAS Collaboration, *Kinematic Distributions of  $K_s^0$  and  $\Lambda^0$  decays in collision data at  $\sqrt{s} = 7$  TeV*, ATLAS-CONF-2010-067.
- [79] The ATLAS Collaboration, *Estimating Track Momentum Resolution in Minimum Bias Events using Simulation and  $K_s^0$  in  $\sqrt{s} = 900$  GeV Collision data*, ATLAS-CONF-2010-009.
- [80] The ATLAS Collaboration, *ATLAS Monte Carlo tunes for MC09*, ATL-PHYS-PUB-2010-002.
- [81] A. Sherstnev and R. S. Thorne, *Parton Distributions for LO Generators*, [arXiv:hep-ph/0711.2473].



# List of abbreviations

<b>ALICE</b>	LHC experiment: A Large Ion Collider Experiment
<b>ATLAS</b>	LHC experiment: A Toroidal LHC ApparatuS
<b>BC</b>	beam constraint
<b>BR</b>	barrel region
<b>CKM</b>	Cabibbo-Kobayashi-Maskawa matrix
<b>CMS</b>	LHC experiment: Compact Muon Solenoid
<b>COM</b>	Colour Octet Model
<b>CSC</b>	Cathode Stripe Chambers, or Computing System Commissioning
<b>CSM</b>	Colour Singlet Model
<b>CTP</b>	central trigger processor
<b>DAQ</b>	data acquisition system
<b>DNA</b>	dynamic noise adjustment, a track fitter
<b>DoF</b>	degrees-of-freedom
<b>DQMF</b>	Data Quality Monitoring Framework
<b>EC</b>	end-cap regions (end-cap A, end-cap C)
<b>EF</b>	event filter
<b>EM</b>	electromagnetic
<b>FCal</b>	Forward Calorimeter
<b>FDR</b>	Full Dress Rehearsal
<b>FSI</b>	Frequency Scan Interferometry
<b>FWHM</b>	full width at half maximum
<b>GSF</b>	Gaussian-sum filters, a track fitter
<b>HEC</b>	Hadronic End-cap Calorimeter
<b>ID</b>	the ATLAS inner detector containing the Pixel detector, SCT detector and the TRT.



<b>L1, L2</b>	Level 1, Level 2
<b>LAr</b>	the liquid-argon electromagnetic sampling calorimeters
<b>LEP</b>	The Large Electron Positron (LEP) collider at CERN operated from 1989 to 2000.
<b>LHC</b>	The Large Hadron Collider
<b>LHCb</b>	LHC experiment: Large Hadron Collider beauty
<b>LHCf</b>	LHC experiment: Large Hadron Collider forward
<b>LUT</b>	lookup tables
<b>MDT</b>	Monitored Drift Tubes
<b>MS</b>	muon spectrometer
<b>NRQCD</b>	non-relativistic QCD
<b>PS</b>	Proton Synchrotron
<b>PSB</b>	Proton Synchrotron Booster
<b>PV, SV</b>	primary vertex, secondary vertex
<b>QCD</b>	Quantum Chromodynamics
<b>QED</b>	Quantum Electrodynamics
<b>RoI</b>	Region-of-Interest
<b>RPC</b>	Resistive Plate Chambers
<b>SCT</b>	the semiconductor tracker
<b>SFO</b>	sub-farm output, an output node of the DAQ system to store events that are selected by the trigger in the local file system according to the classification done by the event filter.
<b>SPS</b>	Super Proton Synchrotron
<b>SUSY</b>	Supersymmetry
<b>Tevatron</b>	a proton-antiproton accelerator and collider at FermiLab with two experiments, D0 and CDF.
<b>TGC</b>	Thin Gap Chambers
<b>TOTEM</b>	LHC experiment: TOTAl Elastic and diffractive cross section Measurement
<b>TRT</b>	transition radiation tracker